Multi-instrument observations of various ionospheric disturbances caused by the 6 February 2023 Turkey earthquake

Haris Haralambous[1], Marco Guerra[2], Jaroslav Chum[3], Tobias G.W. Verhulst[4], Veronika Barta[5], David Altadill[6], Claudio Cesaroni[7], Ivan Galkin[8], Kiszely Márta[9], Jens Mielich[10], Daniel Kouba[11], D. Buresova[12], A. Segarra[13], Luca Spogli[7], Jan Rusz[14], and Jan Zedník[15]

[1]Frederick University
[2]1) Istituto Nazionale di Geofisica e Vulcanologia, Rome, Italy , 2) Sapienza Università di Roma
[3]Institute of Atmospheric Physics CAS
[4]Royal Meteorological Institute (RMI)
[5]Research Centre for Astronomy and Earth Sciences, Geodetic and Geophysical Institute
[6]Observatori de l'Ebre
[7]Istituto Nazionale di Geofisica e Vulcanologia
[8]UMass Lowell, Space Science Lab
[9]Kövesligethy Radó Seismological Observatory, Institute of Earth Physics and Space Science
[10]Leibniz-Institute of Atmospheric Physics (LG)
[11]Institute of Atmospheric Physics Academy of Sciences of the Czech Republic
[12]Institute of Atmospheric Physics, Prague, Czech Republic
[13]Observatori de l'Ebre-CSIC
[14]Institute of Atmospheric Physics of the CAS
[15]Institute of Geophysics Czech Academy of Sciences

May 25, 2023

Abstract

In this work, we investigate various types of ionospheric disturbances observed over Europe after the earthquake in Turkey on 6 February 2023.By combining observations from Doppler sounding systems, ionosondes, and GNSS receivers, we are able to discern different types of disturbances, propagating with different velocities and through different mechanisms. We can detect the co-seismic disturbances produced in the ionosphere close to the epicenter, as well the ionospheric signatures of acoustic waves propagating as a consequence of propagating seismic waves.

Multi-instrument observations of various ionospheric disturbances caused by the 6 February 2023 Turkey earthquake

Haris Haralambous[1], Marco Guerra[2,3], Jaroslav Chum[4], Tobias G. W. Verhulst[5], Veronika Barta[6], David Altadill[7], Claudio Cesaroni[2], Ivan Galkin [8], Kiszely Márta[9], Jens Mielich[10], Daniel Kouba[4], Dalia Buresova[4], Antoni Segarra[7], Luca Spogli[2,11], Jan Rusz [4], Jan Zedník[12]

[1] Frederick University, School of Engineering, Nicosia, Cyprus
[2] Istituto Nazionale di Geofisica e Vulcanologia, Rome, Italy
[3] Sapienza Università di Roma, Rome, Italy
[4] Institute of Atmospheric Physics, Czech Academy of Sciences, Prague, Czech Republic
[5] Royal Meteorological institute of Belgium & Solar Terrestrial Centre of Excellence, Brussels, Belgium
[6] Institute of Earth Physics and Space Science, Sopron, Hungary
[7] Observatori de l'Ebre, Univ. Ramon Llull – CSIC, 43520 Roquetes, Spain
[8] University of Massachusetts Lowell, Space Science Laboratory, Lowell, United States of America
[9] Kövesligethy Radó Seismological Observatory, Institute of Earth Physics and Space Science, Budapest, Hungary
[10] Leibniz-Institute of Atmospheric Physics, Kuehlungsborn, Germany
[11] SpaceEarth Technology, Rome, Italy
[12] Institute of Geophysics Czech Academy of Sciences, Prague, Czech Republic

***** Correspondence: **eng.hh@frederick.ac.cy**

Abstract: In this work, we investigate various types of ionospheric disturbances observed over Europe after the earthquake in Turkey on 6 February 2023.By combining observations from Doppler sounding systems, ionosondes, and GNSS receivers, we are able to discern different types of disturbances, propagating with different velocities and through different mechanisms. We can detect the co-seismic disturbances produced in the ionosphere close to the epicenter, as well the ionospheric signatures of acoustic waves propagating as a consequence of propagating seismic waves.

Keywords: Earthquake; Total Electron Content; TID; infrasound; ionosonde; CDSS

1. Introduction

On 6 February 2023, two earthquakes with magnitude $M_W > 7$ occurred in Turkey. The first shock was recorded at 01:17 UT with a magnitude of 7.8, while the second shock at 10:24 UT with $M_W = 7.7$ (Çetin et al., 2023; Dal Zilio & Ampuero, 2023; US Geological Survey, 2023). These primary shocks were followed by many aftershocks with magnitude lower than 7. Both major earthquakes happened in the region of the East Anatolian Fault, with the epicenters separated by about 95 km. The first event was located at 37.20°N, 37.13°E, and the second at 38.05°N, 37.25°E; both events took place at a depth of around 10 km (International Seismological Centre, 2023; Bondár & Storchak, 2011).
The work of Leonard & Barnes (1965) and Davies & Baker (1965) concerning the great Alaskan earthquake of 1964, has already demonstrated that major earthquakes can cause disturbances in the ionosphere. Since then, it has been established that these ionospheric disturbances are manifested as different types of earthquake induced travelling ionospheric disturbances (TIDs), propagating through different mechanisms (Astafyeva, 2019; Meng et al., 2019).
Co-seismic ionospheric disturbances are generated by waves travelling vertically up to the upper atmosphere in the vicinity of the epicenter (Afraimovich et al., 2001, Astafyeva & Afraimovich, 2006, 2019). As shown by Rolland et al., (2013) through model results, these vertically propagating acoustic waves are accelerated and deflected horizontally due to the variation of atmospheric parameters with altitude. As a result, such acoustic waves are detected as fast TIDs propagating radially outward from the epicenter. Co-seismic disturbances start travelling out from their origin at around 1000 m/s, the speed of sound at the height of the F layer, but have been observed to split at some distance from the epicenter into different modes travelling with velocities of about 600 and 3000 m/s (Astafyeva et al., 2009, Galvan et al., 2012).
On the other hand, seismic waves propagating out from the epicenter—in particular Rayleigh surface waves—can also generate acoustic-gravity waves propagating up to the ionosphere (Astafyeva et al., 2009, Rolland et al., 2011, Komjathi et al., 2016). These disturbances are expected to propagate at the speed of the Rayleigh waves, between 2000 and 5000 m/s, but with a delay of around ten minutes required for the vertical propagation of disturbances from the ground to ionospheric altitude (Lognonné et al., 2006; Astafyeva, 2019). Since seismic waves on the ground can reach long distances, this mechanism can produce disturbances in the ionosphere beyond the range where the shock-acoustic waves travelling through the ionosphere are attenuated (e.g., Maruyama et al., 2016a; 2016b)
Finally, there are acoustic-gravity waves travelling much slower, with velocities in the order of a few hundred meters per second (Astafyeva et al., 2009, Meng et al., 2019). Besides the various types of travelling disturbances, evidence of longer lasting impacts on the ionosphere, particularly close to the epicenter (Astafyeva, 2019, and references therein) has been reported. However, such effects are not considered here.
Earthquakes with $M_W > 6.5$ are expected to generate co-seismic disturbances in the ionosphere (Perevalova et al., 2014). The amplitude of ionospheric disturbances and the distance from the source at which they can be detected are of course dependent on the magnitude of the event, see for instance Heki (2021). In addition to the earthquake magnitude, the depth and the focal mechanism (Astafyeva & Heki, 2009) are also decisive factors that affect the excitation and propagation of TIDs. On top of these primary earthquake attributes, additional factors such as atmospheric conditions (Rolland et al., 2011) and the orientation of the geomagnetic field (Astafyeva & Heki, 2009; Zettergren & Snively, 2019) also define the characteristics of possible

ionospheric disturbances based on the coupling between the movement of the ground surface and the upper atmosphere.

Thus, a complex view of a superposition of different types of travelling ionospheric disturbances is observed after an earthquake, which differs significantly from one event to another. Besides different modes of TIDs, also ionospheric signatures of infrasound can be observed in the aftermath of major earthquakes (Chum et al., 2012; 2018a; Laštovička & Chum, 2017).

Ionospheric disturbances, including those resulting from an earthquake, can be detected using Doppler sounders (Liu et al., 2006; Chum et al., 2012), ionosondes (e.g., Maruyama, 2016a), or GNSS receivers that can facilitate TEC estimation (Calais & Minster, 1995; Afraimovich et al., 2001). This complementary view from observations from different instruments, is ideal for detecting different disturbance types (Astafyeva, 2019; Meng et al., 2019). In the European region, all these instruments are available in relatively dense observational networks (see Figure 1). Disturbances can be observed from a close proximity to the epicenter to distances over 3000 km, and therefore velocities can be calculated. The aim of this paper is to present an integrated picture of the various modes of TIDs generated during this event, as observed by different monitoring networks.

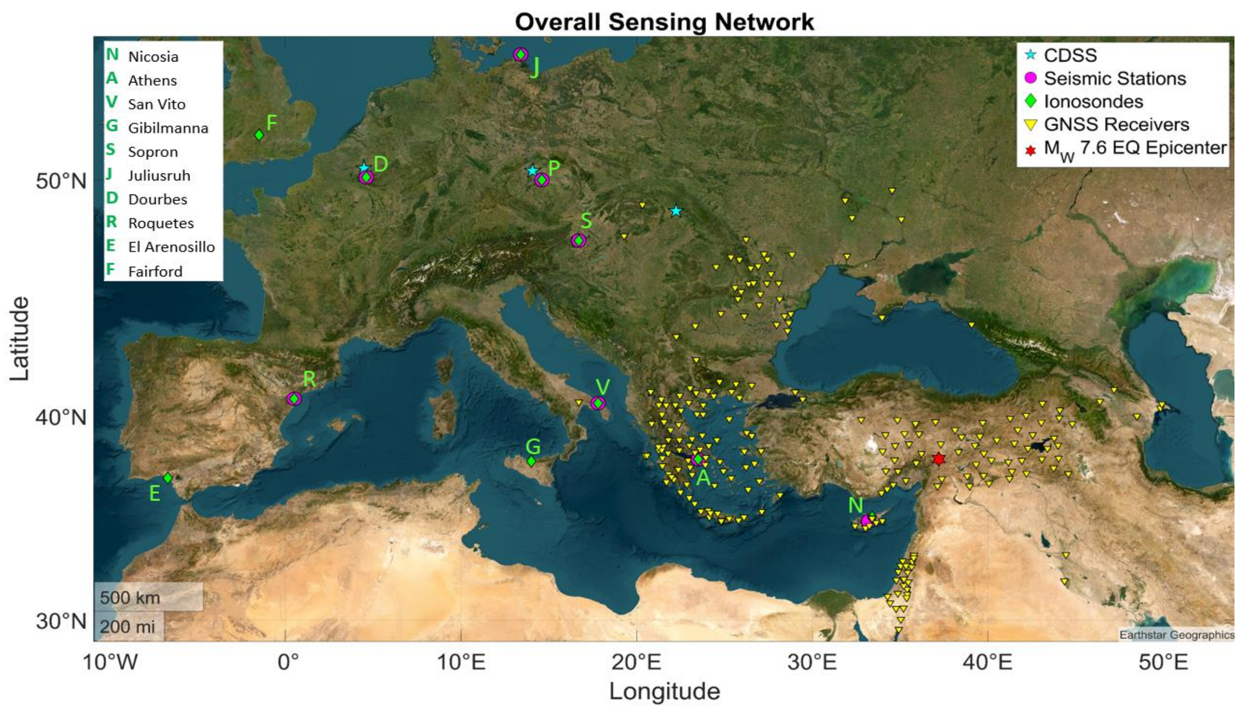

Figure 1. Map showing locations of instruments used for this study. The earthquake epicenter is also shown (red asterisk).

2. Data and Methods

2.1 Geomagnetic conditions

The Turkey earthquakes took place during the ascending phase of the 25th solar cycle.

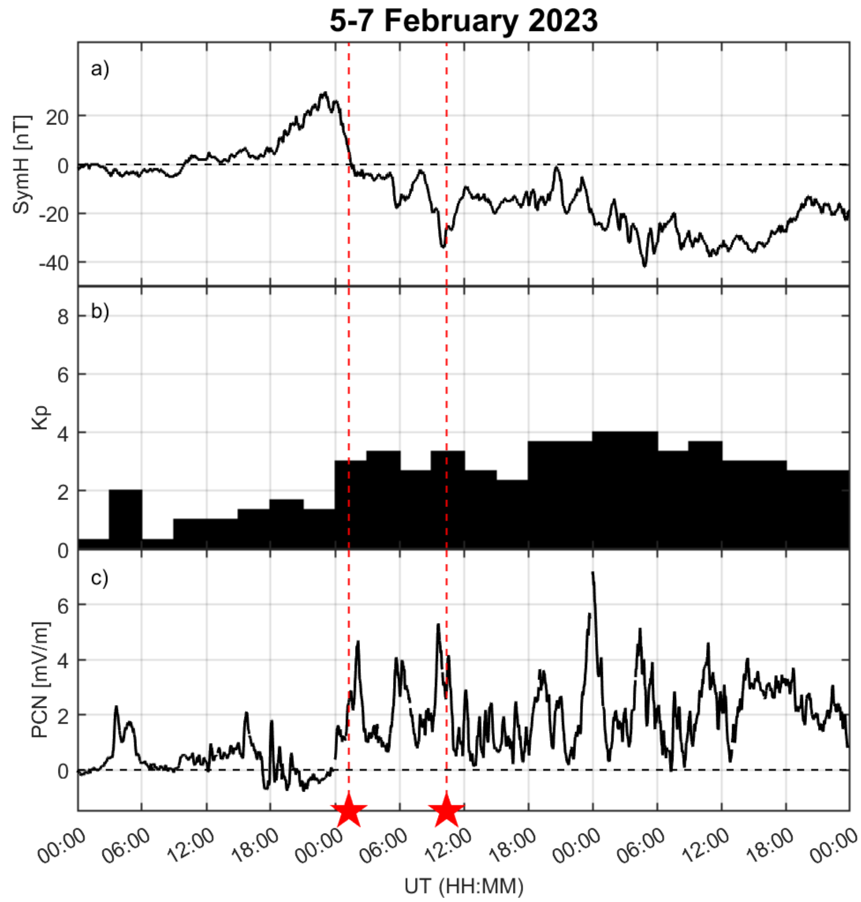

Figure 2. SymH (panel a), Kp (panel b) and Polar Cap North Index (panel c), in the period 5-7 February 2023. The red dashed lines and the corresponding stars indicate the time of the two main shocks (01:17 and 10:24 UT on 6 February 2023).

To quantify geomagnetic disturbances measured on the ground, the SymH (Li et al., 2011), Kp (Kaurisiti et al., 2017) and Polar Cap North (PCN) index (Stauning, 2013) have been considered. Figure 2 shows the time series of the respective indices in the period 5-7 February 2023, also indicating the time of the two main shocks (01:17 and 10:24 UT on 6 February 2023) in red. From the late evening of February 5, the solar wind speed increased, revealing the occurrence of a high speed stream (HSS) linked to a coronal hole in the northern solar hemisphere (Vanlommel, 2018). The solar wind speed slowly increased during 6 February and reached a speed of 600 km/s on 7 February. In correspondence with the passage of such a HSS and under favorable conditions of the Interplanetary Magnetic Field, geomagnetic disturbances covering the period under consideration are found. As reported in Figure 2a-c, these disturbance maximize in the early hours of 7 February (SymH= -42 nT, Kp=4, PCN=8.3). These solar driven disturbances manifested in the ionosphere as spread-F, visible during the nighttime in the higher latitude ionospheric observatories. In addition, the first main shock took place during a local winter night, when background ionization is low. Conversely, during the daytime a positive storm was observed with somewhat enhanced TEC values (Vanlomel, 2018). As a result of these conditions, no clear indication of ionospheric disturbances were detected over Europe after the first shock 01:17 UT, and the rest of this paper focuses on the second main shock at 10:24 UT.

2.2 Seismic context

The different types of seismic waves (body waves: primary P and secondary S, surface waves: Rayleigh waves LR and Love waves LQ) generated by the main shocks were identified at many seismic stations, some of which are located close to an ionosonde station (Figure 1). Figure 3 shows the appearance of seismic waves at various seismic stations co-located with an ionosonde station after the Mw 7.7 earthquake (T0 = 10:24:52 UT). The velocity of the seismic surface waves can be calculated based on the arrival times of the waves and the ground distance of the seismic stations from the epicenter (Table 1). The seismic data is available in the European Integrated Data Archive (EIDA, Strollo et al. 2021). The amplitude of seismic waves registered at Nicosia (ATHA station) were so strong that they caused saturation of the instrument. Determination of Rayleigh wave packets at stations closer to the epicenter is not easy in the case of such a large earthquake. Two types of surface waves (Love and Rayleigh waves) arrive with a minor delay with respect to the S phase. Furthermore, local effects can modify the shape of the waves. We considered the propagation speed of the LR waves to identify the correct Rayleigh arrival time to the different stations during the manual selection.

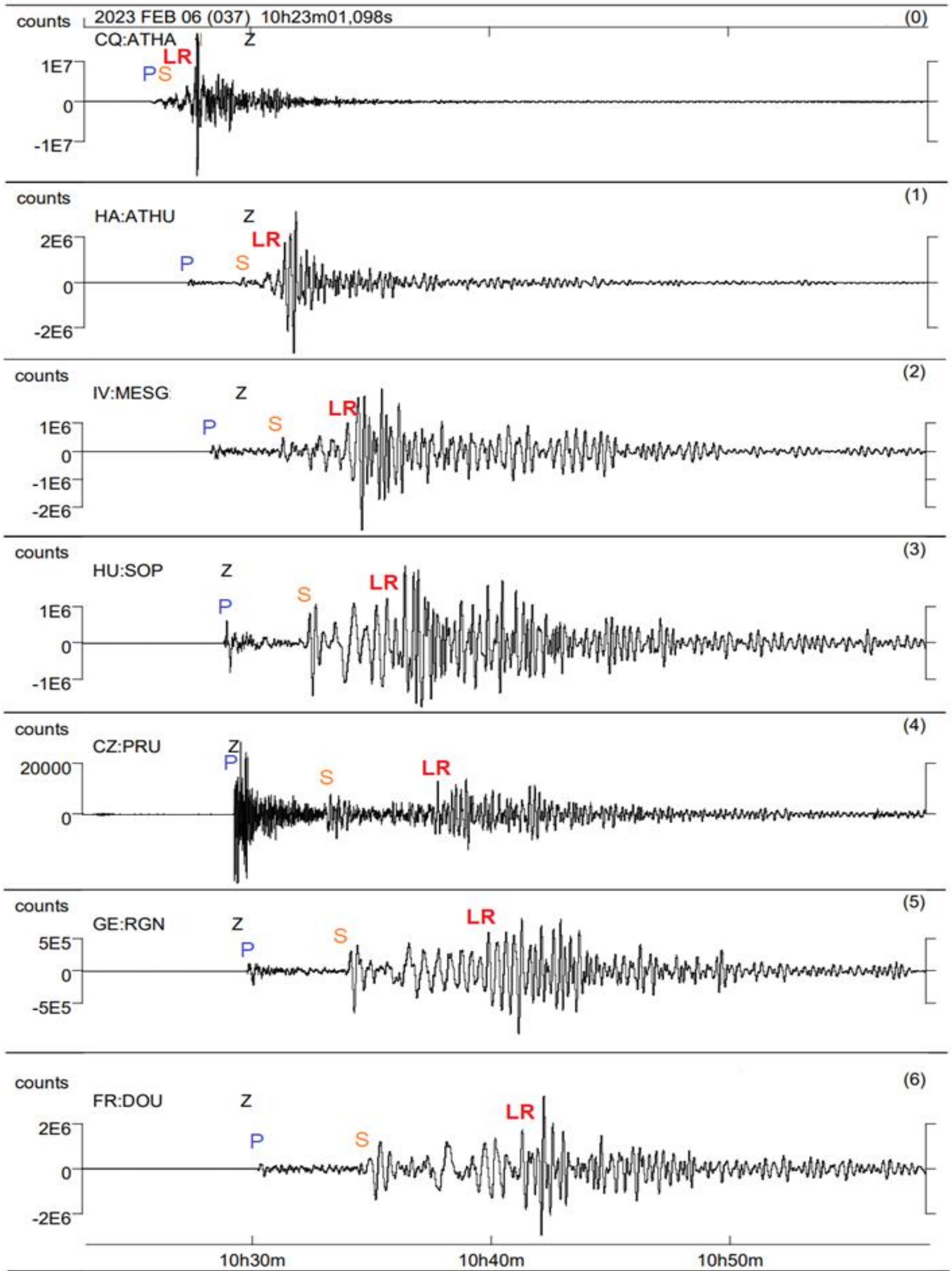

Figure 3. Vertical seismic wave component (Z) recorded at different seismic stations (close to an ionosonde station in Europe) as generated by the earthquake at 10:24 (UT), in order of increasing distance from the epicenter. "Counts" in the y-axis is the raw number read off the physical instrument, ie. the voltage read from a sensor. For example, a "count" value of 3.27508E9 would indicate ground motion of 1 m/s — you can divide the count value by 3.27508E9 to convert into meters per second. However, this multiplier varies from station to station. P, S and Rayleigh wave (LR) indicate the corresponding wave type in the subplots.

Name	Code	Geographic Latitude [ºN]	Geographic Longitude [ºE]	Distance [km]	Arrival times [UT]		
					P waves	S waves	Rayleigh wave
Athalassa, Cyprus	ATHA	35.1	33.4	460	10:25:52	10:27:07	-
Athens, Greece	ATHU	37.9	23.8	1199	10:27:22	10:29:23	-
Mesagne, Italy	MESG	40.6	17.8	1691	10:28:25	10:31:17	10:32:02
Sopron, Hungary	SOP	47.7	16.6	1975	10:29:02	10:32:17	10:32:40
Průhonice, Czech R.	PRU	50.0	14.5	2232	10:29:25	10:33:09	10:34:17
Ruegen, Germany	RGN	54.5	13.3	2574	10:29:56	10:34:07	10:36:31
Dourbes, Belgium	DOU	50.1	4.6	2900	10:30:25	10:34:53	10:37:23

Table 1. List of seismic stations, which are situated close to a European ionosonde station, in order of increasing distance from the epicenter: name, code and attributes (latitude, longitude, and distance from epicenter in km) of the stations, and the arrival time of different waves at the stations.

2.3 Continuous Doppler Sounding Systems

The European network of Continuous Doppler Sounding Systems (CDSS) currently consists of the multi-point and multi-frequency system operating in the Czech Republic at frequencies of 3.59, 4.65 and 7.04 MHz (Laštovička and Chum, 2017; Chum et al., 2021) and systems recently installed (at the end of 2022) in Belgium and Slovakia operating at frequencies of 4,59 and 3.59 MHz, respectively. Data from the Belgian transmitter in Dourbes (50.099°N, 4.591°E) received in Uccle (50.798°N, 4.358°E), the Czech transmitter located in Dlouha Louka (50.648°N, 13.656°E) received in Prague (50.041°N, 14.476°E), and the Slovak transmitter in Zahor (48.625°N, 22.205°E) received in Kolonica (48.935°N, 22.274°E), shown in Figure 1, were analysed in this paper. It should be noted that half distances between the transmitters and corresponding receivers are several times smaller than the reflection heights, so the zenith angle α of sounding radio waves is small and therefore $\cos(\alpha)\approx 1$. The surface horizontal distances of midpoints between the listed transmitter – receiver pairs in Belgium, the Czech Republic and Slovakia from the epicenter of the Turkey earthquake are about 2920, 2280 and 1700 km, respectively.

CDSS measure the Doppler shift that radio waves are subjected to, when reflected from the ionosphere due to the plasma motion and changes in electron density (Davies et al., 1962; Jacobs and Watanabe, 1966). CDSS have a relatively high time resolution (several seconds) due to the continuous sounding of harmonic radio waves of a specific frequency, but they do not provide any information about the reflection height, the region which contributes most to the observed Doppler shift (Chum et al., 2016a, 2018b). Therefore, it is useful to operate CDSS in the vicinity of an ionospheric sounder that can provide information on the CDSS sounding frequency reflection height, which is essential for a variety of studies (Chum et al., 2012; Chum et al., 2021). CDSS mainly detect medium scale travelling ionospheric disturbances (TID) or spread F (Chum et al., 2014; Chum et al., 2021), but they can also be used for the analysis of electric field that penetrates the ionosphere during geomagnetic storms (Kikuchi et al., 2021, 2022), infrasound generated by earthquakes (Artru et al., 2004; Chum et al., 2012, 2016a,b), typhoons and severe tropospheric weather (Georges, 1973; Chum et al., 2018a) or volcano eruptions

(Chum et al., 2023), ionospheric response to solar eclipses (Sindelarova et al., 2018; Liu et al., 2019), solar flares (Chum et al., 2018b) etc.

It was shown by Watada et al. (2006) that the near surface pressure fluctuations and air particle oscillation velocities w_0 are determined by the vertical component of the velocity of Earth surface motion, v_z. A high correlation between the waveforms of v_z for P and S seismic waves and air particle oscillation velocities w in the ionosphere determined from Doppler shift f_D were shown in (Chum et al., 2012). The similarity of spectral content of v_z and w (f_D) at large distances from the earthquake epicenter was discussed in (Chum et al., 2016a, 2018a). The co-seismic infrasound registered by CDSS during the earthquake under consideration was compared with ground surface vertical velocities v_z measured by seismometers and observed time delays between v_z and w (f_D) were compared numerical simulation using ray tracing code described in previous works (e.g., Chum et al., 2023). In addition, the values of w obtained from measured Doppler shifts were compared with the amplitudes of w expected for infrasound propagating up to the CDSS reflection heights assuming a linear theory of propagation and attenuation due to the viscosity, thermal conductivity and rotational relaxation (Bass et al., 1984; Chum et al., 2012). The air particle oscillation velocity w was estimated from the Doppler shift f_D using the approximate formula (1) derived in (Chum et al., 2016a) for (quasi)vertical sounding and (quasi)vertically propagating infrasound.

$$w = -f_D \cdot \frac{c}{2f_0 sin^2(I)} \cdot \frac{\frac{\partial N}{\partial z}}{\sqrt{(\frac{\partial N}{\partial z})^2 + (N\frac{2\pi f_{IS}}{c_S})^2}}, \qquad (1)$$

where c is the speed of light, f_0 is the sounding frequency, I is the inclination of geomagnetic field, N is the electron density at the reflection height, $\partial N/\partial z$ is the vertical gradient of electron density at the reflection height estimated from the ionogram, f_{IS} is the infrasound frequency and c_s is the sound speed. The term $N\cdot(2\pi f_{IS})/c_s$ results from the air and plasma compression due to the infrasound waves. If $\partial N/\partial z >> N\cdot(2\pi f_{IS})/c_s$, equation (1) reduces to (2)

$$w = -f_D \cdot \frac{c}{2f_0 sin^2(I)} \qquad (2)$$

which is a relation that directly follows from the vertical plasma velocity w_p, computed from the Doppler shift f_D by standard equation (3)

$$w_p = -f_D \cdot \frac{c}{2f_0}, \qquad (3)$$

assuming that (quasi)vertically propagating radio waves reflect from the magnetized plasma, where electrons freely move only along magnetic field lines and are forced by vertically oscillating air.

2.4 Ionograms

An ionospheric earthquake-related signature established as a deformation on ionograms is the multiple-cusp signature ("MCS") which appears as additional cusps that can be attributed to electron density irregularities giving rise to stationary points of inflection in the vertical electron density profile as discussed by Maruyama, et al. (2011, 2012, 2014). This ionogram signature is shown in Figures 7 and 8 for several ionospheric stations and may be interpreted as an indication of the propagation of an acoustic wave as the separation of these points of inflection reflects the infrasound wavelength in the thermosphere. For this particular event all ionosondes considered were situated towards north-west with respect to the epicenter with the exception of the nearest ionosonde to the epicenter located at Nicosia which is positioned south-west with respect to the epicenter. All eleven ionosondes across Europe considered in this study along with their respective ionogram cadence are tabulated in Table 2 in accordance to their distance from the epicenter. Their location is also shown in Figure 1.

Station	URSI Code	Geographic latitude	Geographic longitude	Ionogram Cadence (Min)	Distance From Epicenter (km)
Nicosia	NI135	35.2°N	33.4°E	5.0	460
Athens	AT138	38.0°N	23.5°E	5.0	1199
San Vito	VT139	40.6°N	17.8°E	7.5	1691
Gibilmanna	GM037	37.9°N	14.0°E	15.0	2029
Sopron	SO148	47.6°N	16.7°E	5.0	1975
Průhonice	PQO52	50.0°N	14.6°E	15.0	2232
Juliusruh	JR055	54.6°N	13.4°E	5.0	2574
Dourbes	DB049	50.1°N	4.6°E	5.0	2900
Roquetes	EB040	40.8°N	0.5°E	5.0	3146
Fairford	FF051	51.7°N	-1.5°E	7.5	3358
El Arenosillo	EA036	37.1°N	-6.7°E	5.0	3835

Table 2. European ionosondes used in the study, arranged according to distance from the earthquake epicenter.

2.5 GNSS derived TEC

To investigate the ionospheric signatures in Total Electron Content (TEC) we used a collection of GNSS networks spanning different distances and azimuthal directions with respect to the epicenter (shown as yellow inverted triangles in Figure 1). Data from 1s and 30s RINEX files were used, with 1s as the preferred time resolution due to the relatively short period expected from co-seismic TID (Astafyeva, 2019). The GNSS stations used belong to many different institutions and networks, specifically INGV (Michelini et al., 2016), TUGASA-Aktif (Ouml et al., 2011), CYPOS (Danezis et al., 2019), NOA (Chousianitis et al., 2021), IGS (Dow et al., 2009), and EUREF (Torres et al., 2009). To extract TEC perturbations, we used the dual frequency geometry-free linear combination of carrier-phase measurements. The TEC along the satellite-receiver line of sight can be calculated starting from phase measurements as follows:

$$sTEC_{phase} = \frac{1}{40.308}\frac{{f_1}^2{f_2}^2}{{f_1}^2-{f_2}^2}(L_1\lambda_1 - L_2\lambda_2) \quad (4)$$

Where $sTEC_{phase}$ is the ambiguous slant TEC; L_1, L_2 are the phase measurements of the radio signal for the L_1 and L_2 bands defined by their frequency f_1, f_2 and wavelength λ_1, λ_2. By doing so, we obtain an uncalibrated version of sTEC, which is strongly related to the observational elevation. Normally, sTEC is vertically mapped to better compare TEC time-series for different stations and satellites. However, filtering and detrending such an uncalibrated observable would prevent the estimation of the wave amplitude since the calibration bias would be multiplied by the mapping function, causing an amplification of the wave amplitude, especially for low-elevation angles (Verhulst et al., 2022). To prevent or somewhat limit such amplification effect, we employed NeQuick 2 (Nava et al., 2008), a climatological model that provides a TEC estimate between two given points (in our scenario, the initial GNSS station and satellite position). Using this model, we can assign an initial sTEC value between the corresponding GNSS receiver and satellite, which limits by the "verticalization" process. To investigate the spatial behavior of the co-seismic TID, we rely on the widely-used thin-layer ionospheric approximation (Mannucci et al., 1998), with the shell height set to 250 km. To extract the TID signature from the vTEC, we use a bandpass filter based on the novel Fast Iterative Filtering technique (Cicone & Zhou, 2021). This technique can decompose non-stationary, non-linear signals into simple oscillatory components (Madonia et al., 2023; Verhulst et al., 2022) called Intrinsic mode functions, each defined by its quasi-stationary frequency. By summing those modes that fall into the frequency band of interest for each time step, we extracted the detrended TEC (dTEC).

3. Observations and Discussion

3.1 CDSS

Figure 4 shows the Doppler shift spectrograms recorded by CDSS in Slovakia, the Czech Republic and Belgium after the M=7.7 Turkey earthquake on 6 February 2023. All four spectrograms show disturbances caused by infrasound waves. The Doppler shift fluctuations are not very clear in Slovakia, which prevents further analysis. However, Doppler shift time series could be obtained from maxima of spectral densities in the Doppler shift spectrograms recorded in the Czech Republic and Belgium and were used for further analysis.

Figure 5 displays the vertical component of the ground surface velocity v_z measured in Panská Ves, Czech Republic (plot a) and vertical plasma velocity w_p and air particle oscillation velocity w derived from the Doppler shift time series obtained from CDSS operating at f=4.65 MHz and 7.04 MHz (plots b and c, respectively). The fluctuations of w_p (w) in the Czech Republic derived from the 4.65 MHz signal are shorter than those derived from 7.04 MHz signal due to the low quality Doppler shift spectrogram after ~10:47 UT (Figure 4.b). The long-term variations, seen mainly in plots c in Figures 4 and 5 are caused by TIDs not related to the earthquake. On the other hand, the fast variations are due to the infrasound with a period about 20 s and clearly correspond to the variations of v_z shown in Figure 5.a. In particular, the similarity between v_z and

w_p *(w)* for the first pulse (around 10:29:40 UT in v_z), which correspond to P seismic waves is remarkable. The corresponding signatures in the ionosphere recorded by the CDSS are delayed about 485 s for the 4.65 MHz sounding and about 515 s for the 7.04 MHz sounding. A clear similarity between v_z and w_p *(w)* is also observed for the second pulse (around 10:33:32 UT in v_z) corresponding to S seismic waves. The S waves are then followed by Rayleigh waves of higher amplitude and by their corresponding ionospheric signatures. The bottom plots (d) and (e) show ground velocity v_z and the corresponding plasma velocities w_p and air particle oscillation velocities w estimated from CDSS observation in Belgium.

Figure 6 shows the ray tracing simulation results for acoustic waves with a period of 20 s for a realistic atmosphere over the Czech Republic including the neutral horizontal winds obtained by HWM14 model (Drob et al., 2015) on 6 February 2023 at 10:45 UT. The ray tracing was initialized with zenith angles from 2° (red) to 6° (blue). This range covers the expected initial zenith angles α_0, given by the ratio c_{S0}/c_G, $\sin \alpha_0 = c_{S0}/c_G$, where c_{S0} is the near surface sound speed and c_G is the speed of seismic waves (Rolland et al., 2011; Chum et al., 2016a). The ray tracing extended up to an altitude of 300 km. The rays reach the altitudes of about 170 km and 190 km for the observed time delays of 485 s and 515 s, respectively (Figure 6.c), which is consistent with CDSS reflection heights derived from ionograms measured by the nearby Digisonde at Průhonice. Figure 6.b shows the calculated infrasound attenuation along the ray trajectories, related to the initial, near surface infrasound amplitude. The attenuation is also plotted in an alternative way in Figure 6.d, which shows the ratio w/w_0, which is the ratio of air particle oscillation velocities w at a specific height to the velocities w_0 ($w_0=v_z$) near the ground surface. The solid line represents the unrealistic case of lossless propagation (no attenuation).

The simulated ratio w/w_0 can be compared with the measured values v_z, w and w_p (w/v_z, and w_p/v_z) presented in Figure 5 (note different scales for v_z, w and w_p). The measured ratio w_p/w_z is about 50 000 and the ratio w/w_z obtained using equation (1) is about 5000. It should be stressed that the ratio w_p/w_z and hence the ratio w/w_z calculated by equation (2) is higher than the theoretical limit (about 28 000 at the height of 170 km) for lossless propagation (solid line in Figure 6.d) and significantly larger than the estimated/modeled ratio (about 15000 at 170 km) considering the attenuation. From this, it follows that the compressional term in equation (1) cannot be neglected when deriving the air velocities from the measured Doppler shift f_D. It should be remembered that there is a large uncertainty in electron density gradient derived from ionograms (~ $6{\cdot}10^6$ m^{-4} at 170 km and ~ 10^7 m^{-4} at 190 km). This may be one of the reasons why the measured ratio, of approximately 5 000 according to equation (1), is lower than the modelled one (~15000 at 170 km and ~11000 at 190 km). Another reason is the divergence of infrasound ray trajectories (geometrical factor) that is not taken into account in the simulation. The actual attenuation of wave energy is expected to be stronger due to the ray divergence than that shown in Figures 6.b and 6.d.

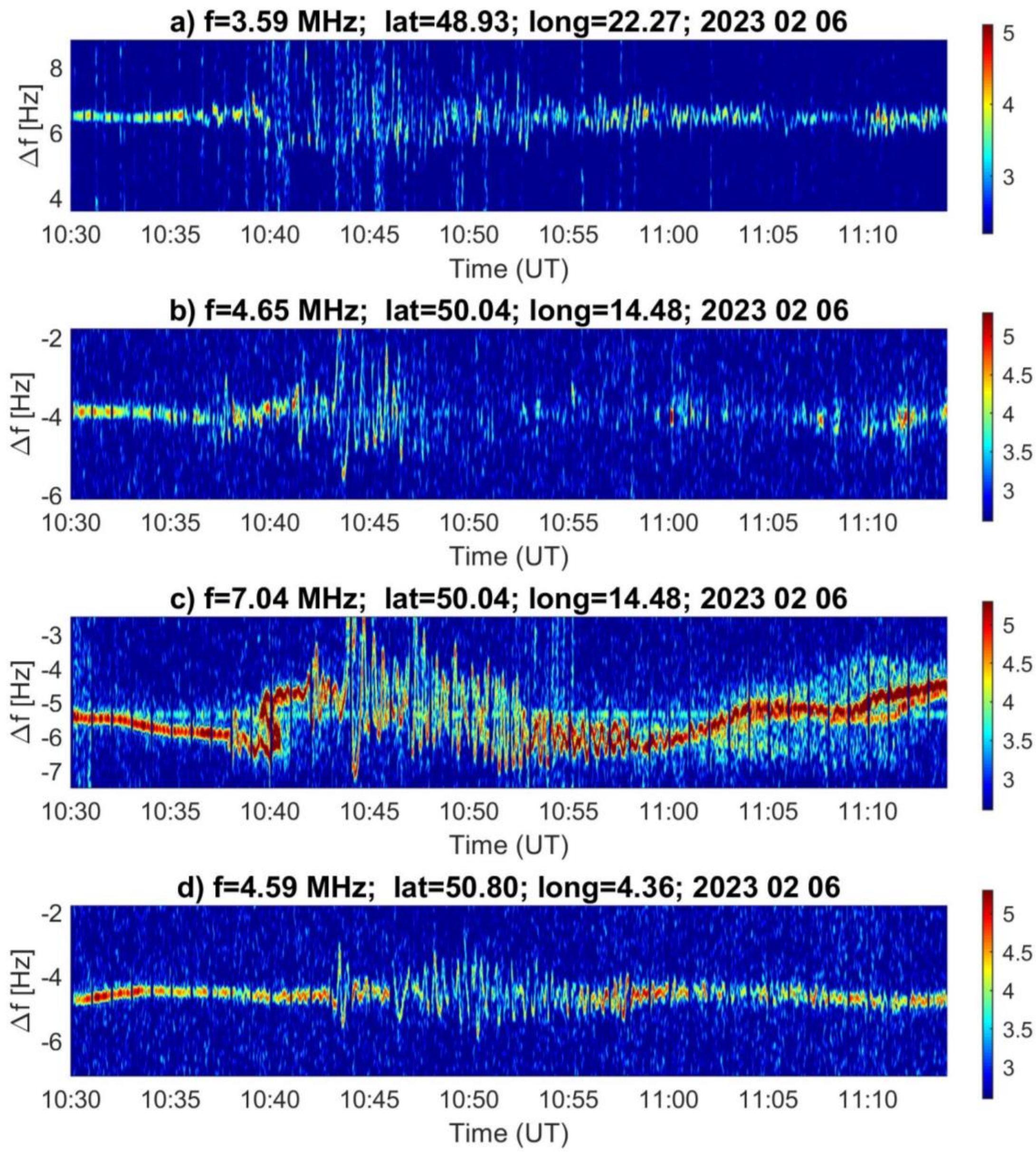

Figure 4. Doppler shift spectrogram recorded for selected sounding paths in (a) Slovakia, (b, c) Czech Republic at f=4.65 and 7.04 MHz, respectively (d) Belgium from 10:30 to 11:15 UT on 6 February 2023

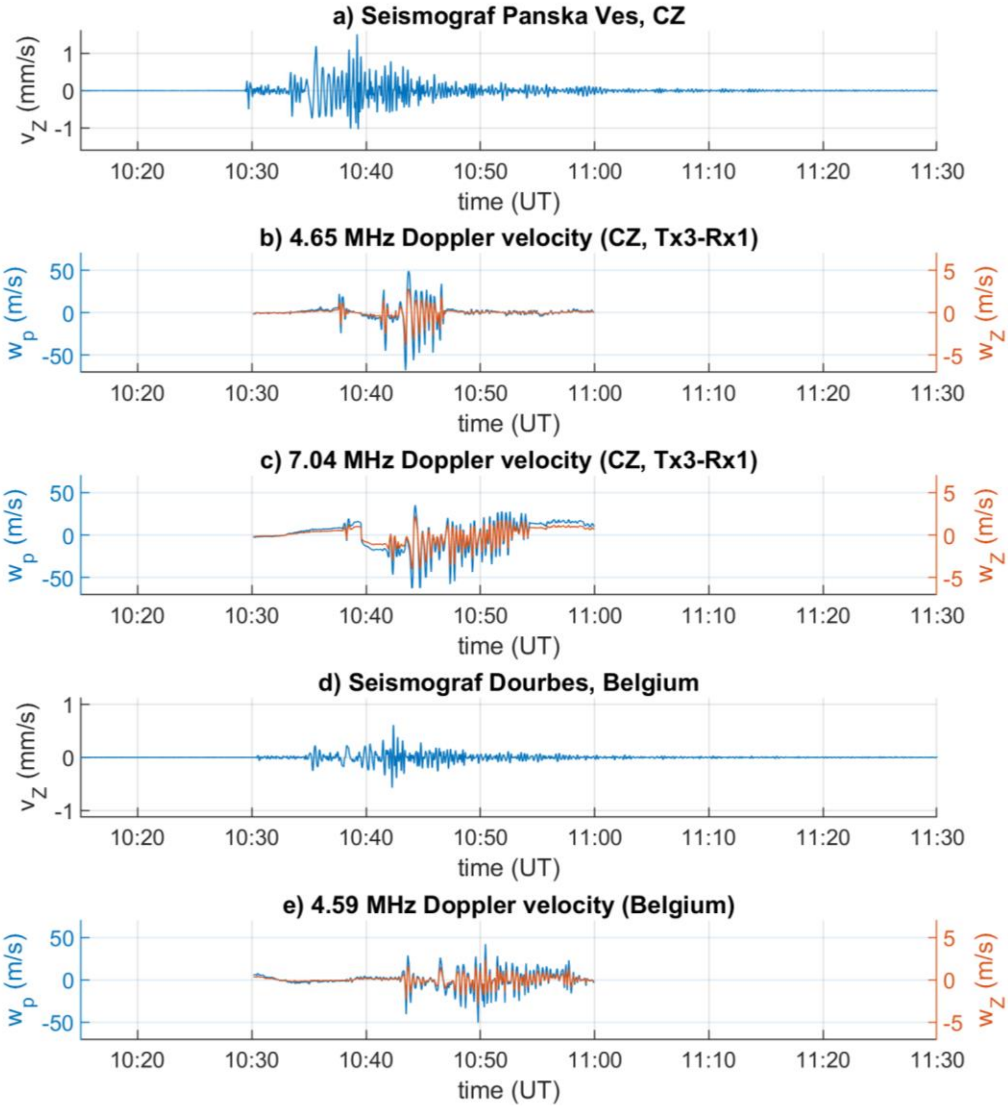

Figure 5. (a) Vertical velocity v_z of ground surface in Panska Ves, Czech Republic, (b), (c) vertical plasma velocity w_p (blue) and air particle velocity w_z (red) derived from measured Doppler shift by CDSS in the Czech Republic at 4.65 and 7.04 MHz, respectively, (d) Vertical velocity v_z of ground surface in Dourbes, Belgium and (e) vertical plasma velocity w_p (blue) and air particle velocity w_z (red) derived from measured Doppler shift by CDSS in Belgium at 4.59 MHz.

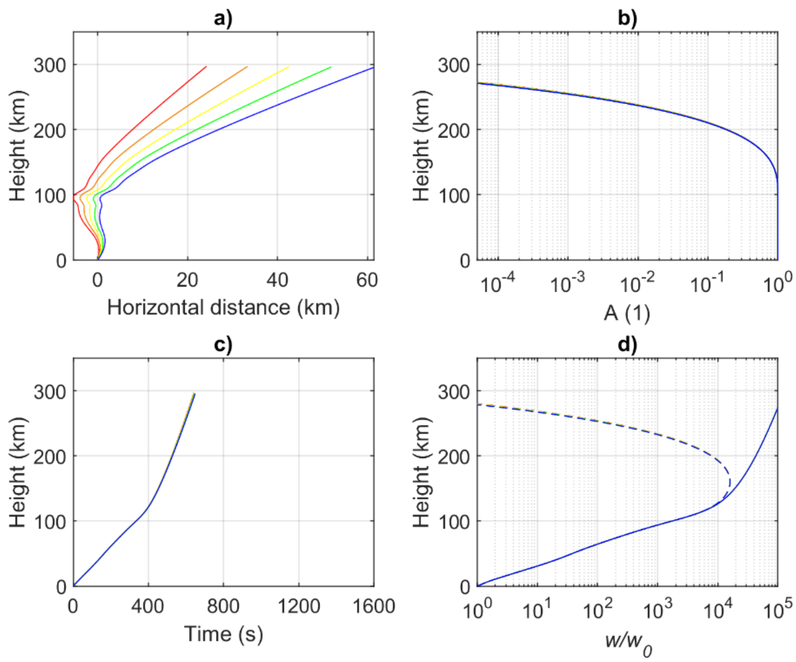

Figure 6. Ray tracing results for the infrasound waves started from the surface with zenith angle 2° (red) to 6° (blue). (a) Ray trajectories in vertical cross-section along the wave vector of seismic waves, (b) Attenuation as a function of height (relative to initial value) calculated by the analytic model assuming the wave period of 20 s, (c) Height as a function of time and (d) Ratio of air particle oscillation velocities w at a specific height related to the near surface value w_0. Solid line represents the lossless propagation.

The CDSS did not detect any co-seismic disturbances related to M=7.8 earthquake that occurred at night at 01:17:35 UT on the same day, 6 February 2023. The main reason besides the low critical frequency *foF2* (only 3.59 MHz systems experienced reflection from the ionosphere) was the high altitude of reflection (about 340 km). The simulation in Figure 6 clearly demonstrates that infrasound waves of 20 s period are strongly attenuated above about 250 km and cannot be detected by CDSS at such altitudes.
A similarity between the waveforms and spectra of the vertical ground surface velocity v_z and the air particle oscillation velocity w determined from the observed Doppler shift f_D indicates that the propagation of infrasound to the altitudes of observation in central Europe was linear. The velocities v_z and hence the initial near surface perturbations w_0 were not large enough to lead to the nonlinear phenomena in the upper atmosphere that have been observed by CDSS in the vicinity of strong earthquakes (Chum et al., 2016b; Chum et al., 2018a).

3.2 Ionograms

Each row in Figures 7 and 8 represents two ionograms for each of the ionosonde stations listed in Table 2. Here the left column shows the latest seismic undisturbed ionogram. On the corresponding ionograms for each of these stations a few minutes later (in the right column), clear multi-cusp signatures are seen. The difference in the consecutive ionograms is particularly evident at Nicosia, Athens, Gibilmanna, Juliusruh, Dourbes and Fairford. The disturbances appear to be limited to the lower F region and the cusps are particularly sharp-edged in the case of Juliusruh, Dourbes and Fairford. The cusps for San Vito, Sopron Roquetes and El Arenosillo are faint, but can still be identified when the traces are compared with the respective regular ionograms on the left.

Considering ionograms from all ionosondes involved, we were able to detect clear “MCS” on ionograms from almost all stations (with the exception of Průhonice) after 10:35 UT at which the first signature appeared at the 10:35 UT Nicosia ionogram, which is in line with the arrival of the acoustic wave in the ionosphere at approximately 10 min after the seismic disturbances generated by the 10:24 UT shock (indicated with the vertical line) as indicated in Figure 9. The appearance of the Rayleigh and Love wave signature in the ionosphere is delayed because of the propagation time of the atmospheric waves from the ground into the ionosphere after the seismic disturbance has reached the ionosonde location. In fact, associated “MCS” can be identified in the subsequent ionograms on more distant stations (as ionograms from top to bottom in Figure 7 and Figure 8 are ordered in accordance to their distance from the epicenter). Despite the fact that, ionograms at Průhonice (PQ052), due to some technical problem with the ionosonde at the time, do not contain correct polarization and direction of arrival information, the time of arrival of individual signals is, reliable. In other words – we can use the individual traces on the ionogram, but we cannot use the color codes of the signal for interpretation.

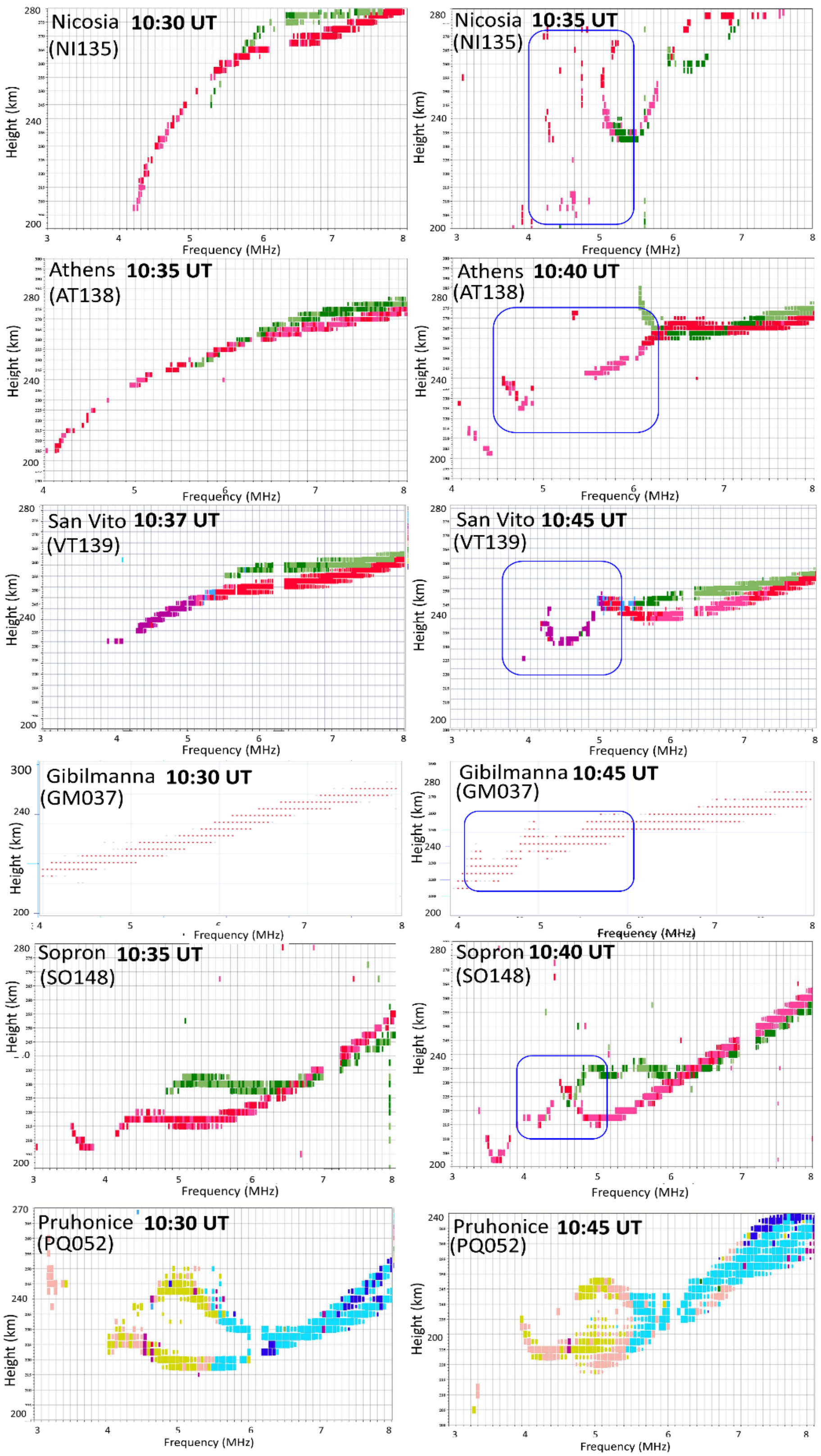

Figure 7. Successive ionograms at European stations (from top to bottom: Nicosia, Athens, San Vito, Gibilmanna, Sopron, Průhonice) registering a clear multiple-cusp signature ("MCS").

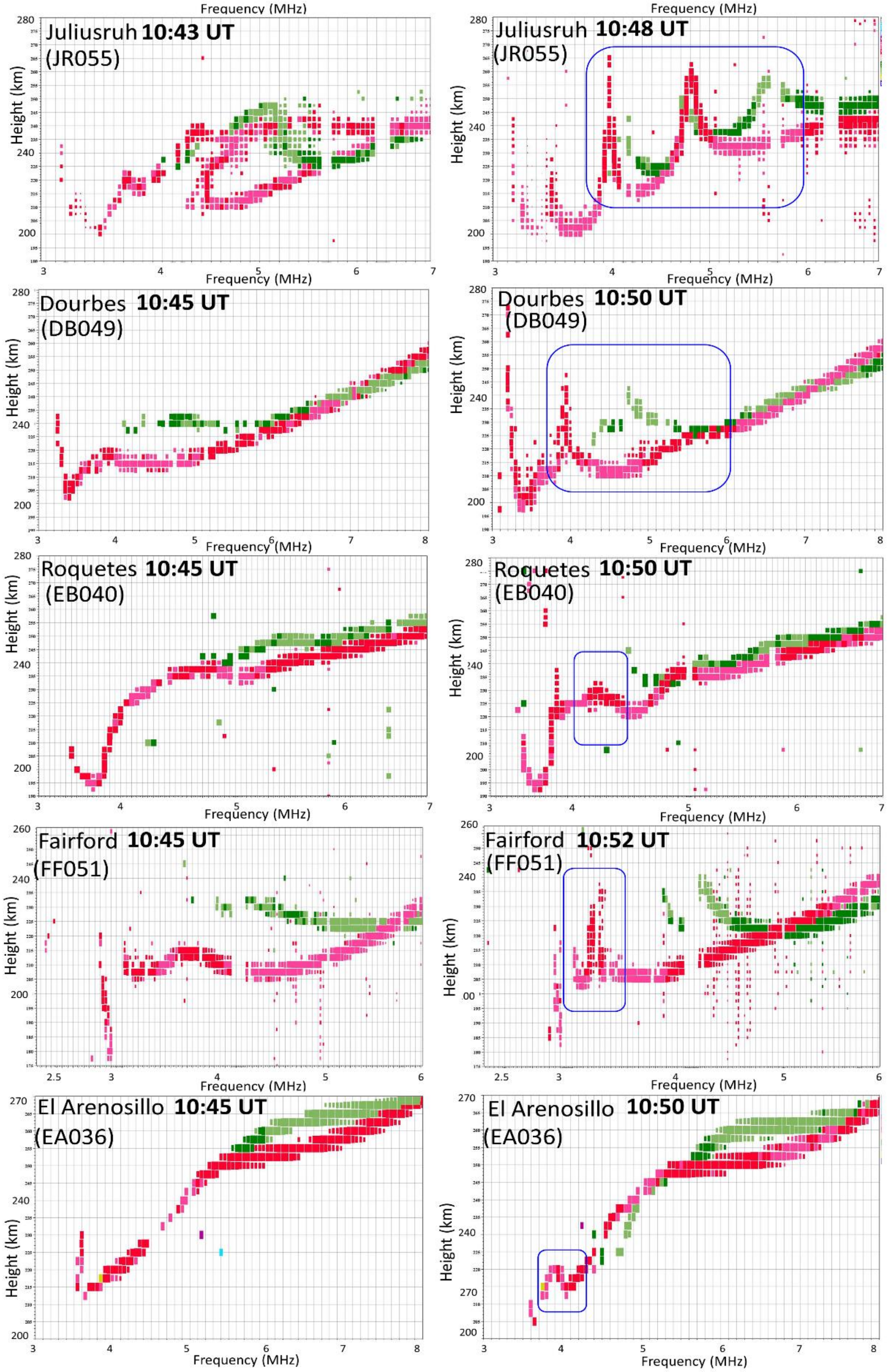

Figure 8. Successive ionograms at European stations (from top to bottom: Juliusruh, Dourbes, Roquetes, Fairford, El Arenosillo) registering a clear multiple-cusp signature ("MCS").

Figure 9 shows the time (horizontal axis) of the first acquisition of an ionogram with a “MCS” after the earthquake (red circle) with respect to the previous unaffected ionogram (white circle) as well as the time of the main shock (10:24 UT) as indicated by the red star on the x axis. Apparently we can draw a line through these points with a slope approximating the disturbance propagation velocity but clearly there exists an ambiguity in defining this line as ionograms were conducted at intervals of 5 to 15 min (Table 2). This ambiguity for each station is also reflected on the time difference between red and white circles for each ionosonde (dotted line connecting the two circles).

Compared to the high-temporal resolution provided by 1 s RINEX files in the GNSS analysis shown in section 3.3 ionosondes are operated typically at a much lower temporal resolution according to which they perform an ionogram measurement every 5-15 min intervals (as indicated by consecutive ionograms from various European stations in Figures 7 and 8). During such a time interval, an acoustic wave would cover a distance of more than 250 km under a sound velocity assumption of 0.8 km/s. Unless the ionosonde operates on a campaign mode where it performs an ionogram measurement every 30 s or 1 min it is not realistic to detect a clear typical “MCS” on consecutive ionograms.

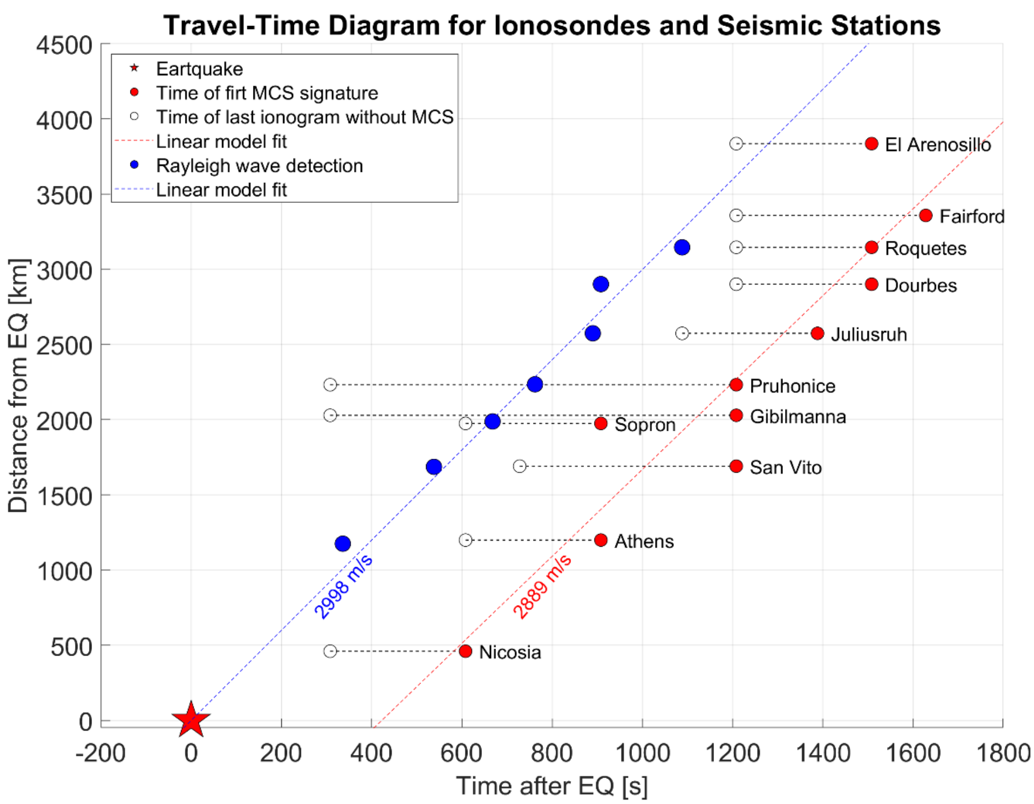

Figure 9. Travel-time diagram of co-seismic ionospheric disturbances causing “MCS”s at each station.

It is interesting to relate the time of arrival of the P, S and most importantly Rayleigh waves according to the recordings of the seismic stations shown in Table 1 and the “MCS” appearance on the ionograms indicated in Figures 7 and 8 considering the corresponding time ambiguity based on the length of the line connecting each pair of white and red circles. For example between Nicosia (nearest location to the epicenter as shown in Figure 1) and Athens, the difference in the time of arrival in the P waves (10:25:52 at Nicosia and 10:27:22 at Athens) and

S waves (10:27:07 at Nicosia and 10:29:23 at Athens) is around 1-2 min (Rayleigh waves saturate the measurements at both seismic stations) whereas the “MCS” appears clearly on ionograms that are 5 min apart (10:35 at Nicosia and 10:35 at Athens). For the San Vito ionosonde we also have a definite estimation for the arrival of Rayleigh waves (10:32:02) the “MCS” appears on the 10:45 ionogram, which is beyond the 8-10 min delay relative to the Rayleigh waves arrival at the corresponding seismic station (MESG). However, we can identify that the “MCS” is not so evident for that specific case as compared to other stations (Nicosia, Athens Juliusruh and Dourbes). In particular, for Dourbes and Juliusruh the time difference in the Rayleigh wave arrival (10:36:31 at Juliusruh and 10:37:23 at Dourbes) is comparable to the time difference of a similar “MCS” appearance on the corresponding ionograms (10:48 at Juliusruh and 10:50 at Dourbes) which underlines the clarity of the “MCS” as a function of the time with respect to the ionogram measurement. This emphasizes the importance of the ambiguity depicted in Figure 9 with respect to the clear identification of “MCS” signatures at each station and the subsequent capability to determine the acoustic wave propagation in the ionosphere based on “MCS”. Although not included in Table 1 but considered in Figure 8, the arrival time of the Rayleigh wave in the Spanish seismic stations ERTA and CMAS was at approximately 10:43 UT. The ionospheric station Roquetes (EB040) in Spain recorded the “MCS” irregularities at 10:50 that compared to the arrival time of the Rayleigh wave identified on the nearest station seismogram at 10:43, this would result in an estimated travel time of the irregularity from ground to the ionosphere of about 7-8 minutes. The latter agrees well with the estimated travel time of about ten minutes required for the vertical propagation of disturbances from the ground to ionospheric altitude (Lognonné et al., 2006; Astafyeva, 2019). The small timing differences discussed above may be also attributed to the fact that ionograms provide information on a wide area of the sky over the measuring site and not over a single point but also on differences on the radiation patterns of transmitting and receiving antennas at the ionosonde sites. A notable conclusion that we can infer from Figure 9 stems out of the parallel red and blue lines indicating the ionospheric disturbance propagation and the corresponding driver of this disturbance which is the Rayleigh wave on the surface, respectively. If we accept that MCS signatures correspond to perturbations of the electron density profile around an altitude of 140 km then the time shift of approximately 400 sec between the two (almost parallel blue and red lines) would infer a propagating upward velocity of this acoustic wave from the surface to the bottom of the F-layer at a velocity of 350 m/s.

3.3 GNSS

Once dTEC and the Ionospheric Pierce Points (IPPs) locations were calculated, we investigated the TID propagation in space through a travel-time diagram (TTD), a technique widely used to estimate velocities and time of arrival of co-seismic ionospheric waves at different locations (Astafyeva, 2019; Astafyeva et al., 2009). Moreover, we expanded the TTD further by dividing it into four sub-panels (Panel (c) of Figures 10, 11 and 12) each corresponding to different azimuthal ranges with respect to the earthquake epicenter. This modification facilitates the investigation of the anisotropies in the TID propagation and parameters, which is expected for co-seismic TIDs (Zettergren & Snively, 2019).

Figures 10, 11 and 12 show the aforementioned diagram for PRN17, PRN49 and PRN58 respectively. Note that the satellites considered were not the only ones showing clear TID signatures, but were chosen because they show the signature of both the shock acoustic wave (Afraimovich et al., 2001; Astafyeva et al., 2009; Heki & Ping, 2005) and the Rayleigh wave induced TID (Ducic et al., 2003; Rolland et al., 2011). The left Panels show the TTD itself, with the X and Y axis representing the distance in time and space to the earthquake. Panels (a) show the spatial distribution of IPPs, the epicenter location and its isodistances. Because of the TID being ion density waves, the coupling of the neutral and ionized particles is maximal along magnetic field lines since ion movement is mainly restricted along magnetic field lines (Bagiya et al., 2019; Rolland et al., 2013). Thus, when investigating the different azimuthal features we need to take into account that over Turkey the inclination and declination of magnetic field lines are respectively around 55 and 5 degrees. Panels (b) show the TTD for the stations shown in Panels (a). Note that the network used was denser than the one visible in Figure 1 (overall network figure), because we decided to show only those station-satellite links with a clear signature. Discarding such links also enabled the investigation of a possible preferred azimuth of propagation by comparing the original spatial distribution and the one of Panels (a). Specifically, we decided to plot only those arcs that showed a TID amplitude higher than 0.05 TEC units (TECu). In addition, the IPP tracks are colored according to the initial arc azimuth to the epicenter to highlight the different wave patterns. Finally, Panels (c) show a slightly different TTD, where blue and red points correspond to negative and positive TEC perturbations. Moreover, the TTD here was split into four different subpanels, each showing a different azimuthal range with respect to the epicenter. Thus, the main difference between Panels (b) and Panels (c) is that the distance shown in Panels (b) is the distance of the given IPP at the time of maximum dTEC, while Panels (c) show its time evolution.

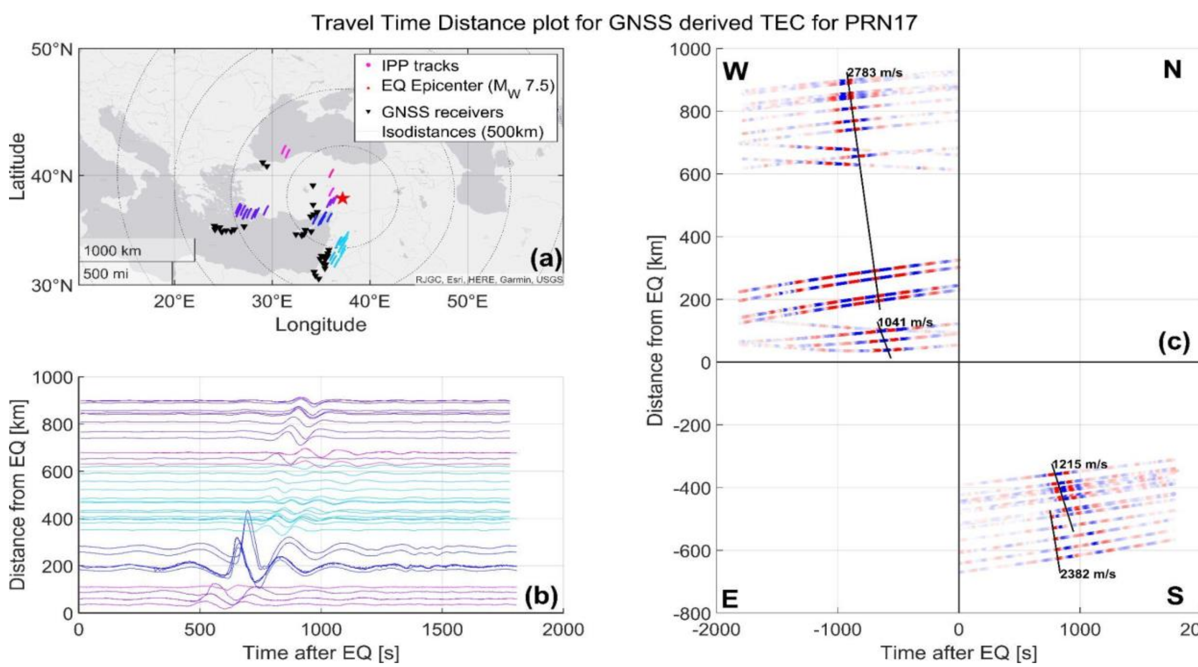

Figure 10. (a) Spatial distribution of IPPs and the epicenter location (b) Travel-time diagram for the stations shown in (a) and (c) Travel-time diagram for different azimuth for PRN17.

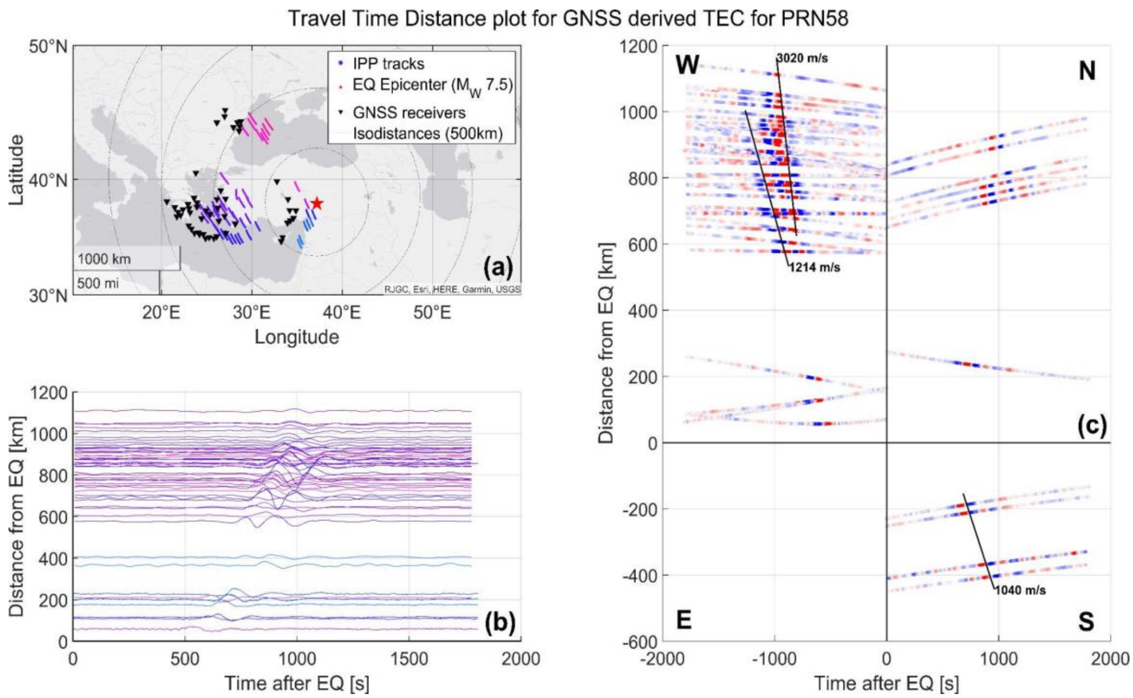

Figure 11. (a) Spatial distribution of IPPs and the epicenter location (b) Travel-time diagram for the stations shown in (a) and to be completed. (c) Travel-time diagram for different azimuth for PRN58.

Thanks to the combination of the two TTDs, we can investigate the waveform and amplitude along with the propagation velocities for different azimuthal ranges. First, Panel (b) of Figure 10 shows how a narrow azimuthal range presents a large amplitude. If we look at the corresponding IPP tracks, color-coded as in Panel (b), we can discern which geographical area these azimuths correspond to. Such waveforms are related to GNSS stations located in Cyprus, and the likely reasons for such this large amplitude could be the observational geometry (IPPs for PRN17) are actually situated over the epicenter) and earthquake characteristics (such as fault alignment and focal mechanism (Astafyeva, 2019; Astafyeva & Heki, 2009). The possible impact of such effects will be discussed below. The waveform visible in all the Panels (b) resembles the typical acoustic N shape, corresponding to an initial overpressure half cycle with a steep rise-time and a slower pressure decay followed by a half cycle of rarefaction (Astafyeva, 2019).

Panels (b), indicate waves of different nature we know from the literature to be produced by earthquakes. The first TID type, the co-seismic disturbance produced above the epicenter, is visible in both the South and West subpanels of Panel (c) of Figure 10 and 11 and in the West subpanel of Figure 12. Note here that the difference in the TID velocity is easily explained by the fact that the small distance covered by the first shock acoustic wave makes it difficult to reliably and accurately identify such waves. Moreover, the near-field TID shows almost no signature for those stations located North of the epicenter, which was expected due to the adverse geometry of the wave vector and MFLs. The lack of signatures East of the epicenter in Figure 10 and 9 is instead due to the scarcity of GNSS data accessible for those regions and as well due to the adverse observational geometry. A similar reasoning applies to the south panel of Figure 11, where due to the adverse geometry, no clear signatures are visible even if the mutual orientation of the wave vector and MFLs is optimal. The few stations that are available showed clear TID signatures East and West of the epicenter for PRN49 where the mutual orientation of the wave vector and observational link was favorable (See Figure 12). This azimuthal anisotropy is in good agreement with previous studies (Zettergren & Sniveley, 2019), which used models and measurements to explain such behaviors (Bagiya et al., 2019; Rolland et al., 2013). To sum up, the near field TID was defined by a 2-3 minutes period, a maximum amplitude of 1 TECu for stations located in Cyprus, and a propagation speed of ~1.150 km/s. In addition, such wave was detected by PRN 17, 49 and 58, East, South and West of epicenter, with signatures spanning from a few kilometers to almost 1000 km away from the epicenter.

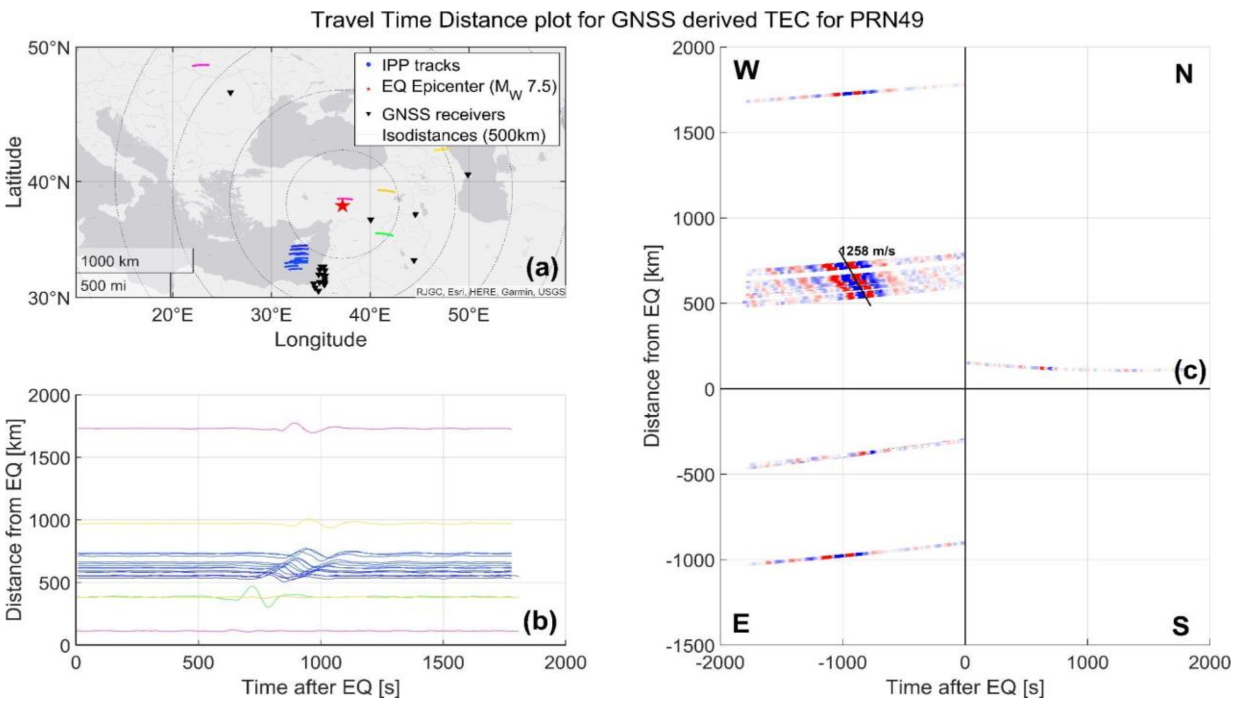

Figure 12. (a) Spatial distribution of IPPs and the epicenter location, (b) Travel-time diagram for the stations shown in (a) and to be completed. (c) Travel-time diagram for different azimuth for PRN49.

The second type of TIDs is the one produced by propagating seismic waves. The West subpanel of Panel (c) in Figure 10 shows a clear signature of such Rayleigh wave-induced TIDs. Specifically, such waves propagated at around 3 km/s, and the first signature was visible around 11 minutes after the earthquake.

Since the expected delay is normally 8 to 9 minutes, we can understand the slightly longer delay due to the fact that the Rayleigh wave had to propagate from the epicenter to the projection on the earth's surface of the first IPP that shows the TID (around 200km, which corresponds to around 1 minute). The period of such Rayleigh-induced TIDs is nearly the same as for the near-field one, thus around 2.5 minutes. Moreover, in the South quadrant of Panel (c) of Figure 10 it seems that two different waves are interacting. Specifically, the first TID signature (the one that shows a speed of 1215 m/s) is interpreted as the co-seismic TID propagating from the epicenter, while for IPPs further than -500 km, it looks as if a faster wave appeared before the near-field one and interacted with it. This pattern could be explained by Rayleigh waves propagating through the ground at speeds around three times higher than the co-seismic TID, which propagates at the speed of sound if the F-layer. Therefore, the Rayleigh wave overcoming the slower near-field TID can explain the mode splitting at around -500 km in the South quadrant. A similar behaviour is also visible in the West quadrant of Figure 11, where two TIDs appeared in the same observation arcs. The first one, with a speed of 3020 m/s, is the Rayleigh wave signature, while the slower one is the co-seismic one. The arcs showing such signatures are all further than 600km, which is consistent with Panel (c) of Figure 10, where the two modes splitting happens around 500 km of distance. This behavior of two modes splitting is typical of earthquake-induced TIDs, and many examples are available in the literature (see e.g., Astafyeva, 2019).

4. Synopsis and conclusions

The networks of different instruments (GNSS receivers, ionosondes, CDSS, seismographs) exploited for this study allowed us to study several aspects of the earthquake-induced various ionospheric disturbances. The first one to appear, was induced by the shock acoustic wave excited by the earth's crust movement close to the epicenter. The near-field TIDs parameters are in accordance with those described by Vesnin et al. (2023), and those seen for other earthquakes that have been studied in the past (Astafyeva, 2019; Kakinami et al., 2013). Moreover, as discussed in the results section, this shock acoustic wave -induced TIDs with a clear anisotropy in the azimuth of propagation, as almost no clear shock acoustic wave related signature is visible for stations located north of the epicenter. This behavior is again in agreement with models (Bagiya et al., 2019; Otsuka et al., 2006; Rolland et al., 2013) and instrumental results (Astafyeva et al., 2009; Kakinami et al., 2013).

The second type of TID detected is the one related to Rayleigh waves. Thanks to the TEC hodocrone, we know that such a wave had a speed of around 3 km/s and a period of around 2,5 minutes, a common value for this type of perturbation. As for the near-field TIDs, the Rayleigh wave shows no clear TID signatures for IPPs North of the epicenter but can instead be traced further though disturbances seen in ionograms. Note that, as the TIDs produced by earthquakes are of medium scale, they are seen as distortions in individual ionograms. As shown in Venin et al. (2023), ionospheric characteristics such as foF2 do not show a clear effect. In earlier literature (Astafyeva et al., 2009; Galvan et al., 2012, Jin et al., 2015), it was possible to trace different TID modes in GNSS derived TEC up to almost 2000 km. However, those works analysed the ionospheric response of more powerful earthquakes, with MW > 8. This can explain why we did not see a clear TEC signature at such long distances. This work illustrates the complementarity of ionosonde and GNSS receiver data, as relatively weak disturbances can still be detected as multi cusp signatures in iongorams at much larger distances.
Another pattern discernible from the GNSS-related figures common for co-seismic TIDs is the two-mode splitting, which happens around 500 and 600 km away from the epicenter for Figure 10 and 11 respectively. This two modes splitting behavior is typical of earthquake-induced TIDs, and many examples are available in the literature (Astafyeva et al., 2009; Kakinami et al., 2013).
Finally, using continuous Doppler sounding systems, it was possible to detect infrasound signatures associated with different types of seismic waves. The infrasound signature associated with the P and S waves is not discernable in the TEC data or even in the ionograms analysed. This further illustrates how the use of multiple instruments is required for observing the entire spectrum of ionospheric disturbances generated by seismic events.

It is worth comparing the ionospheric disturbances described here to those detected after the eruption of the Hunga Tonga volcano in January 2022 (e.g., Chum et al. 2023, Astafyeva et al., 2022; Themens, et al. 2022, Maletckii & Astafyeva, 2022, Verhulst et al., 2022), as the latter was the first such eruption in a long time, and the first for which data quality and coverage was comparable to the earthquake discussed here. After this eruption, TIDs were observed circling the entire globe multiple times. This is not the case for the earthquake analysed here, although TID propagation over longer distances is possible for more powerful earthquakes. However, also the mechanisms for impacting the ionosphere are different between earthquakes and volcanic eruptions. In the case of the volcanic eruption, the most significant mechanism for influencing the ionosphere was the Lamb wave, a feature not present in the context of earthquakes. Thus, although various impulsive events produce signatures in the ionosphere, the nature of their source is important in determining what type of waves will be detected. Conversely, this confirms that the details of the observed ionospheric waves can be used to identify the nature of the earthquake event, as proposed by Sevastano et al. (2017) and Astafyeva (2019).
One aspect of the observations that is clearly similar between events is the anisotropy of the propagation of ionospheric disturbances produced directly over the source. This was also seen after the Hunga eruption, as there was significant anisotropy in the TIDs close to the site of the eruption (Themens et al., 2023). Similar anisotropic propagation was also observed for TIDs from other sources, for instance in the analysis of Luo et al. (2020) concerning a major meteor impact. This therefore must be considered a general feature of TIDs excited by impulsive point sources.

Acknowledgments
Part of this work was funded by: a) T-FORS project by European Commission (number SEP-210818055) and project SAV-23-02 by the Czech Academy of Sciences.
Some of the authors were partially funded through the EU projects PITHIA-NRF (Grant nr. 101007599) and T-FORS (Grant nr. 101081835)
The contribution of VB was supported by the Hungarian National Research, Development and Innovation Office and by Bolyai Fellowship (GD, no. BO/00461/21). The ionograms from the Athens ionosonde were provided by Dr. Anna Belehaki. The authors wish to thank the seismic data to the ORFEUS (European infrastructure for seismic waveform data), furthermore to the European Integrated Data Archive (EIDA) and all the EU projects and institutions that supported them.

The datasets analyzed for this study can be found in the:
The SymH and Kp geomagnetic indices are provided by the World Data Center for Geomagnetism of Kyoto (http:// wdc. kugi. kyoto-u. ac. jp/ index. html), while the PC index by the Arctic and Antarctic Research Institute or Russia and the Technical University of Denmark (PCI, https:// pcind ex. org/). DSCOVR data are available at National Centers for Environmental Information of NOAA (https://www.ngdc.noaa.gov/dscovr/portal/index.html#/). The ionograms analysed can be found in the GIRO (https://giro.uml.edu) and eSWua http://www.eswua.ingv.it/) repositories. The CDSS data can be found in the archive maintained by IAP

http://datacenter.ufa.cas.cz/). Seismic data is available in the European Integrated Data Archive (EIDA) through the following link: https://www.orfeus-eu.org/data/. The GNSS database containing all the RINEX files used for this study can be found at the following link: https://doi.org/10.5281/zenodo.7923587

Conflicts of Interest:

The authors declare no conflict of interest.

References

Afraimovich, E. L., Perevalova, N. P., Plotnikov, A. V., & Uralov, A. M. (2001). *The shock-acoustic waves generated by earthquakes*. Annales Geophysicae, *19*(4), 395–409. https://doi.org/10.5194/angeo-19-395-2001

Afraimovich, E.L., Astafyeva, E.I. & Zhivetiev, I.V. *Solar activity and global electron content*. Dokl. Earth Sc. 409, 921–924 (2006). https://doi.org/10.1134/S1028334X06060195

Astafyeva, E., & Heki, K. (2009). *Dependence of waveform of near-field co-seismic ionospheric disturbances on focal mechanisms*. *LETTER Earth Planets Space* (Vol. 61, pp. 939–943). Retrieved from www.eri.u-tokyo.ac.jp/sanchu/SeismoNote/.

Astafyeva, E., Heki, K., Kiryushkin, V., Afraimovich, E., & Shalimov, S. (2009). Two-mode long-distance propagation of co-seismic ionosphere disturbances. *Journal of Geophysical Research: Space Physics*, *114*(10). https://doi.org/10.1029/2008JA013853

Astafyeva, E., Maletckii, B., Miksell, T. D., Munaibari, E., Ravanelli, M., Coisson, P., Manta, F., and Rolland, L. (2022) *The 15 January 2022 Hunga Tonga Eruption History as Inferred From Ionospheric Observations*, Geophys. Res. Lett. 49(10), e2022GL098827, doi:10.1029/2022GL098827Astafyeva, E. (2019). Ionospheric Detection of Natural Hazards. *Reviews of Geophysics*, *57*(4), 1265–1288. https://doi.org/10.1029/2019RG000668

Astafyeva, EI. and Afraimovich, EL (2019), *Long-distance traveling ionospheric disturbances caused by the great Sumatra-Andaman earthquake on 26 December 2004*, Earth Planets and Space, Vol.58, Issue 8, 1025-1031, DOI10.1186/BF03352607

Artru, J, Farges, T and Lognonne, P. (2004), *Acoustic waves generated from seismic surface waves: propagation properties determined from Doppler sounding observations and normal-mode modelling*. Geophysical Journal International, Vol.158, Issue 3, 1067-1077, DOI10.1111/j.1365-246X.2004.02377.x

Bagiya, M. S., Sunil, A. S., Rolland, L., Nayak, S., Ponraj, M., Thomas, D., & Ramesh, D. S. (2019). *Mapping the Impact of Non-Tectonic Forcing mechanisms on GNSS measured Co-seismic Ionospheric Perturbations.* Scientific Reports, 9(1). https://doi.org/10.1038/s41598-019-54354-0

Bass H, Sutherland ELC, Piercy J, Evans L (1984), *Absorption of sound by the atmosphere*, in Physical Acoustics, Vol. XVII, Chap. 3., edited by W.P. Mason and R.N. Thurston, 145-232, Academic Press, Inc

Chum, J., F. Hruska, J. Zednik, and J. Lastovicka (2012), Ionospheric disturbances (infrasound waves) over the Czech Republic excited by the 2011 Tohoku earthquake, J. Geophys. Res., 117, A08319, doi:10.1029/2012JA017767

Chum, J., F.A.M. Bonomi, J. Fišer, M.A. Cabrera, R.G. Ezquer, D. Burešová, J. Laštovička, J. Baše, F. Hruška, M.G. Molina, J.E.Ise, J.I. Cangemi, and T. Šindelářová (2014), *Propagation of gravity waves and spread F in the low-latitude ionosphere over Tucumán, Argentina, by continuous Doppler sounding: First results*, J. Geophys. Res.Space Physics, 119, 6954–6965, doi:10.1002/2014JA020184.

Chousianitis, K., Papanikolaou, X., Drakatos, G., & Tselentis, G. -Akis. (2021). NOANET: A Continuously Operating GNSS Network for Solid-Earth Sciences in Greece. Seismological Research Letters, 92(3), 2050–2064. https://doi.org/10.1785/0220200340

Chum J., Y.-J. Liu, J. Laštovička, J. Fišer, Z. Mošna, J. Baše, Y.Y. Sun (2016a), Ionospheric signatures of the April 25, 2015 Nepal earthquake and the relative role of compression and advection for Doppler sounding of infrasound in the ionosphere, Earth, Planets, Space, 68:24, DOI 10.1186/s40623-016-0401-9

Chum, J., M. A. Cabrera, Z. Mošna, M. Fagre, J. Baše, and J. Fišer (2016b), Nonlinear acoustic waves in the viscous thermosphere and ionosphere above earthquake, J. Geophys. Res. Space Physics, 121, doi:10.1002/2016JA023450.

Chum, J., J.-Y. Liu, K. Podolská, T. Šindelářová (2018a), Infrasound in the ionosphere from earthquakes and typhoons, J. Atmos. Sol. Terr. Phys., 171, 72-82, doi:/10.1016/j.jastp.2017.07.022

Chum,J., Urbář, J., Laštovička, J., Cabrera, M. A., Liu, J.Y., Bonomi, F., Fagre, M.,Fišer, J. & Mošna, Z. (2018b), Continuous Doppler sounding of the ionosphere during solar flares, Earth, Planets and Space, 2018, 70:198, https://doi.org/10.1186/s40623-018-0976-4

Chum, J., Podolská, K., Rusz, J., Baše, J., Tedoradze, N. (2021), Statistical investigation of gravity wave characteristics in the ionosphere. Earth Planets Space 73, 60, https://doi.org/10.1186/s40623-021-01379-3

Chum J., Šindelářová T., Koucká Knížová P., Podolská K., Rusz J., Baše J., Nakata H., Hosokawa K., Danielides M., Schmidt C., Knez L., Liu J-Y., Molina M.G., Fagre M., Katamzi-Joseph Z., Ohya H., Omori T., Laštovička J., Obrazová Burešová D., Kouba D., Urbář J., Truhlík V. (2023), Atmospheric and ionospheric waves induced by the Hunga eruption on 15 January 2022; Doppler sounding and infrasound, Geophys. J. Int. (2023) 233, 1429–1443, https://doi.org/10.1093/gji/ggac517

Cicone, A., & Zhou, H. (2021). Numerical analysis for iterative filtering with new efficient implementations based on FFT. *Numerische Mathematik*, *147*(1), 1–28. https://doi.org/10.1007/s00211-020-01165-5

Dal Zilio, L., & Ampuero, J. P. (2023). Earthquake doublet in Turkey and Syria. Communications Earth & Environment, 4(1), 71

Danezis, C., Chatzinikos, M., & Kotsakis, C. (2019). LINEAR AND NONLINEAR DEFORMATION EFFECTS IN THE PERMANENT GNSS NETWORK OF CYPRUS (version 2019).

David A. Galvan, Attila Komjathy, Michael P. Hickey, Philip Stephens, Jonathan Snively, Y. Tony Song, Mark D. Butala, and Anthony J. Mannucci (2012): "Ionospheric signatures of Tohoku-Oki tsunami of March 11, 2011: Model comparisons near the epicenter," Radio Sci., 47(4), RS4003, doi:10.1029/2012rs005023

Davies K., Watts J., Zacharisen D. (1962), A study of F2-layer effects as observed with a Doppler technique. J Geophys Res 67:2. doi:10.1029/JZ067i002p00601

Dow, J. M., Neilan, R. E., & Rizos, C. (2009). The International GNSS Service in a changing landscape of Global Navigation Satellite Systems. Journal of Geodesy, 83(3), 191–198. https://doi.org/10.1007/s00190-008-0300-3

Drob, D. P., et al. (2015), An update to the Horizontal Wind Model (HWM): The quiet time thermosphere, Earth Space Sci., 2, 301–319, doi:10.1002/2014EA000089.

Eric Calais and J. Bernard Minster (1995): "GPS detection of ionospheric perturbations following the January 17, 1994, Northridge Earthquake," Geophys. Res. Lett. 22(9), 1045–1048, doi:10.1029/95gl00168.

Ducic, V., Artru, J., & Lognonné, P. (2003). Ionospheric remote sensing of the Denali Earthquake Rayleigh surface waves. *Geophysical Research Letters*, *30*(18). https://doi.org/10.1029/2003GL017812

Georges, T.M., 1973. Infrasound from convective storms: examining the evidence. Rev. Geophys. Space Phys. 11, 571–594.

Galvan, D. A., Komjathy, A., Hickey, M. P., Stephens, P., Snively, J., Song, Y. T., Butala, M. D., and Mannucci, A. J. (2012) *Ionospheric signatures of Tohoku-Oki tsunami of March 11, 2011: Model comparisons near the epicenter*, Radio Sci. 47, RS4003, doi:10.1029/2012rs005023.

Heki, K., & Ping, J. (2005). Directivity and apparent velocity of the co-seismic ionospheric disturbances observed with a dense GPS array. *Earth and Planetary Science Letters*, *236*(3), 845–855. https://doi.org/10.1016/j.epsl.2005.06.010

István Bondár and Dmitry Storchak (2011): Improved location procedures at the International Seismological Centre, Geophys. J. Int. 186(3), 1220–1244, doi:10.1111/j.1365-246X.2011.05107.x.

Jacobs JA, Watanabe T (1966) Doppler frequency changes in radio waves propagating through a moving ionosphere. Radio Science 1(3):257–264

Jin, S., Occhipinti, G., and Jin., R. (2015) GNSS ionospheric seismology: Recent observation evidences and characteristics, Earth-Sci. Rev. 147, 54--64, doi:10.1016/j.earscirev.2015.05.003.

Kakinami, Y., Kamogawa, M., Watanabe, S., Odaka, M., Mogi, T., Liu, J. Y., et al. (2013). Ionospheric ripples excited by superimposed wave fronts associated with Rayleigh waves in the thermosphere. *Journal of Geophysical Research: Space Physics*, *118*(2), 905–911. https://doi.org/10.1002/jgra.50099

Kauristie, K., Morschhauser, A., Olsen, N., Finlay, C. C., McPherron, R. L., Gjerloev, J. W., & Opgenoorth, H. J. (2017). On the usage of geomagnetic indices for data selection in internal field modelling. Space Science Reviews, 206, 61-90.

Kemal Önder Çetin, Makbule Ilgaç, Gizem Can, and Elife Çakır (2023): Preliminary Reconnaissance Report on February 6, 2023, Pazarcık M_W=7.7 and Elbistan M_W=7.6 Kahramanmaraş-Türkiye Earthquakes, Report no: METU/EERC 2023-01, Middle East Technical University – Earthquake Engineering Research Center.

Kenneth Davies and Donald M. Baker (1965): “Ionospheric effects observed around the time of the Alaskan earthquake of March 28, 1964,” J. Geophys. Res. 70(9), 2251–2253, doi:10.1029/jz070i009p02251.

Kikuchi T, Chum J., Tomizawa I, Kumiko K. K K, Hosokawa K, Ebihara Y, Hozumi K, Supnithi P (2021), Penetration of the electric fields of the geomagnetic sudden commencement over the globe as observed with the HF Doppler sounders and magnetometers, Earth, Planets and Space, 73:10, https://doi.org/10.1186/s40623-020-01350-8

Kikuchi T., Araki T., Hashimoto K. K., Ebihara Y., Tanaka T., Nishimura Y., Vichare G., Sinha A. K., Chum J., Hosokawa K., Tomizawa I., Tanaka Y., Kadokura A. (2022), Instantaneous Achievement of the Hall and Pedersen–Cowling Current Circuits in Northern and Southern Hemispheres During the Geomagnetic Sudden Commencement on 12 May 2021, Front. Astron. Space Sci. 9: 879314, https://doi.org/10.3389/fspas.2022.879314

Komjathy, A., Yang, Y. M., Meng, X., Verkhoglyadova, O., Mannucci, A. J., & Langley, R. B. (2016). Review and perspectives: Understanding natural-hazards-generated ionospheric perturbations using GPS measurements and coupled modeling. *Radio Science*, *51*(7), 951–961. https://doi.org/10.1002/2015RS005910

Kosuke Heki (2021): “Ionospheric Disturbances Related to Earthquakes,” in: Chaosong Huang and Gang Lu (eds.) Space Physics and Aeronomy, Volume 3, Ionosphere Dynamics and Applications (chapter 21), John Wiley & Sons, NJ USA, International Seismological Centre (2023), On-line Bulletin, doi:/10.31905/D808B830.

Laštovička, J., and J. Chum (2017) A review of results of the international ionospheric Doppler sounder network, Adv. Space Res., 60, 1629-1643, http://dx.doi.org/10.1016/j.asr.2017.01.032

Leonard R.S. and R.A. Barnes, Jr. (1965): “Observation of ionospheric disturbances following the Alaska earthquake,”. Geophys. Res. 70(5), 1250–1253, doi:10.1029/jz070i005p01250.

Li, H., Wang, C., & Kan, J. R. (2011). Contribution of the partial ring current to the SYMH index during magnetic storms. Journal of Geophysical Research, 116(A11), A11222.

Liu, J.Y. , Y. B. Tsai, S. W. Chen, C. P. Lee, Y. C. Chen, H. Y. Yen, W. Y. Chang, and C. Liu (2006): “Giant ionospheric disturbances excited by the M9.3 Sumatra earthquake of 26 December 2004,” Geophys. Res. Lett. 33(2), L02103, doi:10.1029/2005gl023963

Liu, J.Y., Yang, S.S., Rajesh, P.K., Sun Y.Y., Chum, J., Pan, C.J., Chu, Y.H., Chao, C.K. and Chang L.C. (2019), Ionospheric response to the 21 May 2012 annular solar eclipse over Taiwan, Journal of Geophysical Research: Space Physics, 124, 3623–3636. https://doi.org/10.1029/2018JA025928

Luca Dal Zilio and Jean-Paul Ampuero (2023): “Earthquake doublet in Turkey and Syria,” Commun. Earth Environ. 4, 71, doi:10.1038/s43247-023-00747

Lucie M. Rolland, Philippe Lognonné, and Hiroshi Munekane (2011): “Detection and modeling of Rayleigh wave induced patterns in the ionosphere,” J. Geophys. Res., 11, A05320, doi:10.1029/2010AJ016060.

Madonia, P., Bonaccorso, A., Bonforte, A., Buonocunto, C., Cannata, A., Carleo, L., et al. (2023). Propagation of Perturbations in the Lower and Upper Atmosphere over the Central Mediterranean, Driven by the 15 January 2022 Hunga Tonga-Hunga Ha’apai Volcano Explosion. *Atmosphere*, *14*(1), 65. https://doi.org/10.3390/atmos14010065

Michelini, A., Margheriti, L., Cattaneo, M., Cecere, G., D'Anna, G., Delladio, A., et al. (2016). The Italian National Seismic Network and the earthquake and tsunami monitoring and surveillance systems. Advances in Geosciences, 43, 31–38. https://doi.org/10.5194/adgeo-43-31-2016

NOAA Space Weather Prediction Center (2016): Deep Space Climate Observatory (DSCOVR). NOAA National Centers for Environmental Information. Dataset. http://doi.org/10.7289/V51Z42F7

Maletckii, B. and Astafyeva, E. (2022) *Near-Real-Time Analysis of the Ionospheric Response to the 15 January 2022 Hunga Tonga-Hunga Ha'apai Volcanic Eruption*, J. Geophys. Res. 127(10), e2022JA030735, doi:10.1029/2022JA030735.

Mannucci, A. J., Wilson, B. D., Yuan, D. N., Ho, C. H., Lindqwister, U. J., & Runge, T. F. (1998). A global mapping technique for GPS-derived ionospheric total electron content measurements. *Radio Science*, *33*(3), 565–582. https://doi.org/10.1029/97RS02707

Maruyama, T., Tsugawa, T., Kato, H., Saito, A., Otsuka, Y., and Nishioka, M.: Ionospheric multiple stratifications and irregularities induced by the 2011 off the Pacific coast of Tohoku Earthquake, Earth Planets Space, 63, 65, https://doi.org/10.5047/eps.2011.06.008, (2011)

Maruyama, T., T. Tsugawa, H. Kato, M. Ishii, and M. Nishioka, Rayleigh wave signature in ionograms induced by strong earthquakes, J. Geophys. Res., 117, A08306, doi:10.1029/2012JA017952, (2012)

Maruyama, T., and H. Shinagawa, Infrasonic sounds excited by seismic waves of the 2011 Tohoku-oki earthquake as visualized in ionograms, J. Geophys. Res. Space Physics, 119, 4094–4108, doi:10.1002/2013JA019707, (2014)

Nava, B., Coisson, P., & Radicella, S. M. (2008). A new version of the NeQuick ionosphere electron density model. *Journal of Atmospheric and Solar-Terrestrial Physics*, *70*(15), 1856–1862. https://doi.org/10.1016/j.jastp.2008.01.015

Otsuka, Y., Kotake, N., Tsugawa, T., Shiokawa, K., Ogawa, T., Saito, S., et al. (2006). *GPS detection of total electron content variations over Indonesia and Thailand following the 26 December 2004 earthquake*. *Earth Planets Space* (Vol. 58, pp. 159–165).

Ouml, & Yildirim, M. (2011). A comparative analysis of the virtual reference stations (VRS). Scientific Research and Essays, 6(27), 5726–5733. https://doi.org/10.5897/SRE11.786

Perevalova, V, V.A. Sankov, E.I. Astafyeva, and A.S. Zhupityaeva (2014): “Treshold magnitude for ionospheric TEC response to earthquakes,” J. Atmos. Sol. Terr. Phys. 108, 77–90, doi:10.1016/j.jastp.2013.12.014.

Philippe Lognonné, Juliette Artru, Raphael Garcia, François Crespon, Vesna Ducic, Eric Jeansou, Giovani Occhipinti, Jérôme Helbert, Guilhelm Moreaux, and Pierre-Emmanuel Godet (2006): “Ground-based GPS imaging of ionospheric post-seismic signal,” Planet. Space Sci. 54(5), 528–540, doi:10.1016/j.pss.2005.10.021.

Rolland, L., Lognonné, P., Munekane, H. M., Rolland, L. M., & Munekane, H. (2011). Detection and modeling of Rayleigh wave induced patterns in the ionosphere. *Journal of Geophysical Research Space Physics*, *116*(A5), 5320. https://doi.org/10.1029/2010JA016060ï

Rolland, L. M., Vergnolle, M., Nocquet, J. M., Sladen, A., Dessa, J. X., Tavakoli, F., et al. (2013). Discriminating the tectonic and non-tectonic contributions in the ionospheric signature of the 2011, Mw7.1, dip-slip Van earthquake, Eastern Turkey. *Geophysical Research Letters*, *40*(11), 2518–2522. https://doi.org/10.1002/grl.50544

Sevastano, G., Komjathy, A., Verkhoglyandova, O. Mazzoni, A., Crespi, M., Wei, Y. et al. (2017) Real-Time Detection of Tsunami Ionospheric Disturbances with a Stand-Alone GNSS Receiver: A Preliminary Feasibility Demonstration, Sci. Rep. 7, 46607, doi:10.1038/srep46607.

Sindelarova T., Mosna Z., Chum J., Kouba D., Base J., Liu J.Y., and Katamzi-Joseph Z. (2018), Solar eclipse effects in the ionosphere observed by continuous Doppler sounding, Adv. Space Res., 62, 785-800, http://dx.doi.org/10.1016/j.asr.2018.05.029

Stauning P (2013) The polar cap index: a critical review of methods and a new approach. J Geophys Res Space Phys 118(8):5021–5038

Strollo, A., Cambaz, D., Clinton, J., Danecek, P., Evangelidis, C. P., Marmureanu, A., & Triantafyllis, N. (2021). EIDA: The European integrated data archive and service infrastructure within ORFEUS. Seismological Society of America, 92(3), 1788-1795.

Takashi Maruyama, Kamil Yusupov, and Adel Akchurin (2016a): “Interpretation of deformed ionograms induced by vertical ground motion of seismic Rayleigh waves and infrasound in the thermosphere” Ann. Geophys. 34(2), 271–278, doi:10.5194/angeo-34-271-2016.

Takashi Maruyama, Kamil Yusupov, Adel Akchurin (2016b): “Ionosonde tracking of infrasound wavefronts in the thermosphere launched by seismic waves after the 2010 M8.8 Chile earthquake,” J. Geophys. Res. 121(3), 2683–2692, doi:10.1002/2015ja022260.

Torres, J. A., Altamimi, Z., Boucher, C., Brockmann, E., Bruyninx, C., Caporali, A., et al. (2009). Status of the European Reference Frame (EUREF). In M. G. Sideris (Ed.), Observing our Changing Earth (pp. 47–56). Berlin, Heidelberg: Springer. https://doi.org/10.1007/978-3-540-85426-5_6

Themens, D. R., Watson, C., Žagar, N., Vasylkevych, S., Elvidge, S., McCaffrey, A., Prikryl, P., Reid, B., Wood, A., and Jayachandran, P. T. (2022) Global Propagation of Ionospheric Disturbances Associated With the 2022 Tonga Volcanic Eruption, Geophys. Res. Lett. 49(7), e2022GL098158, doi:10.1029/2022GL098158.

US Geological Survey (2023): Event page of the M7.8 - Pazarcik earthquake, Kahramanmaras earthquake sequence, https://earthquake.usgs.gov/earthquakes/eventpage/us6000jllz/executive.

Vanlommel, P. (2018). Solar-Terrestrial Centre of Excellence (STCE) Newsletter, issue 17 Feb 2023. Available online at https://www.stce.be/newsletter/.

Verhulst, T. G. W., Altadill, D., Barta, V., Belehaki, A., Burešová, D., Cesaroni, C., et al. (2022). Multi-instrument detection in Europe of ionospheric disturbances caused by the 15 January 2022 eruption of the Hunga volcano. *Journal of Space Weather and Space Climate*, *12*, 35. https://doi.org/10.1051/swsc/2022032

Vesnin A, Yasyukevich Y, Perevalova N, Şentürk E. Ionospheric Response to the 6 February 2023 Turkey–Syria Earthquake. Remote Sensing. 2023; 15(9):2336. https://doi.org/10.3390/rs15092336

Watada S, Kunugi T, Hirata K, Sugioka H, Nishida K, Sekiguchi S, Oikawa J, Tsuji Y, Kanamori H (2006) Atmospheric pressure chase associated with the 2003 Tokachi-Oki earthquake. Geophys Res Lett 33, L24306. doi:10.1029/2006GL027967

Xing Meng, Panagiotis Vergados, Attila Komjathy, and Olga Verkhoglyadova (2019): “Upper Atmospheric Responses to Surface Disturbances: An Observational Perspective,” Radio Sci. 54(11), 1076–1098, doi:10.1029/2019rs006858.

Zettergren M.D. and J.B. Snively (2019): “Latitude and Longitude Dependence of Ionospheric TEC and Magnetic Perturbations From Infrasonic-Acoustic Waves Generated by Strong Seismic Events,” Geophys. Res. Lett. 46, 1132–1140, doi:10.1029/2018GL081569.

Multi-instrument observations of various ionospheric disturbances caused by the 6 February 2023 Turkey earthquake

Haris Haralambous[1], Marco Guerra[2,3], Jaroslav Chum[4], Tobias G. W. Verhulst[5], Veronika Barta[6], David Altadill[7], Claudio Cesaroni[2], Ivan Galkin [8], Kiszely Márta[9], Jens Mielich[10], Daniel Kouba[4], Dalia Buresova[4], Antoni Segarra[7], Luca Spogli[2,11], Jan Rusz [4], Jan Zedník[12]

[1] Frederick University, School of Engineering, Nicosia, Cyprus
[2] Istituto Nazionale di Geofisica e Vulcanologia, Rome, Italy
[3] Sapienza Università di Roma, Rome, Italy
[4] Institute of Atmospheric Physics, Czech Academy of Sciences, Prague, Czech Republic
[5] Royal Meteorological institute of Belgium & Solar Terrestrial Centre of Excellence, Brussels, Belgium
[6] Institute of Earth Physics and Space Science, Sopron, Hungary
[7] Observatori de l'Ebre, Univ. Ramon Llull – CSIC, 43520 Roquetes, Spain
[8] University of Massachusetts Lowell, Space Science Laboratory, Lowell, United States of America
[9] Kövesligethy Radó Seismological Observatory, Institute of Earth Physics and Space Science, Budapest, Hungary
[10] Leibniz-Institute of Atmospheric Physics, Kuehlungsborn, Germany
[11] SpaceEarth Technology, Rome, Italy
[12] Institute of Geophysics Czech Academy of Sciences, Prague, Czech Republic

***** Correspondence: **eng.hh@frederick.ac.cy**

Abstract: In this work, we investigate various types of ionospheric disturbances observed over Europe after the earthquake in Turkey on 6 February 2023.By combining observations from Doppler sounding systems, ionosondes, and GNSS receivers, we are able to discern different types of disturbances, propagating with different velocities and through different mechanisms. We can detect the co-seismic disturbances produced in the ionosphere close to the epicenter, as well the ionospheric signatures of acoustic waves propagating as a consequence of propagating seismic waves.

Keywords: Earthquake; Total Electron Content; TID; infrasound; ionosonde; CDSS

1. Introduction

On 6 February 2023, two earthquakes with magnitude $M_W > 7$ occurred in Turkey. The first shock was recorded at 01:17 UT with a magnitude of 7.8, while the second shock at 10:24 UT with $M_W = 7.7$ (Çetin et al., 2023; Dal Zilio & Ampuero, 2023; US Geological Survey, 2023). These primary shocks were followed by many aftershocks with magnitude lower than 7. Both major earthquakes happened in the region of the East Anatolian Fault, with the epicenters separated by about 95 km. The first event was located at 37.20°N, 37.13°E, and the second at 38.05°N, 37.25°E; both events took place at a depth of around 10 km (International Seismological Centre, 2023; Bondár & Storchak, 2011).

The work of Leonard & Barnes (1965) and Davies & Baker (1965) concerning the great Alaskan earthquake of 1964, has already demonstrated that major earthquakes can cause disturbances in the ionosphere. Since then, it has been established that these ionospheric disturbances are manifested as different types of earthquake induced travelling ionospheric disturbances (TIDs), propagating through different mechanisms (Astafyeva, 2019; Meng et al., 2019).

Co-seismic ionospheric disturbances are generated by waves travelling vertically up to the upper atmosphere in the vicinity of the epicenter (Afraimovich et al., 2001, Astafyeva & Afraimovich, 2006, 2019). As shown by Rolland et al., (2013) through model results, these vertically propagating acoustic waves are accelerated and deflected horizontally due to the variation of atmospheric parameters with altitude. As a result, such acoustic waves are detected as fast TIDs propagating radially outward from the epicenter. Co-seismic disturbances start travelling out from their origin at around 1000 m/s, the speed of sound at the height of the F layer, but have been observed to split at some distance from the epicenter into different modes travelling with velocities of about 600 and 3000 m/s (Astafyeva et al., 2009, Galvan et al., 2012).

On the other hand, seismic waves propagating out from the epicenter—in particular Rayleigh surface waves—can also generate acoustic-gravity waves propagating up to the ionosphere (Astafyeva et al., 2009, Rolland et al., 2011, Komjathi et al., 2016). These disturbances are expected to propagate at the speed of the Rayleigh waves, between 2000 and 5000 m/s, but with a delay of around ten minutes required for the vertical propagation of disturbances from the ground to ionospheric altitude (Lognonné et al., 2006; Astafyeva, 2019). Since seismic waves on the ground can reach long distances, this mechanism can produce disturbances in the ionosphere beyond the range where the shock-acoustic waves travelling through the ionosphere are attenuated (e.g., Maruyama et al., 2016a; 2016b)

Finally, there are acoustic-gravity waves travelling much slower, with velocities in the order of a few hundred meters per second (Astafyeva et al., 2009, Meng et al., 2019). Besides the various types of travelling disturbances, evidence of longer lasting impacts on the ionosphere, particularly close to the epicenter (Astafyeva, 2019, and references therein) has been reported. However, such effects are not considered here.

Earthquakes with $M_W > 6.5$ are expected to generate co-seismic disturbances in the ionosphere (Perevalova et al., 2014). The amplitude of ionospheric disturbances and the distance from the source at which they can be detected are of course dependent on the magnitude of the event, see for instance Heki (2021). In addition to the earthquake magnitude, the depth and the focal mechanism (Astafyeva & Heki, 2009) are also decisive factors that affect the excitation and propagation of TIDs. On top of these primary earthquake attributes, additional factors such as atmospheric conditions (Rolland et al., 2011) and the orientation of the geomagnetic field (Astafyeva & Heki, 2009; Zettergren & Snively, 2019) also define the characteristics of possible ionospheric disturbances based on the coupling between the movement of the ground surface and the upper atmosphere.

Thus, a complex view of a superposition of different types of travelling ionospheric disturbances is observed after an earthquake, which differs significantly from one event to another. Besides different modes of TIDs, also ionospheric signatures of infrasound can be observed in the aftermath of major earthquakes (Chum et al., 2012; 2018a; Laštovička & Chum, 2017).

Ionospheric disturbances, including those resulting from an earthquake, can be detected using Doppler sounders (Liu et al., 2006; Chum et al., 2012), ionosondes (e.g., Maruyama, 2016a), or GNSS receivers that can facilitate TEC estimation (Calais & Minster, 1995; Afraimovich et al., 2001). This complementary view from observations from different instruments, is ideal for detecting different disturbance types (Astafyeva, 2019; Meng et al., 2019). In the European region, all these instruments are available in relatively dense observational networks (see Figure 1). Disturbances can be observed from a close proximity to the epicenter to distances over 3000 km, and therefore velocities can be calculated. The aim of this paper is to present an integrated picture of the various modes of TIDs generated during this event, as observed by different monitoring networks.

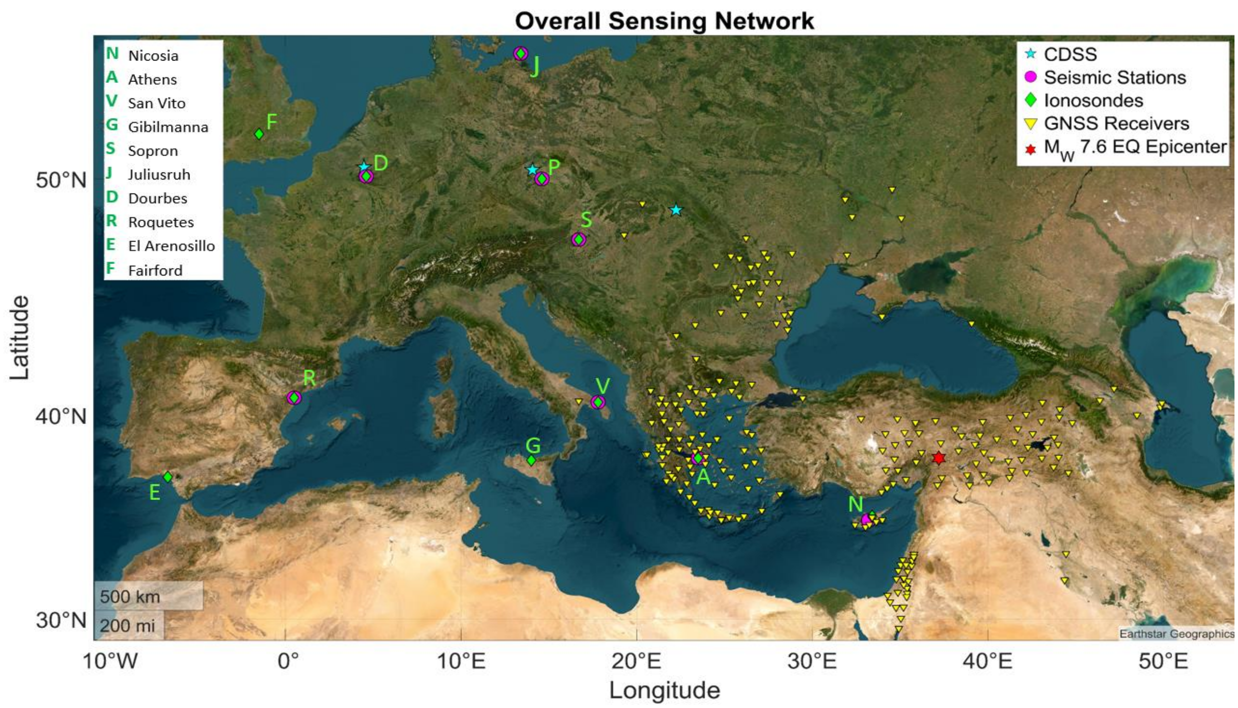

Figure 1. Map showing locations of instruments used for this study. The earthquake epicenter is also shown (red asterisk).

2. Data and Methods

2.1 Geomagnetic conditions

The Turkey earthquakes took place during the ascending phase of the 25th solar cycle.

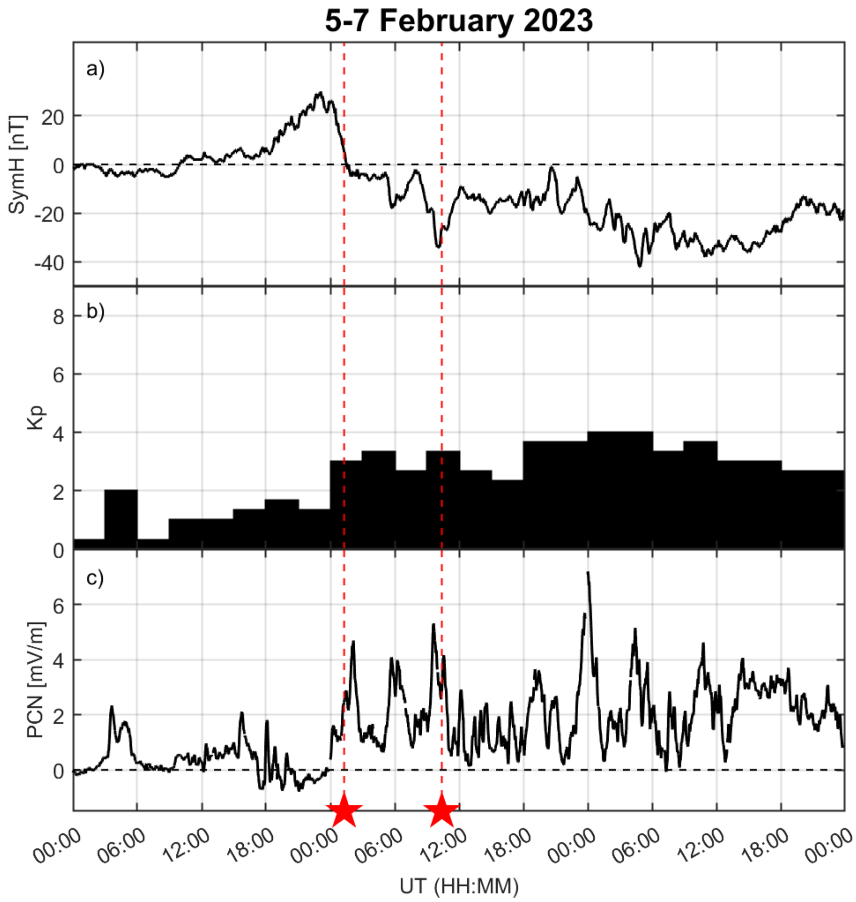

Figure 2. SymH (panel a), Kp (panel b) and Polar Cap North Index (panel c), in the period 5-7 February 2023. The red dashed lines and the corresponding stars indicate the time of the two main shocks (01:17 and 10:24 UT on 6 February 2023).

To quantify geomagnetic disturbances measured on the ground, the SymH (Li et al., 2011), Kp (Kaurisiti et al., 2017) and Polar Cap North (PCN) index (Stauning, 2013) have been considered. Figure 2 shows the time series of the respective indices in the period 5-7 February 2023, also indicating the time of the two main shocks (01:17 and 10:24 UT on 6 February 2023) in red. From the late evening of February 5, the solar wind speed increased, revealing the occurrence of a high speed stream (HSS) linked to a coronal hole in the northern solar hemisphere (Vanlommel, 2018). The solar wind speed slowly increased during 6 February and reached a speed of 600 km/s on 7 February. In correspondence with the passage of such a HSS and under favorable conditions of the Interplanetary Magnetic Field, geomagnetic disturbances covering the period under consideration are found. As reported in Figure 2a-c, these disturbance maximize in the early hours of 7 February (SymH= -42 nT, Kp=4, PCN=8.3). These solar driven disturbances manifested in the ionosphere as spread-F, visible during the nighttime in the higher latitude ionospheric observatories. In addition, the first main shock took place during a local winter night, when background ionization is low. Conversely, during the daytime a positive storm was observed with somewhat enhanced TEC values (Vanlomel, 2018). As a result of these conditions, no clear indication of ionospheric disturbances were detected over Europe after the first shock 01:17 UT, and the rest of this paper focuses on the second main shock at 10:24 UT.

2.2 Seismic context

The different types of seismic waves (body waves: primary P and secondary S, surface waves: Rayleigh waves LR and Love waves LQ) generated by the main shocks were identified at many seismic stations, some of which are located close to an ionosonde station (Figure 1). Figure 3 shows the appearance of seismic waves at various seismic stations co-located with an ionosonde station after the Mw 7.7 earthquake (T0 = 10:24:52 UT). The velocity of the seismic surface waves can be calculated based on the arrival times of the waves and the ground distance of the seismic stations from the epicenter (Table 1). The seismic data is available in the European Integrated Data Archive (EIDA, Strollo et al. 2021). The amplitude of seismic waves registered at Nicosia (ATHA station) were so strong that they caused saturation of the instrument. Determination of Rayleigh wave packets at stations closer to the epicenter is not easy in the case of such a large earthquake. Two types of surface waves (Love and Rayleigh waves) arrive with a minor delay with respect to the S phase. Furthermore, local effects can modify the shape of the waves. We considered the propagation speed of the LR waves to identify the correct Rayleigh arrival time to the different stations during the manual selection.

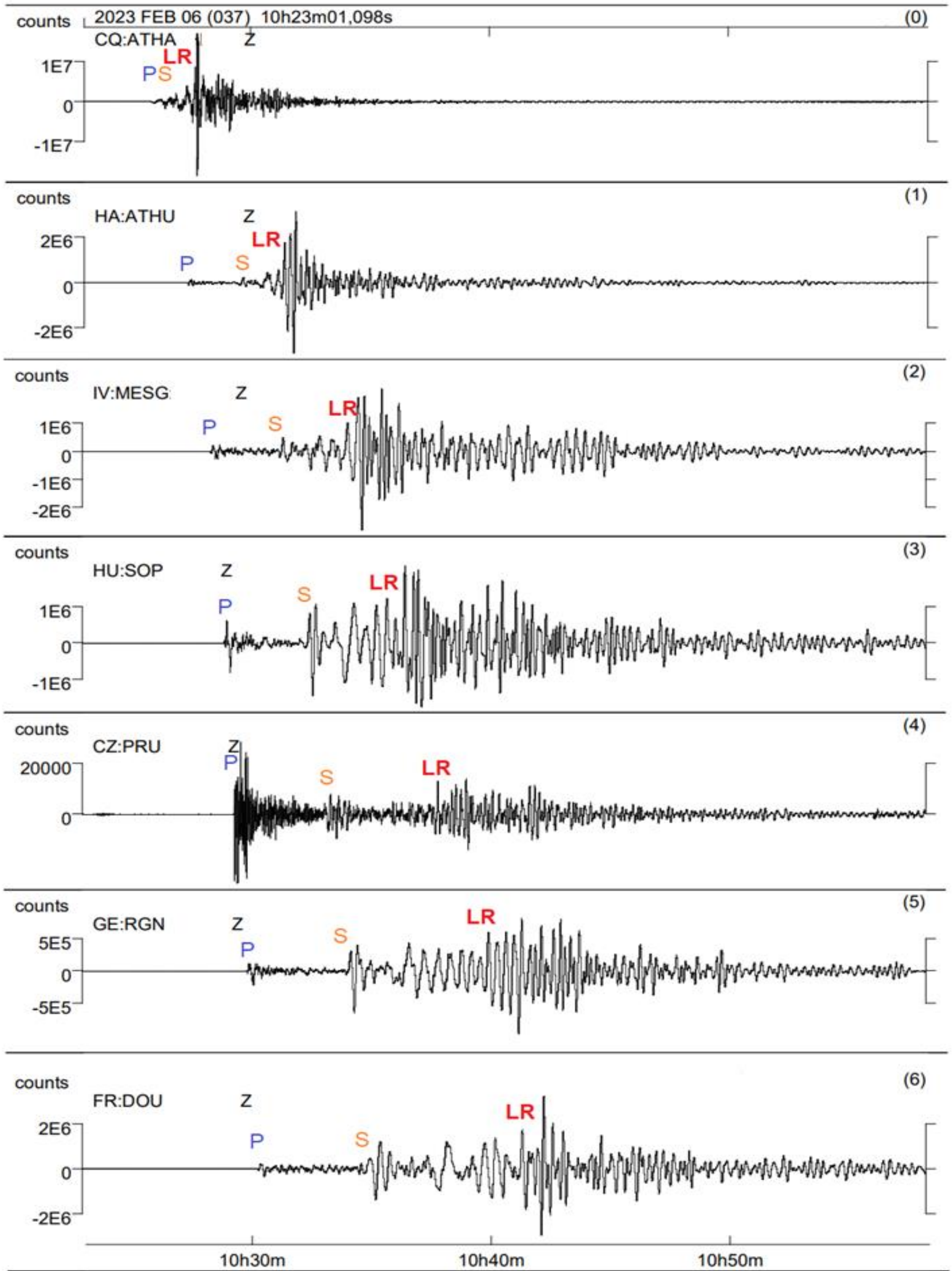

Figure 3. Vertical seismic wave component (Z) recorded at different seismic stations (close to an ionosonde station in Europe) as generated by the earthquake at 10:24 (UT), in order of increasing distance from the epicenter. "Counts" in the y-axis is the raw number read off the physical instrument, ie. the voltage read from a sensor. For example, a "count" value of 3.27508E9 would indicate ground motion of 1 m/s — you can divide the count value by 3.27508E9 to convert into meters per second. However, this multiplier varies from station to station. P, S and Rayleigh wave (LR) indicate the corresponding wave type in the subplots.

Name	Code	Geographic Latitude [°N]	Geographic Longitude [°E]	Distance [km]	Arrival times [UT]		
					P waves	S waves	Rayleigh wave
Athalassa, Cyprus	ATHA	35.1	33.4	460	10:25:52	10:27:07	-
Athens, Greece	ATHU	37.9	23.8	1199	10:27:22	10:29:23	-
Mesagne, Italy	MESG	40.6	17.8	1691	10:28:25	10:31:17	10:32:02
Sopron, Hungary	SOP	47.7	16.6	1975	10:29:02	10:32:17	10:32:40
Průhonice, Czech R.	PRU	50.0	14.5	2232	10:29:25	10:33:09	10:34:17
Ruegen, Germany	RGN	54.5	13.3	2574	10:29:56	10:34:07	10:36:31
Dourbes, Belgium	DOU	50.1	4.6	2900	10:30:25	10:34:53	10:37:23

Table 1. List of seismic stations, which are situated close to a European ionosonde station, in order of increasing distance from the epicenter: name, code and attributes (latitude, longitude, and distance from epicenter in km) of the stations, and the arrival time of different waves at the stations.

2.3 Continuous Doppler Sounding Systems

The European network of Continuous Doppler Sounding Systems (CDSS) currently consists of the multi-point and multi-frequency system operating in the Czech Republic at frequencies of 3.59, 4.65 and 7.04 MHz (Laštovička and Chum, 2017; Chum et al., 2021) and systems recently installed (at the end of 2022) in Belgium and Slovakia operating at frequencies of 4,59 and 3.59 MHz, respectively. Data from the Belgian transmitter in Dourbes (50.099°N, 4.591°E) received in Uccle (50.798°N, 4.358°E), the Czech transmitter located in Dlouha Louka (50.648°N, 13.656°E) received in Prague (50.041°N, 14.476°E), and the Slovak transmitter in Zahor (48.625°N, 22.205°E) received in Kolonica (48.935°N, 22.274°E), shown in Figure 1, were analysed in this paper. It should be noted that half distances between the transmitters and corresponding receivers are several times smaller than the reflection heights, so the zenith angle α of sounding radio waves is small and therefore $\cos(\alpha)\approx 1$. The surface horizontal distances of midpoints between the listed transmitter – receiver pairs in Belgium, the Czech Republic and Slovakia from the epicenter of the Turkey earthquake are about 2920, 2280 and 1700 km, respectively.

CDSS measure the Doppler shift that radio waves are subjected to, when reflected from the ionosphere due to the plasma motion and changes in electron density (Davies et al., 1962; Jacobs and Watanabe, 1966). CDSS have a relatively high time resolution (several seconds) due to the continuous sounding of harmonic radio waves of a specific frequency, but they do not provide any information about the reflection height, the region which contributes most to the observed Doppler shift (Chum et al., 2016a, 2018b). Therefore, it is useful to operate CDSS in the vicinity of an ionospheric sounder that can provide information on the CDSS sounding frequency reflection height, which is essential for a variety of studies (Chum et al., 2012; Chum et al., 2021). CDSS mainly detect medium scale travelling ionospheric disturbances (TID) or spread F (Chum et al., 2014; Chum et al., 2021), but they can also be used for the analysis of electric field that penetrates the ionosphere during geomagnetic storms (Kikuchi et al., 2021, 2022), infrasound generated by earthquakes (Artru et al., 2004; Chum et al., 2012, 2016a,b), typhoons and severe tropospheric weather (Georges, 1973; Chum et al., 2018a) or volcano eruptions

(Chum et al., 2023), ionospheric response to solar eclipses (Sindelarova et al., 2018; Liu et al., 2019), solar flares (Chum et al., 2018b) etc.

It was shown by Watada et al. (2006) that the near surface pressure fluctuations and air particle oscillation velocities w_0 are determined by the vertical component of the velocity of Earth surface motion, v_z. A high correlation between the waveforms of v_z for P and S seismic waves and air particle oscillation velocities w in the ionosphere determined from Doppler shift f_D were shown in (Chum et al., 2012). The similarity of spectral content of v_z and w (f_D) at large distances from the earthquake epicenter was discussed in (Chum et al., 2016a, 2018a). The co-seismic infrasound registered by CDSS during the earthquake under consideration was compared with ground surface vertical velocities v_z measured by seismometers and observed time delays between v_z and w (f_D) were compared numerical simulation using ray tracing code described in previous works (e.g., Chum et al., 2023). In addition, the values of w obtained from measured Doppler shifts were compared with the amplitudes of w expected for infrasound propagating up to the CDSS reflection heights assuming a linear theory of propagation and attenuation due to the viscosity, thermal conductivity and rotational relaxation (Bass et al., 1984; Chum et al., 2012). The air particle oscillation velocity w was estimated from the Doppler shift f_D using the approximate formula (1) derived in (Chum et al., 2016a) for (quasi)vertical sounding and (quasi)vertically propagating infrasound.

$$w = -f_D \cdot \frac{c}{2 f_0 sin^2(I)} \cdot \frac{\frac{\partial N}{\partial z}}{\sqrt{(\frac{\partial N}{\partial z})^2 + (N\frac{2\pi f_{IS}}{c_S})^2}}, \qquad (1)$$

where c is the speed of light, f_0 is the sounding frequency, I is the inclination of geomagnetic field, N is the electron density at the reflection height, $\partial N/\partial z$ is the vertical gradient of electron density at the reflection height estimated from the ionogram, f_{IS} is the infrasound frequency and c_s is the sound speed. The term $N\cdot(2\pi f_{IS})/c_s$ results from the air and plasma compression due to the infrasound waves. If $\partial N/\partial z >> N\cdot(2\pi f_{IS})/c_s$, equation (1) reduces to (2)

$$w = -f_D \cdot \frac{c}{2 f_0 sin^2(I)} \qquad (2)$$

which is a relation that directly follows from the vertical plasma velocity w_p, computed from the Doppler shift f_D by standard equation (3)

$$w_p = -f_D \cdot \frac{c}{2 f_0}, \qquad (3)$$

assuming that (quasi)vertically propagating radio waves reflect from the magnetized plasma, where electrons freely move only along magnetic field lines and are forced by vertically oscillating air.

2.4 Ionograms

An ionospheric earthquake-related signature established as a deformation on ionograms is the multiple-cusp signature ("MCS") which appears as additional cusps that can be attributed to electron density irregularities giving rise to stationary points of inflection in the vertical electron density profile as discussed by Maruyama, et al. (2011, 2012, 2014). This ionogram signature is shown in Figures 7 and 8 for several ionospheric stations and may be interpreted as an indication of the propagation of an acoustic wave as the separation of these points of inflection reflects the infrasound wavelength in the thermosphere. For this particular event all ionosondes considered were situated towards north-west with respect to the epicenter with the exception of the nearest ionosonde to the epicenter located at Nicosia which is positioned south-west with respect to the epicenter. All eleven ionosondes across Europe considered in this study along with their respective ionogram cadence are tabulated in Table 2 in accordance to their distance from the epicenter. Their location is also shown in Figure 1.

Station	URSI Code	Geographic latitude	Geographic longitude	Ionogram Cadence (Min)	Distance From Epicenter (km)
Nicosia	NI135	35.2°N	33.4°E	5.0	460
Athens	AT138	38.0°N	23.5°E	5.0	1199
San Vito	VT139	40.6°N	17.8°E	7.5	1691
Gibilmanna	GM037	37.9°N	14.0°E	15.0	2029
Sopron	SO148	47.6°N	16.7°E	5.0	1975
Průhonice	PQO52	50.0°N	14.6°E	15.0	2232
Juliusruh	JR055	54.6°N	13.4°E	5.0	2574
Dourbes	DB049	50.1°N	4.6°E	5.0	2900
Roquetes	EB040	40.8°N	0.5°E	5.0	3146
Fairford	FF051	51.7°N	-1.5°E	7.5	3358
El Arenosillo	EA036	37.1°N	-6.7°E	5.0	3835

Table 2. European ionosondes used in the study, arranged according to distance from the earthquake epicenter.

2.5 GNSS derived TEC

To investigate the ionospheric signatures in Total Electron Content (TEC) we used a collection of GNSS networks spanning different distances and azimuthal directions with respect to the epicenter (shown as yellow inverted triangles in Figure 1). Data from 1s and 30s RINEX files were used, with 1s as the preferred time resolution due to the relatively short period expected from co-seismic TID (Astafyeva, 2019). The GNSS stations used belong to many different institutions and networks, specifically INGV (Michelini et al., 2016), TUGASA-Aktif (Ouml et al., 2011), CYPOS (Danezis et al., 2019), NOA (Chousianitis et al., 2021), IGS (Dow et al., 2009), and EUREF (Torres et al., 2009). To extract TEC perturbations, we used the dual frequency geometry-free linear combination of carrier-phase measurements. The TEC along the satellite-receiver line of sight can be calculated starting from phase measurements as follows:

$$sTEC_{phase} = \frac{1}{40.308} \frac{{f_1}^2 {f_2}^2}{{f_1}^2 - {f_2}^2} (L_1\lambda_1 - L_2\lambda_2) \quad (4)$$

Where $sTEC_{phase}$ is the ambiguous slant TEC; L_1, L_2 are the phase measurements of the radio signal for the L_1 and L_2 bands defined by their frequency f_1, f_2 and wavelength λ_1, λ_2. By doing so, we obtain an uncalibrated version of sTEC, which is strongly related to the observational elevation. Normally, sTEC is vertically mapped to better compare TEC time-series for different stations and satellites. However, filtering and detrending such an uncalibrated observable would prevent the estimation of the wave amplitude since the calibration bias would be multiplied by the mapping function, causing an amplification of the wave amplitude, especially for low-elevation angles (Verhulst et al., 2022). To prevent or somewhat limit such amplification effect, we employed NeQuick 2 (Nava et al., 2008), a climatological model that provides a TEC estimate between two given points (in our scenario, the initial GNSS station and satellite position). Using this model, we can assign an initial sTEC value between the corresponding GNSS receiver and satellite, which limits by the "verticalization" process. To investigate the spatial behavior of the co-seismic TID, we rely on the widely-used thin-layer ionospheric approximation (Mannucci et al., 1998), with the shell height set to 250 km. To extract the TID signature from the vTEC, we use a bandpass filter based on the novel Fast Iterative Filtering technique (Cicone & Zhou, 2021). This technique can decompose non-stationary, non-linear signals into simple oscillatory components (Madonia et al., 2023; Verhulst et al., 2022) called Intrinsic mode functions, each defined by its quasi-stationary frequency. By summing those modes that fall into the frequency band of interest for each time step, we extracted the detrended TEC (dTEC).

3. Observations and Discussion

3.1 CDSS

Figure 4 shows the Doppler shift spectrograms recorded by CDSS in Slovakia, the Czech Republic and Belgium after the M=7.7 Turkey earthquake on 6 February 2023. All four spectrograms show disturbances caused by infrasound waves. The Doppler shift fluctuations are not very clear in Slovakia, which prevents further analysis. However, Doppler shift time series could be obtained from maxima of spectral densities in the Doppler shift spectrograms recorded in the Czech Republic and Belgium and were used for further analysis.

Figure 5 displays the vertical component of the ground surface velocity v_z measured in Panská Ves, Czech Republic (plot a) and vertical plasma velocity w_p and air particle oscillation velocity w derived from the Doppler shift time series obtained from CDSS operating at f=4.65 MHz and 7.04 MHz (plots b and c, respectively). The fluctuations of w_p (w) in the Czech Republic derived from the 4.65 MHz signal are shorter than those derived from 7.04 MHz signal due to the low quality Doppler shift spectrogram after ~10:47 UT (Figure 4.b). The long-term variations, seen mainly in plots c in Figures 4 and 5 are caused by TIDs not related to the earthquake. On the other hand, the fast variations are due to the infrasound with a period about 20 s and clearly correspond to the variations of v_z shown in Figure 5.a. In particular, the similarity between v_z and

w_p *(w)* for the first pulse (around 10:29:40 UT in v_z), which correspond to P seismic waves is remarkable. The corresponding signatures in the ionosphere recorded by the CDSS are delayed about 485 s for the 4.65 MHz sounding and about 515 s for the 7.04 MHz sounding. A clear similarity between v_z and w_p *(w)* is also observed for the second pulse (around 10:33:32 UT in v_z) corresponding to S seismic waves. The S waves are then followed by Rayleigh waves of higher amplitude and by their corresponding ionospheric signatures. The bottom plots (d) and (e) show ground velocity v_z and the corresponding plasma velocities w_p and air particle oscillation velocities w estimated from CDSS observation in Belgium.

Figure 6 shows the ray tracing simulation results for acoustic waves with a period of 20 s for a realistic atmosphere over the Czech Republic including the neutral horizontal winds obtained by HWM14 model (Drob et al., 2015) on 6 February 2023 at 10:45 UT. The ray tracing was initialized with zenith angles from 2° (red) to 6° (blue). This range covers the expected initial zenith angles α_0, given by the ratio c_{S0}/c_G, $\sin \alpha_0 = c_{S0}/c_G$, where c_{S0} is the near surface sound speed and c_G is the speed of seismic waves (Rolland et al., 2011; Chum et al., 2016a). The ray tracing extended up to an altitude of 300 km. The rays reach the altitudes of about 170 km and 190 km for the observed time delays of 485 s and 515 s, respectively (Figure 6.c), which is consistent with CDSS reflection heights derived from ionograms measured by the nearby Digisonde at Průhonice. Figure 6.b shows the calculated infrasound attenuation along the ray trajectories, related to the initial, near surface infrasound amplitude. The attenuation is also plotted in an alternative way in Figure 6.d, which shows the ratio w/w_0, which is the ratio of air particle oscillation velocities w at a specific height to the velocities w_0 ($w_0=v_z$) near the ground surface. The solid line represents the unrealistic case of lossless propagation (no attenuation).

The simulated ratio w/w_0 can be compared with the measured values v_z, w and w_p (w/v_z, and w_p/v_z) presented in Figure 5 (note different scales for v_z, w and w_p). The measured ratio w_p/w_z is about 50 000 and the ratio w/w_z obtained using equation (1) is about 5000. It should be stressed that the ratio w_p/w_z and hence the ratio w/w_z calculated by equation (2) is higher than the theoretical limit (about 28 000 at the height of 170 km) for lossless propagation (solid line in Figure 6.d) and significantly larger than the estimated/modeled ratio (about 15000 at 170 km) considering the attenuation. From this, it follows that the compressional term in equation (1) cannot be neglected when deriving the air velocities from the measured Doppler shift f_D. It should be remembered that there is a large uncertainty in electron density gradient derived from ionograms (~ $6{\cdot}10^6$ m^{-4} at 170 km and ~ 10^7 m^{-4} at 190 km). This may be one of the reasons why the measured ratio, of approximately 5 000 according to equation (1), is lower than the modelled one (~15000 at 170 km and ~11000 at 190 km). Another reason is the divergence of infrasound ray trajectories (geometrical factor) that is not taken into account in the simulation. The actual attenuation of wave energy is expected to be stronger due to the ray divergence than that shown in Figures 6.b and 6.d.

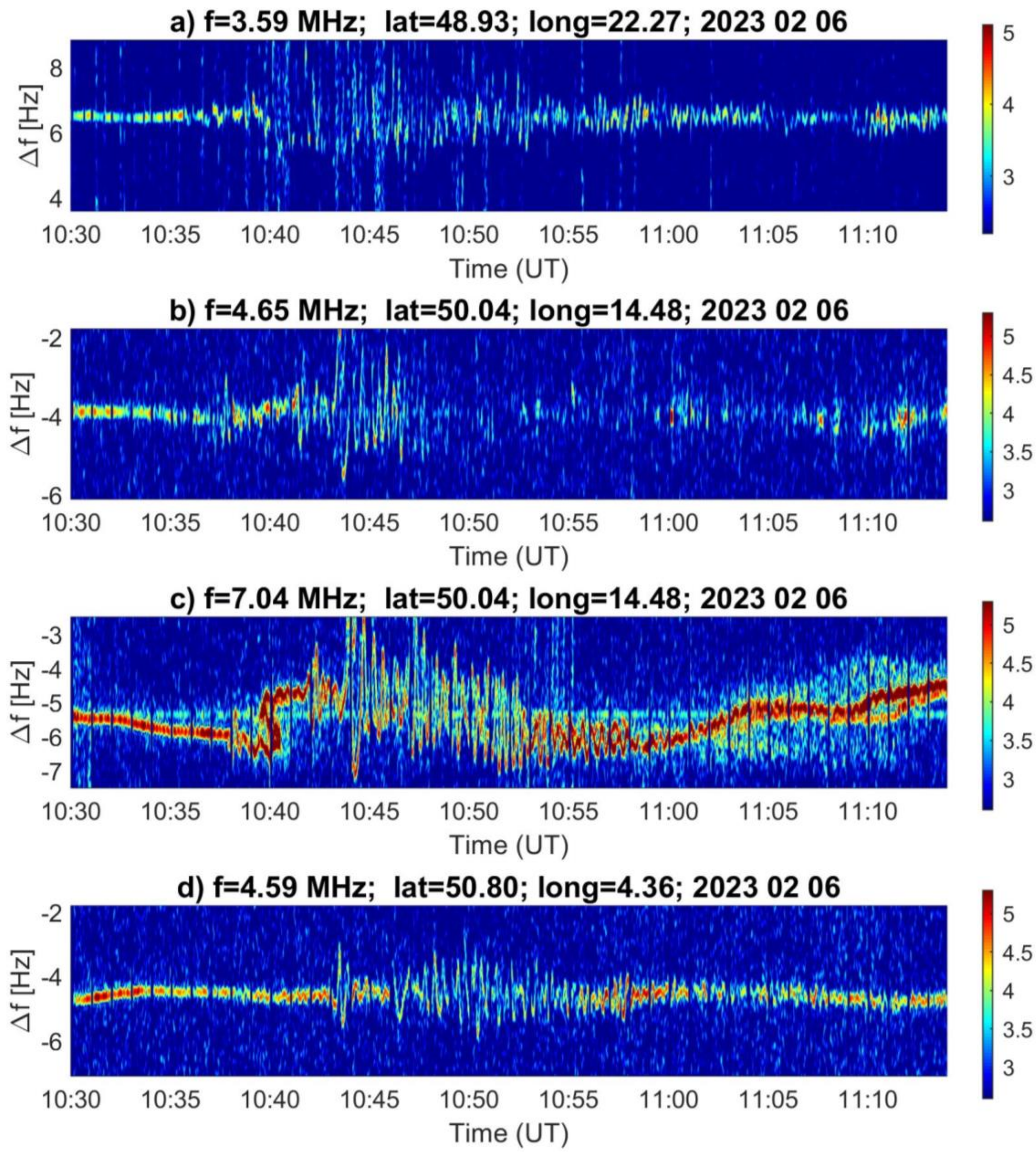

Figure 4. Doppler shift spectrogram recorded for selected sounding paths in (a) Slovakia, (b, c) Czech Republic at f=4.65 and 7.04 MHz, respectively (d) Belgium from 10:30 to 11:15 UT on 6 February 2023

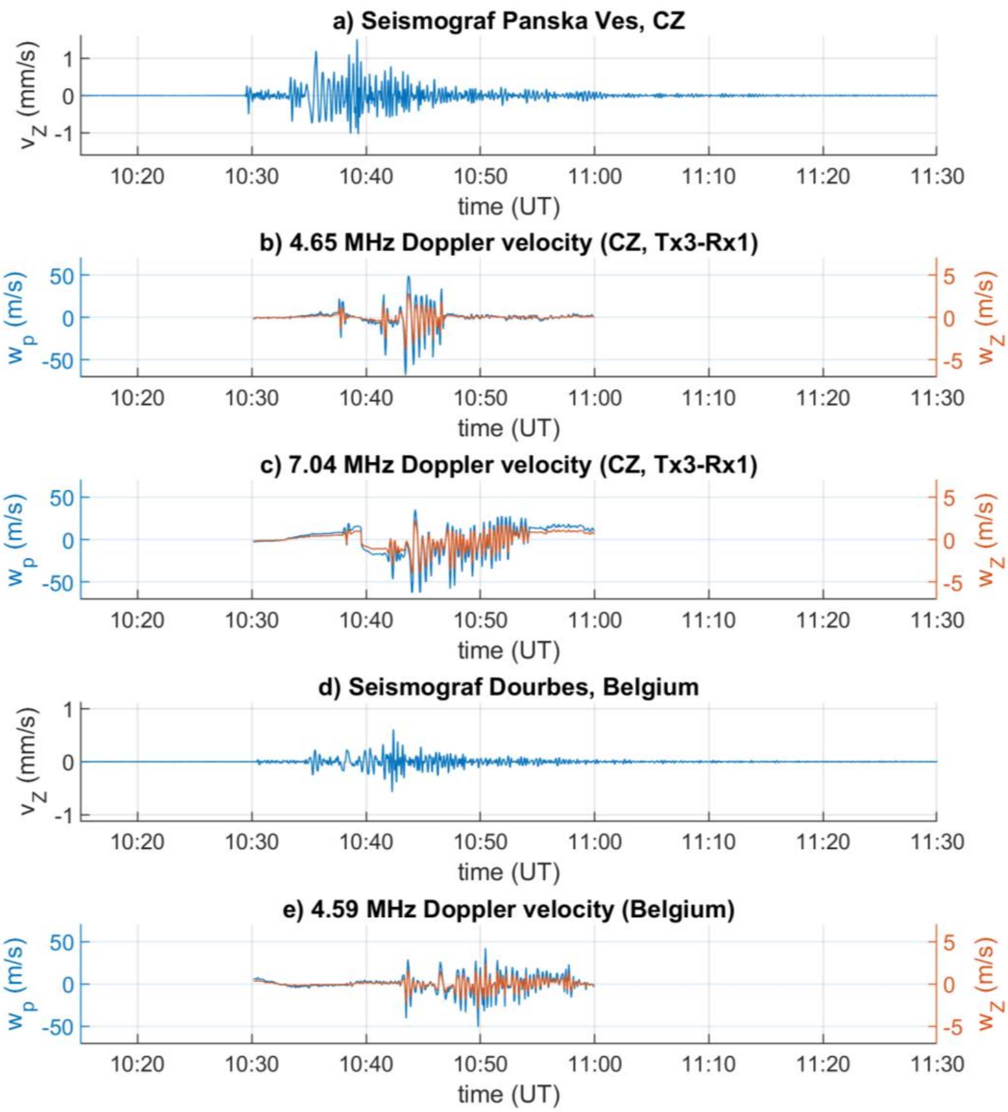

Figure 5. (a) Vertical velocity v_z of ground surface in Panska Ves, Czech Republic, (b), (c) vertical plasma velocity w_p (blue) and air particle velocity w_z (red) derived from measured Doppler shift by CDSS in the Czech Republic at 4.65 and 7.04 MHz, respectively, (d) Vertical velocity v_z of ground surface in Dourbes, Belgium and (e) vertical plasma velocity w_p (blue) and air particle velocity w_z (red) derived from measured Doppler shift by CDSS in Belgium at 4.59 MHz.

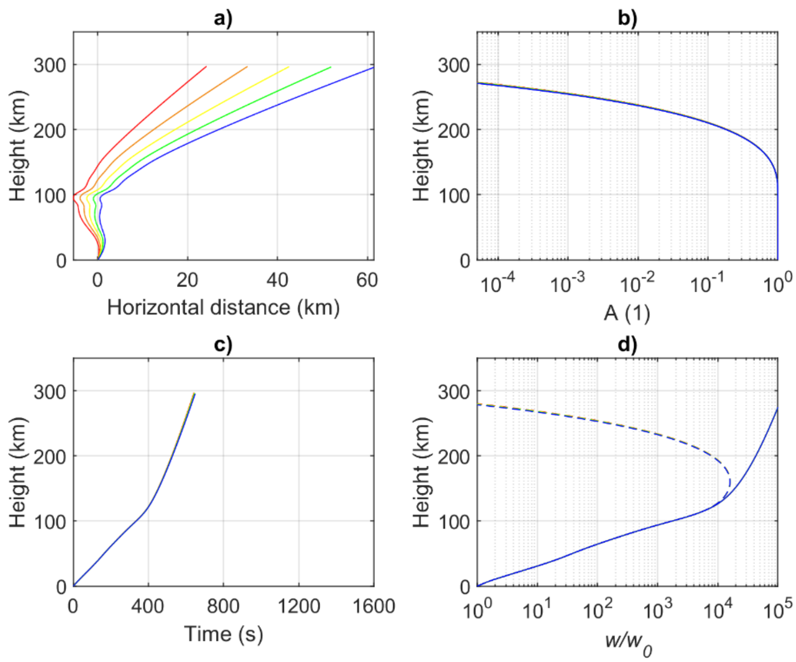

Figure 6. Ray tracing results for the infrasound waves started from the surface with zenith angle 2° (red) to 6° (blue). (a) Ray trajectories in vertical cross-section along the wave vector of seismic waves, (b) Attenuation as a function of height (relative to initial value) calculated by the analytic model assuming the wave period of 20 s, (c) Height as a function of time and (d) Ratio of air particle oscillation velocities w at a specific height related to the near surface value w_0. Solid line represents the lossless propagation.

The CDSS did not detect any co-seismic disturbances related to M=7.8 earthquake that occurred at night at 01:17:35 UT on the same day, 6 February 2023. The main reason besides the low critical frequency *foF2* (only 3.59 MHz systems experienced reflection from the ionosphere) was the high altitude of reflection (about 340 km). The simulation in Figure 6 clearly demonstrates that infrasound waves of 20 s period are strongly attenuated above about 250 km and cannot be detected by CDSS at such altitudes.
A similarity between the waveforms and spectra of the vertical ground surface velocity v_z and the air particle oscillation velocity w determined from the observed Doppler shift f_D indicates that the propagation of infrasound to the altitudes of observation in central Europe was linear. The velocities v_z and hence the initial near surface perturbations w_0 were not large enough to lead to the nonlinear phenomena in the upper atmosphere that have been observed by CDSS in the vicinity of strong earthquakes (Chum et al., 2016b; Chum et al., 2018a).

3.2 Ionograms

Each row in Figures 7 and 8 represents two ionograms for each of the ionosonde stations listed in Table 2. Here the left column shows the latest seismic undisturbed ionogram. On the corresponding ionograms for each of these stations a few minutes later (in the right column), clear multi-cusp signatures are seen. The difference in the consecutive ionograms is particularly evident at Nicosia, Athens, Gibilmanna, Juliusruh, Dourbes and Fairford. The disturbances appear to be limited to the lower F region and the cusps are particularly sharp-edged in the case of Juliusruh, Dourbes and Fairford. The cusps for San Vito, Sopron Roquetes and El Arenosillo are faint, but can still be identified when the traces are compared with the respective regular ionograms on the left.

Considering ionograms from all ionosondes involved, we were able to detect clear “MCS” on ionograms from almost all stations (with the exception of Průhonice) after 10:35 UT at which the first signature appeared at the 10:35 UT Nicosia ionogram, which is in line with the arrival of the acoustic wave in the ionosphere at approximately 10 min after the seismic disturbances generated by the 10:24 UT shock (indicated with the vertical line) as indicated in Figure 9. The appearance of the Rayleigh and Love wave signature in the ionosphere is delayed because of the propagation time of the atmospheric waves from the ground into the ionosphere after the seismic disturbance has reached the ionosonde location. In fact, associated “MCS” can be identified in the subsequent ionograms on more distant stations (as ionograms from top to bottom in Figure 7 and Figure 8 are ordered in accordance to their distance from the epicenter). Despite the fact that, ionograms at Průhonice (PQ052), due to some technical problem with the ionosonde at the time, do not contain correct polarization and direction of arrival information, the time of arrival of individual signals is, reliable. In other words – we can use the individual traces on the ionogram, but we cannot use the color codes of the signal for interpretation.

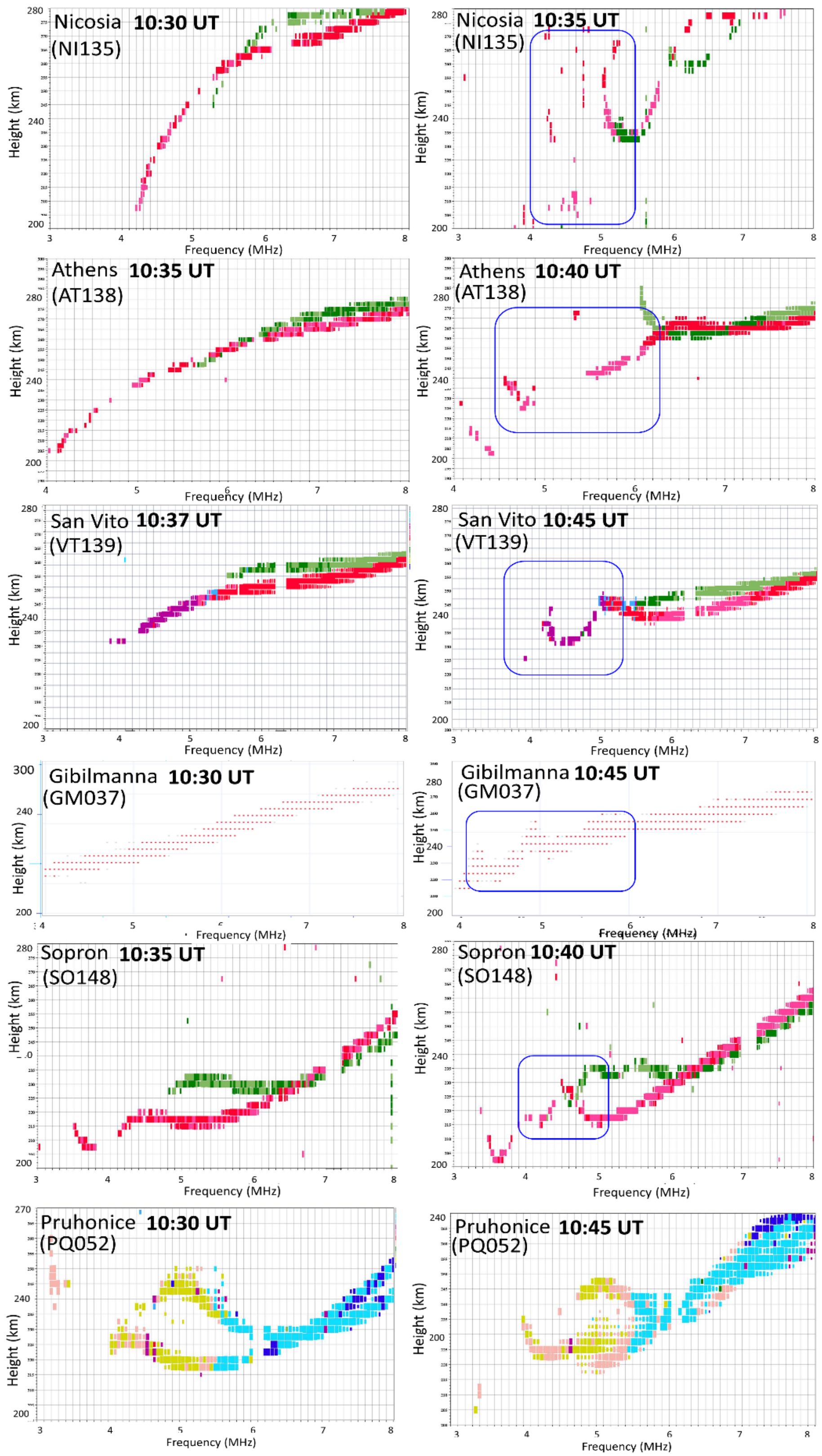

Figure 7. Successive ionograms at European stations (from top to bottom: Nicosia, Athens, San Vito, Gibilmanna, Sopron, Průhonice) registering a clear multiple-cusp signature ("MCS").

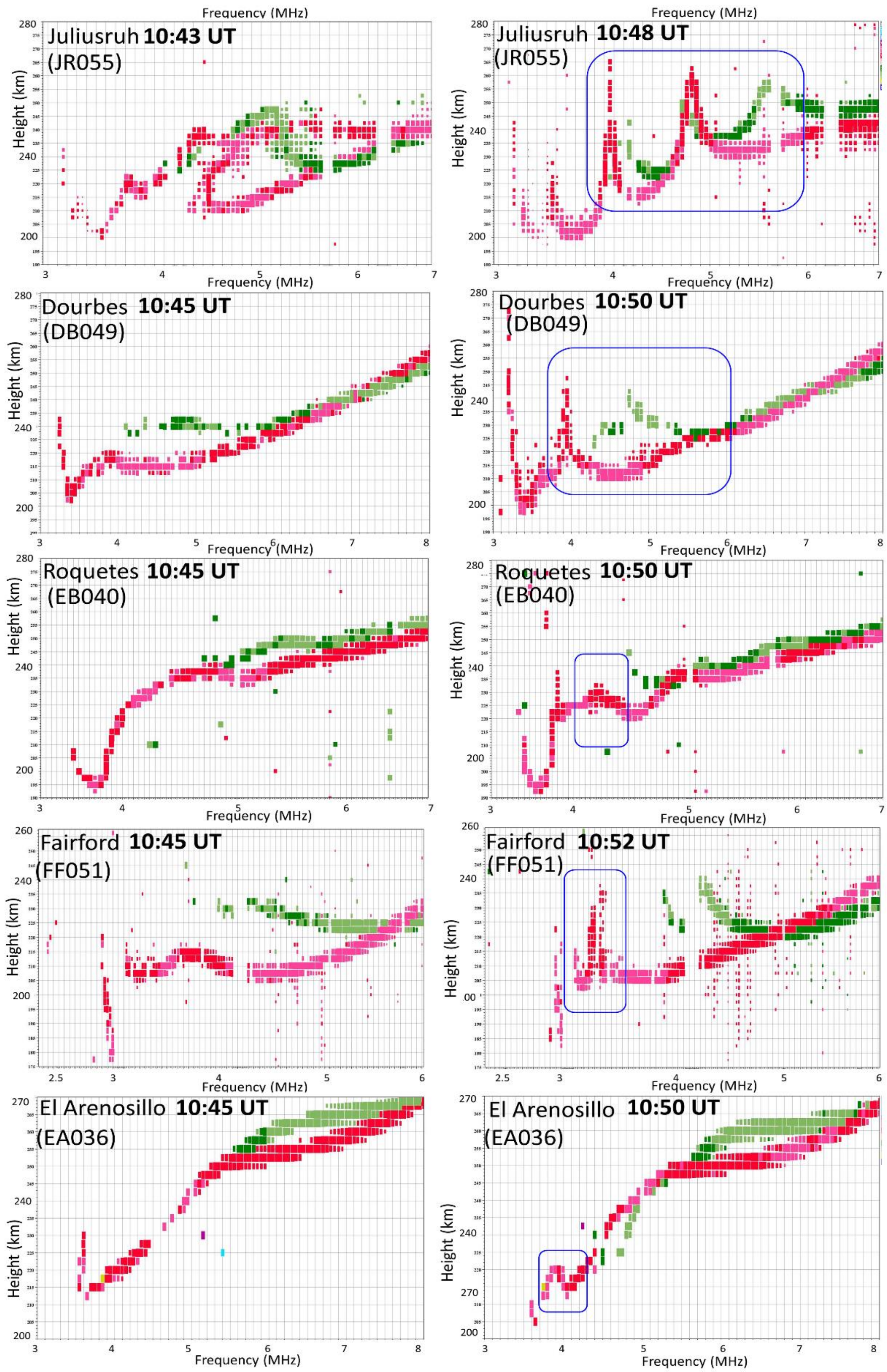

Figure 8. Successive ionograms at European stations (from top to bottom: Juliusruh, Dourbes, Roquetes, Fairford, El Arenosillo) registering a clear multiple-cusp signature ("MCS").

Figure 9 shows the time (horizontal axis) of the first acquisition of an ionogram with a "MCS" after the earthquake (red circle) with respect to the previous unaffected ionogram (white circle) as well as the time of the main shock (10:24 UT) as indicated by the red star on the x axis. Apparently we can draw a line through these points with a slope approximating the disturbance propagation velocity but clearly there exists an ambiguity in defining this line as ionograms were conducted at intervals of 5 to 15 min (Table 2). This ambiguity for each station is also reflected on the time difference between red and white circles for each ionosonde (dotted line connecting the two circles).

Compared to the high-temporal resolution provided by 1 s RINEX files in the GNSS analysis shown in section 3.3 ionosondes are operated typically at a much lower temporal resolution according to which they perform an ionogram measurement every 5-15 min intervals (as indicated by consecutive ionograms from various European stations in Figures 7 and 8). During such a time interval, an acoustic wave would cover a distance of more than 250 km under a sound velocity assumption of 0.8 km/s. Unless the ionosonde operates on a campaign mode where it performs an ionogram measurement every 30 s or 1 min it is not realistic to detect a clear typical "MCS" on consecutive ionograms.

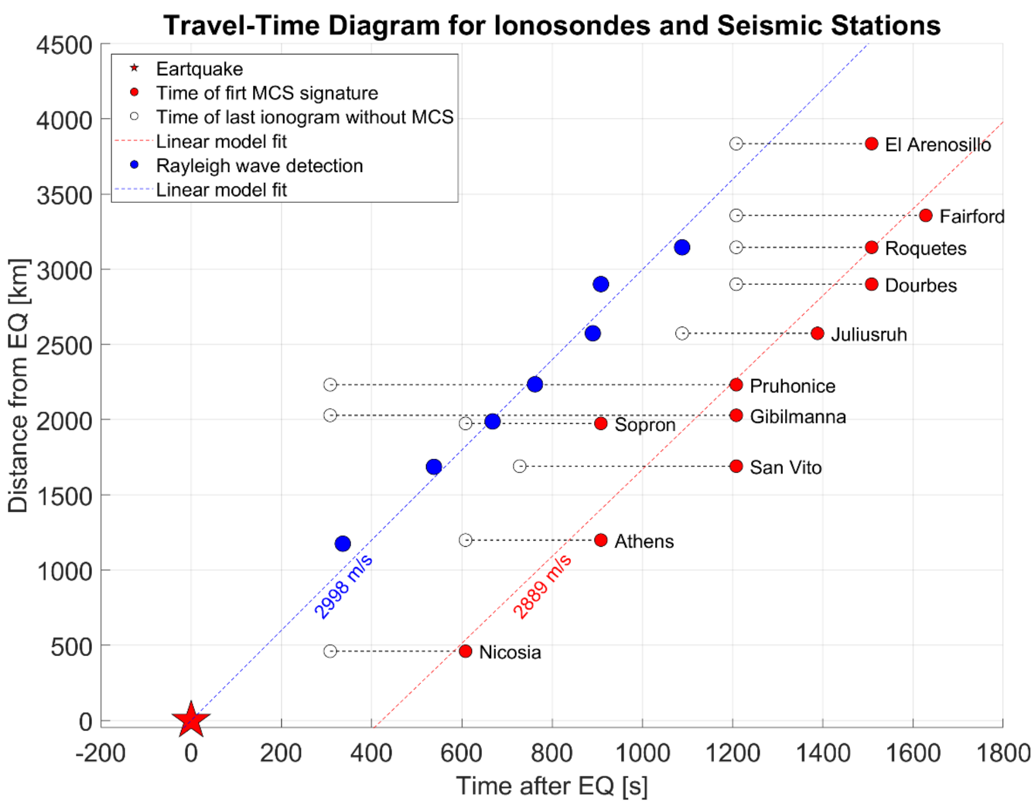

Figure 9. Travel-time diagram of co-seismic ionospheric disturbances causing "MCS"s at each station.

It is interesting to relate the time of arrival of the P, S and most importantly Rayleigh waves according to the recordings of the seismic stations shown in Table 1 and the "MCS" appearance on the ionograms indicated in Figures 7 and 8 considering the corresponding time ambiguity based on the length of the line connecting each pair of white and red circles. For example between Nicosia (nearest location to the epicenter as shown in Figure 1) and Athens, the difference in the time of arrival in the P waves (10:25:52 at Nicosia and 10:27:22 at Athens) and

S waves (10:27:07 at Nicosia and 10:29:23 at Athens) is around 1-2 min (Rayleigh waves saturate the measurements at both seismic stations) whereas the “MCS” appears clearly on ionograms that are 5 min apart (10:35 at Nicosia and 10:35 at Athens). For the San Vito ionosonde we also have a definite estimation for the arrival of Rayleigh waves (10:32:02) the “MCS” appears on the 10:45 ionogram, which is beyond the 8-10 min delay relative to the Rayleigh waves arrival at the corresponding seismic station (MESG). However, we can identify that the “MCS” is not so evident for that specific case as compared to other stations (Nicosia, Athens Juliusruh and Dourbes). In particular, for Dourbes and Juliusruh the time difference in the Rayleigh wave arrival (10:36:31 at Juliusruh and 10:37:23 at Dourbes) is comparable to the time difference of a similar “MCS” appearance on the corresponding ionograms (10:48 at Juliusruh and 10:50 at Dourbes) which underlines the clarity of the “MCS” as a function of the time with respect to the ionogram measurement. This emphasizes the importance of the ambiguity depicted in Figure 9 with respect to the clear identification of “MCS” signatures at each station and the subsequent capability to determine the acoustic wave propagation in the ionosphere based on “MCS”. Although not included in Table 1 but considered in Figure 8, the arrival time of the Rayleigh wave in the Spanish seismic stations ERTA and CMAS was at approximately 10:43 UT. The ionospheric station Roquetes (EB040) in Spain recorded the “MCS” irregularities at 10:50 that compared to the arrival time of the Rayleigh wave identified on the nearest station seismogram at 10:43, this would result in an estimated travel time of the irregularity from ground to the ionosphere of about 7-8 minutes. The latter agrees well with the estimated travel time of about ten minutes required for the vertical propagation of disturbances from the ground to ionospheric altitude (Lognonné et al., 2006; Astafyeva, 2019). The small timing differences discussed above may be also attributed to the fact that ionograms provide information on a wide area of the sky over the measuring site and not over a single point but also on differences on the radiation patterns of transmitting and receiving antennas at the ionosonde sites. A notable conclusion that we can infer from Figure 9 stems out of the parallel red and blue lines indicating the ionospheric disturbance propagation and the corresponding driver of this disturbance which is the Rayleigh wave on the surface, respectively. If we accept that MCS signatures correspond to perturbations of the electron density profile around an altitude of 140 km then the time shift of approximately 400 sec between the two (almost parallel blue and red lines) would infer a propagating upward velocity of this acoustic wave from the surface to the bottom of the F-layer at a velocity of 350 m/s.

3.3 GNSS

Once dTEC and the Ionospheric Pierce Points (IPPs) locations were calculated, we investigated the TID propagation in space through a travel-time diagram (TTD), a technique widely used to estimate velocities and time of arrival of co-seismic ionospheric waves at different locations (Astafyeva, 2019; Astafyeva et al., 2009). Moreover, we expanded the TTD further by dividing it into four sub-panels (Panel (c) of Figures 10, 11 and 12) each corresponding to different azimuthal ranges with respect to the earthquake epicenter. This modification facilitates the investigation of the anisotropies in the TID propagation and parameters, which is expected for co-seismic TIDs (Zettergren & Snively, 2019).

Figures 10, 11 and 12 show the aforementioned diagram for PRN17, PRN49 and PRN58 respectively. Note that the satellites considered were not the only ones showing clear TID signatures, but were chosen because they show the signature of both the shock acoustic wave (Afraimovich et al., 2001; Astafyeva et al., 2009; Heki & Ping, 2005) and the Rayleigh wave induced TID (Ducic et al., 2003; Rolland et al., 2011). The left Panels show the TTD itself, with the X and Y axis representing the distance in time and space to the earthquake. Panels (a) show the spatial distribution of IPPs, the epicenter location and its isodistances. Because of the TID being ion density waves, the coupling of the neutral and ionized particles is maximal along magnetic field lines since ion movement is mainly restricted along magnetic field lines (Bagiya et al., 2019; Rolland et al., 2013). Thus, when investigating the different azimuthal features we need to take into account that over Turkey the inclination and declination of magnetic field lines are respectively around 55 and 5 degrees. Panels (b) show the TTD for the stations shown in Panels (a). Note that the network used was denser than the one visible in Figure 1 (overall network figure), because we decided to show only those station-satellite links with a clear signature. Discarding such links also enabled the investigation of a possible preferred azimuth of propagation by comparing the original spatial distribution and the one of Panels (a). Specifically, we decided to plot only those arcs that showed a TID amplitude higher than 0.05 TEC units (TECu). In addition, the IPP tracks are colored according to the initial arc azimuth to the epicenter to highlight the different wave patterns. Finally, Panels (c) show a slightly different TTD, where blue and red points correspond to negative and positive TEC perturbations. Moreover, the TTD here was split into four different subpanels, each showing a different azimuthal range with respect to the epicenter. Thus, the main difference between Panels (b) and Panels (c) is that the distance shown in Panels (b) is the distance of the given IPP at the time of maximum dTEC, while Panels (c) show its time evolution.

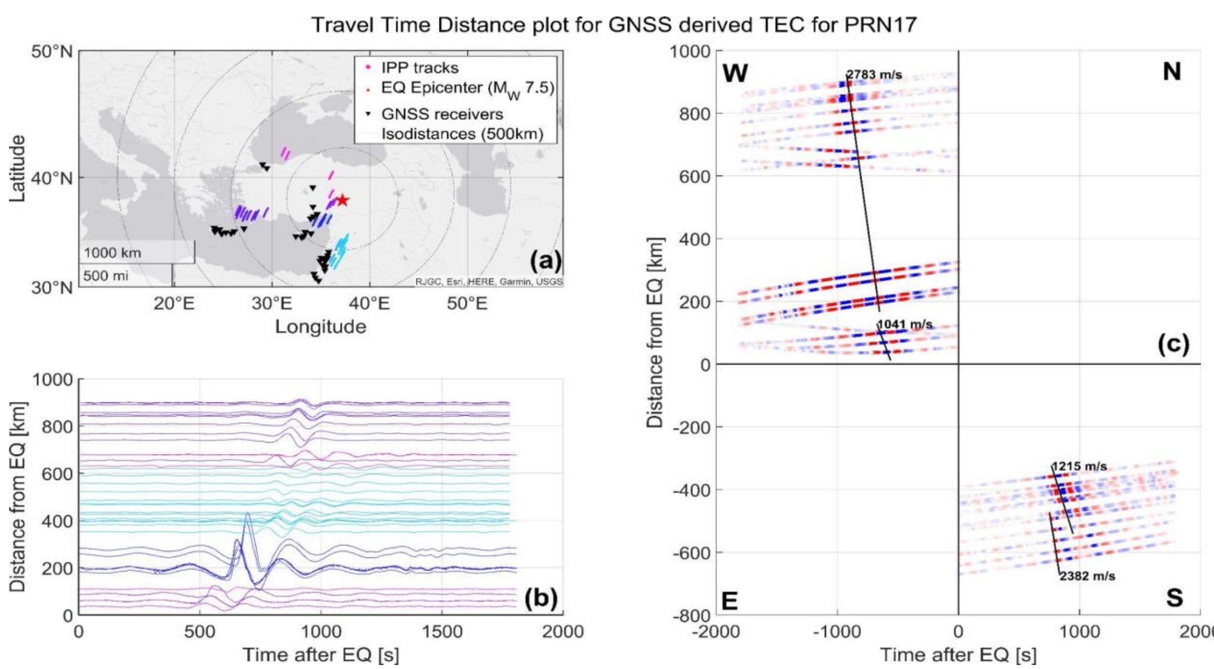

Figure 10. (a) Spatial distribution of IPPs and the epicenter location (b) Travel-time diagram for the stations shown in (a) and (c) Travel-time diagram for different azimuth for PRN17.

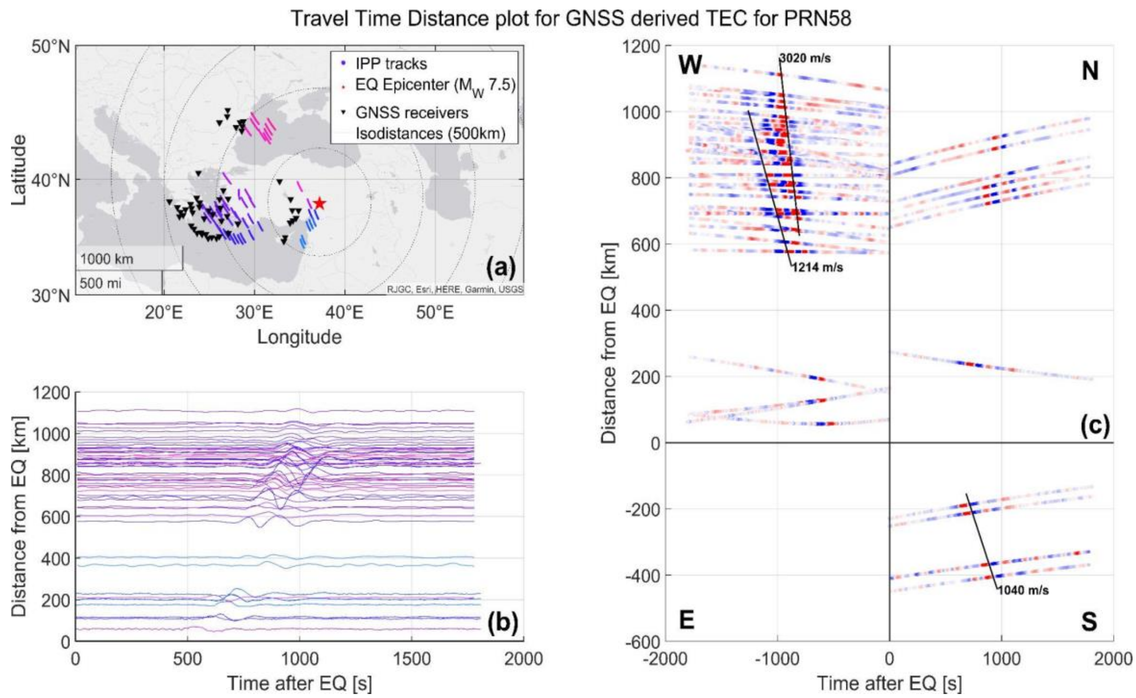

Figure 11. (a) Spatial distribution of IPPs and the epicenter location (b) Travel-time diagram for the stations shown in (a) and to be completed. (c) Travel-time diagram for different azimuth for PRN58.

Thanks to the combination of the two TTDs, we can investigate the waveform and amplitude along with the propagation velocities for different azimuthal ranges. First, Panel (b) of Figure 10 shows how a narrow azimuthal range presents a large amplitude. If we look at the corresponding IPP tracks, color-coded as in Panel (b), we can discern which geographical area these azimuths correspond to. Such waveforms are related to GNSS stations located in Cyprus, and the likely reasons for such this large amplitude could be the observational geometry (IPPs for PRN17) are actually situated over the epicenter) and earthquake characteristics (such as fault alignment and focal mechanism (Astafyeva, 2019; Astafyeva & Heki, 2009). The possible impact of such effects will be discussed below. The waveform visible in all the Panels (b) resembles the typical acoustic N shape, corresponding to an initial overpressure half cycle with a steep rise-time and a slower pressure decay followed by a half cycle of rarefaction (Astafyeva, 2019).

Panels (b), indicate waves of different nature we know from the literature to be produced by earthquakes. The first TID type, the co-seismic disturbance produced above the epicenter, is visible in both the South and West subpanels of Panel (c) of Figure 10 and 11 and in the West subpanel of Figure 12. Note here that the difference in the TID velocity is easily explained by the fact that the small distance covered by the first shock acoustic wave makes it difficult to reliably and accurately identify such waves. Moreover, the near-field TID shows almost no signature for those stations located North of the epicenter, which was expected due to the adverse geometry of the wave vector and MFLs. The lack of signatures East of the epicenter in Figure 10 and 9 is instead due to the scarcity of GNSS data accessible for those regions and as well due to the adverse observational geometry. A similar reasoning applies to the south panel of Figure 11, where due to the adverse geometry, no clear signatures are visible even if the mutual orientation of the wave vector and MFLs is optimal. The few stations that are available showed clear TID signatures East and West of the epicenter for PRN49 where the mutual orientation of the wave vector and observational link was favorable (See Figure 12). This azimuthal anisotropy is in good agreement with previous studies (Zettergren & Sniveley, 2019), which used models and measurements to explain such behaviors (Bagiya et al., 2019; Rolland et al., 2013). To sum up, the near field TID was defined by a 2-3 minutes period, a maximum amplitude of 1 TECu for stations located in Cyprus, and a propagation speed of ~1.150 km/s. In addition, such wave was detected by PRN 17, 49 and 58, East, South and West of epicenter, with signatures spanning from a few kilometers to almost 1000 km away from the epicenter.

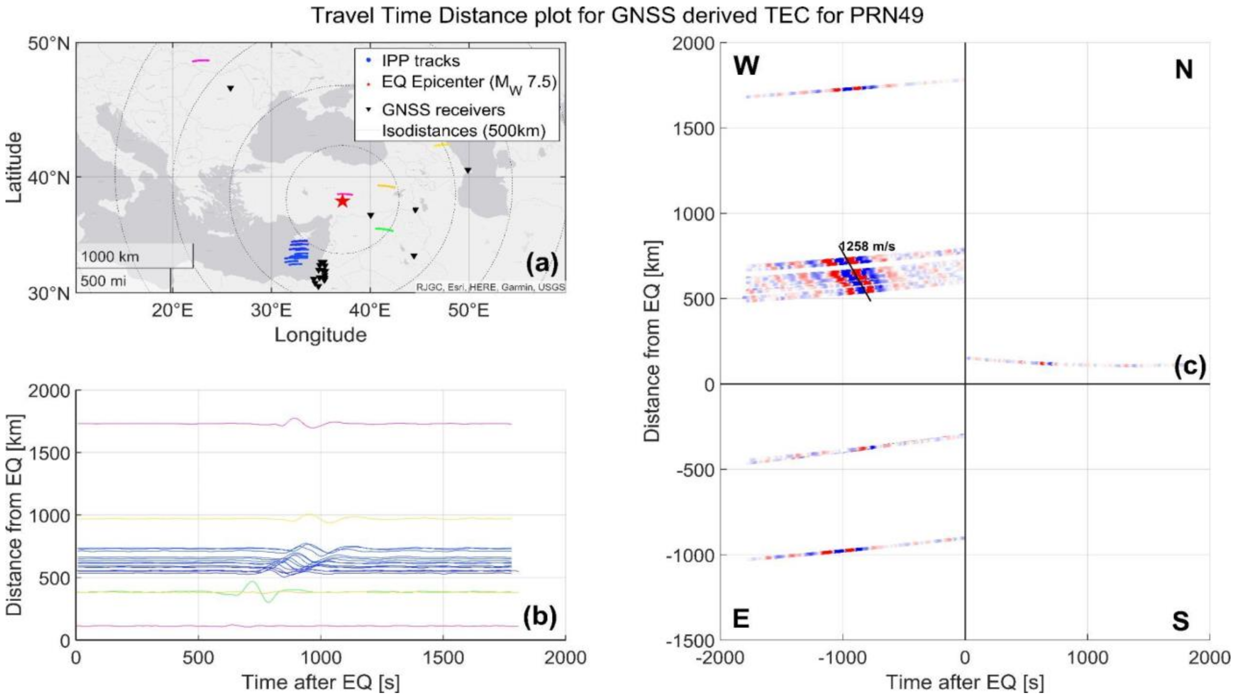

Figure 12. (a) Spatial distribution of IPPs and the epicenter location, (b) Travel-time diagram for the stations shown in (a) and to be completed. (c) Travel-time diagram for different azimuth for PRN49.

The second type of TIDs is the one produced by propagating seismic waves. The West subpanel of Panel (c) in Figure 10 shows a clear signature of such Rayleigh wave-induced TIDs. Specifically, such waves propagated at around 3 km/s, and the first signature was visible around 11 minutes after the earthquake.

Since the expected delay is normally 8 to 9 minutes, we can understand the slightly longer delay due to the fact that the Rayleigh wave had to propagate from the epicenter to the projection on the earth's surface of the first IPP that shows the TID (around 200km, which corresponds to around 1 minute). The period of such Rayleigh-induced TIDs is nearly the same as for the near-field one, thus around 2.5 minutes. Moreover, in the South quadrant of Panel (c) of Figure 10 it seems that two different waves are interacting. Specifically, the first TID signature (the one that shows a speed of 1215 m/s) is interpreted as the co-seismic TID propagating from the epicenter, while for IPPs further than -500 km, it looks as if a faster wave appeared before the near-field one and interacted with it. This pattern could be explained by Rayleigh waves propagating through the ground at speeds around three times higher than the co-seismic TID, which propagates at the speed of sound if the F-layer. Therefore, the Rayleigh wave overcoming the slower near-field TID can explain the mode splitting at around -500 km in the South quadrant. A similar behaviour is also visible in the West quadrant of Figure 11, where two TIDs appeared in the same observation arcs. The first one, with a speed of 3020 m/s, is the Rayleigh wave signature, while the slower one is the co-seismic one. The arcs showing such signatures are all further than 600km, which is consistent with Panel (c) of Figure 10, where the two modes splitting happens around 500 km of distance. This behavior of two modes splitting is typical of earthquake-induced TIDs, and many examples are available in the literature (see e.g., Astafyeva, 2019).

4. Synopsis and conclusions

The networks of different instruments (GNSS receivers, ionosondes, CDSS, seismographs) exploited for this study allowed us to study several aspects of the earthquake-induced various ionospheric disturbances. The first one to appear, was induced by the shock acoustic wave excited by the earth's crust movement close to the epicenter. The near-field TIDs parameters are in accordance with those described by Vesnin et al. (2023), and those seen for other earthquakes that have been studied in the past (Astafyeva, 2019; Kakinami et al., 2013). Moreover, as discussed in the results section, this shock acoustic wave -induced TIDs with a clear anisotropy in the azimuth of propagation, as almost no clear shock acoustic wave related signature is visible for stations located north of the epicenter. This behavior is again in agreement with models (Bagiya et al., 2019; Otsuka et al., 2006; Rolland et al., 2013) and instrumental results (Astafyeva et al., 2009; Kakinami et al., 2013).

The second type of TID detected is the one related to Rayleigh waves. Thanks to the TEC hodocrone, we know that such a wave had a speed of around 3 km/s and a period of around 2,5 minutes, a common value for this type of perturbation. As for the near-field TIDs, the Rayleigh wave shows no clear TID signatures for IPPs North of the epicenter but can instead be traced further though disturbances seen in ionograms. Note that, as the TIDs produced by earthquakes are of medium scale, they are seen as distortions in individual ionograms. As shown in Venin et al. (2023), ionospheric characteristics such as foF2 do not show a clear effect. In earlier literature (Astafyeva et al., 2009; Galvan et al., 2012, Jin et al., 2015), it was possible to trace different TID modes in GNSS derived TEC up to almost 2000 km. However, those works analysed the ionospheric response of more powerful earthquakes, with MW > 8. This can explain why we did not see a clear TEC signature at such long distances. This work illustrates the complementarity of ionosonde and GNSS receiver data, as relatively weak disturbances can still be detected as multi cusp signatures in iongorams at much larger distances.
Another pattern discernible from the GNSS-related figures common for co-seismic TIDs is the two-mode splitting, which happens around 500 and 600 km away from the epicenter for Figure 10 and 11 respectively. This two modes splitting behavior is typical of earthquake-induced TIDs, and many examples are available in the literature (Astafyeva et al., 2009; Kakinami et al., 2013).
Finally, using continuous Doppler sounding systems, it was possible to detect infrasound signatures associated with different types of seismic waves. The infrasound signature associated with the P and S waves is not discernable in the TEC data or even in the ionograms analysed. This further illustrates how the use of multiple instruments is required for observing the entire spectrum of ionospheric disturbances generated by seismic events.

It is worth comparing the ionospheric disturbances described here to those detected after the eruption of the Hunga Tonga volcano in January 2022 (e.g., Chum et al. 2023, Astafyeva et al., 2022; Themens, et al. 2022, Maletckii & Astafyeva, 2022, Verhulst et al., 2022), as the latter was the first such eruption in a long time, and the first for which data quality and coverage was comparable to the earthquake discussed here. After this eruption, TIDs were observed circling the entire globe multiple times. This is not the case for the earthquake analysed here, although TID propagation over longer distances is possible for more powerful earthquakes. However, also the mechanisms for impacting the ionosphere are different between earthquakes and volcanic eruptions. In the case of the volcanic eruption, the most significant mechanism for influencing the ionosphere was the Lamb wave, a feature not present in the context of earthquakes. Thus, although various impulsive events produce signatures in the ionosphere, the nature of their source is important in determining what type of waves will be detected. Conversely, this confirms that the details of the observed ionospheric waves can be used to identify the nature of the earthquake event, as proposed by Sevastano et al. (2017) and Astafyeva (2019).

One aspect of the observations that is clearly similar between events is the anisotropy of the propagation of ionospheric disturbances produced directly over the source. This was also seen after the Hunga eruption, as there was significant anisotropy in the TIDs close to the site of the eruption (Themens et al., 2023). Similar anisotropic propagation was also observed for TIDs from other sources, for instance in the analysis of Luo et al. (2020) concerning a major meteor impact. This therefore must be considered a general feature of TIDs excited by impulsive point sources.

Acknowledgments

Part of this work was funded by: a) T-FORS project by European Commission (number SEP-210818055) and project SAV-23-02 by the Czech Academy of Sciences.

Some of the authors were partially funded through the EU projects PITHIA-NRF (Grant nr. 101007599) and T-FORS (Grant nr. 101081835)

The contribution of VB was supported by the Hungarian National Research, Development and Innovation Office and by Bolyai Fellowship (GD, no. BO/00461/21). The ionograms from the Athens ionosonde were provided by Dr. Anna Belehaki. The authors wish to thank the seismic data to the ORFEUS (European infrastructure for seismic waveform data), furthermore to the European Integrated Data Archive (EIDA) and all the EU projects and institutions that supported them.

The datasets analyzed for this study can be found in the:

The SymH and Kp geomagnetic indices are provided by the World Data Center for Geomagnetism of Kyoto (http:// wdc. kugi. kyoto-u. ac. jp/ index. html), while the PC index by the Arctic and Antarctic Research Institute or Russia and the Technical University of Denmark (PCI, https:// pcind ex. org/). DSCOVR data are available at National Centers for Environmental Information of NOAA (https://www.ngdc.noaa.gov/dscovr/portal/index.html#/). The ionograms analysed can be found in the GIRO (https://giro.uml.edu) and eSWua http://www.eswua.ingv.it/) repositories. The CDSS data can be found in the archive maintained by IAP http://datacenter.ufa.cas.cz/). Seismic data is available in the European Integrated Data Archive (EIDA) through the following link: https://www.orfeus-eu.org/data/. The GNSS database containing all the RINEX files used for this study can be found at the following link: https://doi.org/10.5281/zenodo.7923587

Conflicts of Interest:

The authors declare no conflict of interest.

References

Afraimovich, E. L., Perevalova, N. P., Plotnikov, A. V., & Uralov, A. M. (2001). *The shock-acoustic waves generated by earthquakes*. Annales Geophysicae, *19*(4), 395–409. https://doi.org/10.5194/angeo-19-395-2001

Afraimovich, E.L., Astafyeva, E.I. & Zhivetiev, I.V. *Solar activity and global electron content*. Dokl. Earth Sc. 409, 921–924 (2006). https://doi.org/10.1134/S1028334X06060195

Astafyeva, E., & Heki, K. (2009). *Dependence of waveform of near-field co-seismic ionospheric disturbances on focal mechanisms*. *LETTER Earth Planets Space* (Vol. 61, pp. 939–943). Retrieved from www.eri.u-tokyo.ac.jp/sanchu/SeismoNote/.

Astafyeva, E., Heki, K., Kiryushkin, V., Afraimovich, E., & Shalimov, S. (2009). Two-mode long-distance propagation of co-seismic ionosphere disturbances. *Journal of Geophysical Research: Space Physics*, *114*(10). https://doi.org/10.1029/2008JA013853

Astafyeva, E., Maletckii, B., Miksell, T. D., Munaibari, E., Ravanelli, M., Coisson, P., Manta, F., and Rolland, L. (2022) *The 15 January 2022 Hunga Tonga Eruption History as Inferred From Ionospheric Observations*, Geophys. Res. Lett. 49(10), e2022GL098827, doi:10.1029/2022GL098827Astafyeva, E. (2019). Ionospheric Detection of Natural Hazards. *Reviews of Geophysics*, *57*(4), 1265–1288. https://doi.org/10.1029/2019RG000668

Astafyeva, EI. and Afraimovich, EL (2019), *Long-distance traveling ionospheric disturbances caused by the great Sumatra-Andaman earthquake on 26 December 2004*, Earth Planets and Space, Vol.58, Issue 8, 1025-1031, DOI10.1186/BF03352607

Artru, J, Farges, T and Lognonne, P. (2004), *Acoustic waves generated from seismic surface waves: propagation properties determined from Doppler sounding observations and normal-mode modelling*. Geophysical Journal International, Vol.158, Issue 3, 1067-1077, DOI10.1111/j.1365-246X.2004.02377.x

Bagiya, M. S., Sunil, A. S., Rolland, L., Nayak, S., Ponraj, M., Thomas, D., & Ramesh, D. S. (2019). *Mapping the Impact of Non-Tectonic Forcing mechanisms on GNSS measured Co-seismic Ionospheric Perturbations.* Scientific Reports, 9(1). https://doi.org/10.1038/s41598-019-54354-0

Bass H, Sutherland ELC, Piercy J, Evans L (1984), *Absorption of sound by the atmosphere*, in Physical Acoustics, Vol. XVII, Chap. 3., edited by W.P. Mason and R.N. Thurston, 145-232, Academic Press, Inc

Chum, J., F. Hruska, J. Zednik, and J. Lastovicka (2012), Ionospheric disturbances (infrasound waves) over the Czech Republic excited by the 2011 Tohoku earthquake, J. Geophys. Res., 117, A08319, doi:10.1029/2012JA017767

Chum, J., F.A.M. Bonomi, J. Fišer, M.A. Cabrera, R.G. Ezquer, D. Burešová, J. Laštovička, J. Baše, F. Hruška, M.G. Molina, J.E.Ise, J.I. Cangemi, and T. Šindelářová (2014), *Propagation of gravity waves and spread F in the low-latitude ionosphere over Tucumán, Argentina, by continuous Doppler sounding: First results*, J. Geophys. Res.Space Physics, 119, 6954–6965, doi:10.1002/2014JA020184.

Chousianitis, K., Papanikolaou, X., Drakatos, G., & Tselentis, G. -Akis. (2021). NOANET: A Continuously Operating GNSS Network for Solid-Earth Sciences in Greece. Seismological Research Letters, 92(3), 2050–2064. https://doi.org/10.1785/0220200340

Chum J., Y.-J. Liu, J. Laštovička, J. Fišer, Z. Mošna, J. Baše, Y.Y. Sun (2016a), Ionospheric signatures of the April 25, 2015 Nepal earthquake and the relative role of compression and advection for Doppler sounding of infrasound in the ionosphere, Earth, Planets, Space, 68:24, DOI 10.1186/s40623-016-0401-9

Chum, J., M. A. Cabrera, Z. Mošna, M. Fagre, J. Baše, and J. Fišer (2016b), Nonlinear acoustic waves in the viscous thermosphere and ionosphere above earthquake, J. Geophys. Res. Space Physics, 121, doi:10.1002/2016JA023450.

Chum, J., J.-Y. Liu, K. Podolská, T. Šindelářová (2018a), Infrasound in the ionosphere from earthquakes and typhoons, J. Atmos. Sol. Terr. Phys., 171, 72-82, doi:/10.1016/j.jastp.2017.07.022

Chum,J., Urbář, J., Laštovička, J., Cabrera, M. A., Liu, J.Y., Bonomi, F., Fagre, M.,Fišer, J. & Mošna, Z. (2018b), Continuous Doppler sounding of the ionosphere during solar flares, Earth, Planets and Space, 2018, 70:198, https://doi.org/10.1186/s40623-018-0976-4

Chum, J., Podolská, K., Rusz, J., Baše, J., Tedoradze, N. (2021), Statistical investigation of gravity wave characteristics in the ionosphere. Earth Planets Space 73, 60, https://doi.org/10.1186/s40623-021-01379-3

Chum J., Šindelářová T., Koucká Knížová P., Podolská K., Rusz J., Baše J., Nakata H., Hosokawa K., Danielides M., Schmidt C., Knez L., Liu J-Y., Molina M.G., Fagre M., Katamzi-Joseph Z., Ohya H., Omori T., Laštovička J., Obrazová Burešová D., Kouba D., Urbář J., Truhlík V. (2023), Atmospheric and ionospheric waves induced by the Hunga eruption on 15 January 2022; Doppler sounding and infrasound, Geophys. J. Int. (2023) 233, 1429–1443, https://doi.org/10.1093/gji/ggac517

Cicone, A., & Zhou, H. (2021). Numerical analysis for iterative filtering with new efficient implementations based on FFT. *Numerische Mathematik*, *147*(1), 1–28. https://doi.org/10.1007/s00211-020-01165-5

Dal Zilio, L., & Ampuero, J. P. (2023). Earthquake doublet in Turkey and Syria. Communications Earth & Environment, 4(1), 71

Danezis, C., Chatzinikos, M., & Kotsakis, C. (2019). LINEAR AND NONLINEAR DEFORMATION EFFECTS IN THE PERMANENT GNSS NETWORK OF CYPRUS (version 2019).

David A. Galvan, Attila Komjathy, Michael P. Hickey, Philip Stephens, Jonathan Snively, Y. Tony Song, Mark D. Butala, and Anthony J. Mannucci (2012): "Ionospheric signatures of Tohoku-Oki tsunami of March 11, 2011: Model comparisons near the epicenter," Radio Sci., 47(4), RS4003, doi:10.1029/2012rs005023

Davies K., Watts J., Zacharisen D. (1962), A study of F2-layer effects as observed with a Doppler technique. J Geophys Res 67:2. doi:10.1029/JZ067i002p00601

Dow, J. M., Neilan, R. E., & Rizos, C. (2009). The International GNSS Service in a changing landscape of Global Navigation Satellite Systems. Journal of Geodesy, 83(3), 191–198. https://doi.org/10.1007/s00190-008-0300-3

Drob, D. P., et al. (2015), An update to the Horizontal Wind Model (HWM): The quiet time thermosphere, Earth Space Sci., 2, 301–319, doi:10.1002/2014EA000089.

Eric Calais and J. Bernard Minster (1995): "GPS detection of ionospheric perturbations following the January 17, 1994, Northridge Earthquake," Geophys. Res. Lett. 22(9), 1045–1048, doi:10.1029/95gl00168.

Ducic, V., Artru, J., & Lognonné, P. (2003). Ionospheric remote sensing of the Denali Earthquake Rayleigh surface waves. *Geophysical Research Letters*, *30*(18). https://doi.org/10.1029/2003GL017812

Georges, T.M., 1973. Infrasound from convective storms: examining the evidence. Rev. Geophys. Space Phys. 11, 571–594.

Galvan, D. A., Komjathy, A., Hickey, M. P., Stephens, P., Snively, J., Song, Y. T., Butala, M. D., and Mannucci, A. J. (2012) *Ionospheric signatures of Tohoku-Oki tsunami of March 11, 2011: Model comparisons near the epicenter*, Radio Sci. 47, RS4003, doi:10.1029/2012rs005023.

Heki, K., & Ping, J. (2005). Directivity and apparent velocity of the co-seismic ionospheric disturbances observed with a dense GPS array. *Earth and Planetary Science Letters*, *236*(3), 845–855. https://doi.org/10.1016/j.epsl.2005.06.010

István Bondár and Dmitry Storchak (2011): Improved location procedures at the International Seismological Centre, Geophys. J. Int. 186(3), 1220–1244, doi:10.1111/j.1365-246X.2011.05107.x.

Jacobs JA, Watanabe T (1966) Doppler frequency changes in radio waves propagating through a moving ionosphere. Radio Science 1(3):257–264

Jin, S., Occhipinti, G., and Jin., R. (2015) GNSS ionospheric seismology: Recent observation evidences and characteristics, Earth-Sci. Rev. 147, 54--64, doi:10.1016/j.earscirev.2015.05.003.

Kakinami, Y., Kamogawa, M., Watanabe, S., Odaka, M., Mogi, T., Liu, J. Y., et al. (2013). Ionospheric ripples excited by superimposed wave fronts associated with Rayleigh waves in the thermosphere. *Journal of Geophysical Research: Space Physics*, *118*(2), 905–911. https://doi.org/10.1002/jgra.50099

Kauristie, K., Morschhauser, A., Olsen, N., Finlay, C. C., McPherron, R. L., Gjerloev, J. W., & Opgenoorth, H. J. (2017). On the usage of geomagnetic indices for data selection in internal field modelling. Space Science Reviews, 206, 61-90.

Kemal Önder Çetin, Makbule Ilgaç, Gizem Can, and Elife Çakır (2023): Preliminary Reconnaissance Report on February 6, 2023, Pazarcık M_W=7.7 and Elbistan M_W=7.6 Kahramanmaraş-Türkiye Earthquakes, Report no: METU/EERC 2023-01, Middle East Technical University – Earthquake Engineering Research Center.

Kenneth Davies and Donald M. Baker (1965): “Ionospheric effects observed around the time of the Alaskan earthquake of March 28, 1964,” J. Geophys. Res. 70(9), 2251–2253, doi:10.1029/jz070i009p02251.

Kikuchi T, Chum J., Tomizawa I, Kumiko K. K K, Hosokawa K, Ebihara Y, Hozumi K, Supnithi P (2021), Penetration of the electric fields of the geomagnetic sudden commencement over the globe as observed with the HF Doppler sounders and magnetometers, Earth, Planets and Space, 73:10, https://doi.org/10.1186/s40623-020-01350-8

Kikuchi T., Araki T., Hashimoto K. K., Ebihara Y., Tanaka T., Nishimura Y., Vichare G., Sinha A. K., Chum J., Hosokawa K., Tomizawa I., Tanaka Y., Kadokura A. (2022), Instantaneous Achievement of the Hall and Pedersen–Cowling Current Circuits in Northern and Southern Hemispheres During the Geomagnetic Sudden Commencement on 12 May 2021, Front. Astron. Space Sci. 9: 879314, https://doi.org/10.3389/fspas.2022.879314

Komjathy, A., Yang, Y. M., Meng, X., Verkhoglyadova, O., Mannucci, A. J., & Langley, R. B. (2016). Review and perspectives: Understanding natural-hazards-generated ionospheric perturbations using GPS measurements and coupled modeling. *Radio Science*, *51*(7), 951–961. https://doi.org/10.1002/2015RS005910

Kosuke Heki (2021): “Ionospheric Disturbances Related to Earthquakes,” in: Chaosong Huang and Gang Lu (eds.) Space Physics and Aeronomy, Volume 3, Ionosphere Dynamics and Applications (chapter 21), John Wiley & Sons, NJ USA, International Seismological Centre (2023), On-line Bulletin, doi:/10.31905/D808B830.

Laštovička, J., and J. Chum (2017) A review of results of the international ionospheric Doppler sounder network, Adv. Space Res., 60, 1629-1643, http://dx.doi.org/10.1016/j.asr.2017.01.032

Leonard R.S. and R.A. Barnes, Jr. (1965): “Observation of ionospheric disturbances following the Alaska earthquake,”. Geophys. Res. 70(5), 1250–1253, doi:10.1029/jz070i005p01250.

Li, H., Wang, C., & Kan, J. R. (2011). Contribution of the partial ring current to the SYMH index during magnetic storms. Journal of Geophysical Research, 116(A11), A11222.

Liu, J.Y. , Y. B. Tsai, S. W. Chen, C. P. Lee, Y. C. Chen, H. Y. Yen, W. Y. Chang, and C. Liu (2006): “Giant ionospheric disturbances excited by the M9.3 Sumatra earthquake of 26 December 2004,” Geophys. Res. Lett. 33(2), L02103, doi:10.1029/2005gl023963

Liu, J.Y., Yang, S.S., Rajesh, P.K., Sun Y.Y., Chum, J., Pan, C.J., Chu, Y.H., Chao, C.K. and Chang L.C. (2019), Ionospheric response to the 21 May 2012 annular solar eclipse over Taiwan, Journal of Geophysical Research: Space Physics, 124, 3623–3636. https://doi.org/10.1029/2018JA025928

Luca Dal Zilio and Jean-Paul Ampuero (2023): “Earthquake doublet in Turkey and Syria,” Commun. Earth Environ. 4, 71, doi:10.1038/s43247-023-00747

Lucie M. Rolland, Philippe Lognonné, and Hiroshi Munekane (2011): “Detection and modeling of Rayleigh wave induced patterns in the ionosphere,” J. Geophys. Res., 11, A05320, doi:10.1029/2010AJ016060.

Madonia, P., Bonaccorso, A., Bonforte, A., Buonocunto, C., Cannata, A., Carleo, L., et al. (2023). Propagation of Perturbations in the Lower and Upper Atmosphere over the Central Mediterranean, Driven by the 15 January 2022 Hunga Tonga-Hunga Ha’apai Volcano Explosion. *Atmosphere*, *14*(1), 65. https://doi.org/10.3390/atmos14010065

Michelini, A., Margheriti, L., Cattaneo, M., Cecere, G., D'Anna, G., Delladio, A., et al. (2016). The Italian National Seismic Network and the earthquake and tsunami monitoring and surveillance systems. Advances in Geosciences, 43, 31–38. https://doi.org/10.5194/adgeo-43-31-2016

NOAA Space Weather Prediction Center (2016): Deep Space Climate Observatory (DSCOVR). NOAA National Centers for Environmental Information. Dataset. http://doi.org/10.7289/V51Z42F7

Maletckii, B. and Astafyeva, E. (2022) *Near-Real-Time Analysis of the Ionospheric Response to the 15 January 2022 Hunga Tonga-Hunga Ha'apai Volcanic Eruption*, J. Geophys. Res. 127(10), e2022JA030735, doi:10.1029/2022JA030735.

Mannucci, A. J., Wilson, B. D., Yuan, D. N., Ho, C. H., Lindqwister, U. J., & Runge, T. F. (1998). A global mapping technique for GPS-derived ionospheric total electron content measurements. *Radio Science*, *33*(3), 565–582. https://doi.org/10.1029/97RS02707

Maruyama, T., Tsugawa, T., Kato, H., Saito, A., Otsuka, Y., and Nishioka, M.: Ionospheric multiple stratifications and irregularities induced by the 2011 off the Pacific coast of Tohoku Earthquake, Earth Planets Space, 63, 65, https://doi.org/10.5047/eps.2011.06.008, (2011)

Maruyama, T., T. Tsugawa, H. Kato, M. Ishii, and M. Nishioka, Rayleigh wave signature in ionograms induced by strong earthquakes, J. Geophys. Res., 117, A08306, doi:10.1029/2012JA017952, (2012)

Maruyama, T., and H. Shinagawa, Infrasonic sounds excited by seismic waves of the 2011 Tohoku-oki earthquake as visualized in ionograms, J. Geophys. Res. Space Physics, 119, 4094–4108, doi:10.1002/2013JA019707, (2014)

Nava, B., Coisson, P., & Radicella, S. M. (2008). A new version of the NeQuick ionosphere electron density model. *Journal of Atmospheric and Solar-Terrestrial Physics*, *70*(15), 1856–1862. https://doi.org/10.1016/j.jastp.2008.01.015

Otsuka, Y., Kotake, N., Tsugawa, T., Shiokawa, K., Ogawa, T., Saito, S., et al. (2006). *GPS detection of total electron content variations over Indonesia and Thailand following the 26 December 2004 earthquake*. *Earth Planets Space* (Vol. 58, pp. 159–165).

Ouml, & Yildirim, M. (2011). A comparative analysis of the virtual reference stations (VRS). Scientific Research and Essays, 6(27), 5726–5733. https://doi.org/10.5897/SRE11.786

Perevalova, V, V.A. Sankov, E.I. Astafyeva, and A.S. Zhupityaeva (2014): “Treshold magnitude for ionospheric TEC response to earthquakes,” J. Atmos. Sol. Terr. Phys. 108, 77–90, doi:10.1016/j.jastp.2013.12.014.

Philippe Lognonné, Juliette Artru, Raphael Garcia, François Crespon, Vesna Ducic, Eric Jeansou, Giovani Occhipinti, Jérôme Helbert, Guilhelm Moreaux, and Pierre-Emmanuel Godet (2006): “Ground-based GPS imaging of ionospheric post-seismic signal,” Planet. Space Sci. 54(5), 528–540, doi:10.1016/j.pss.2005.10.021.

Rolland, L., Lognonné, P., Munekane, H. M., Rolland, L. M., & Munekane, H. (2011). Detection and modeling of Rayleigh wave induced patterns in the ionosphere. *Journal of Geophysical Research Space Physics*, *116*(A5), 5320. https://doi.org/10.1029/2010JA016060ï

Rolland, L. M., Vergnolle, M., Nocquet, J. M., Sladen, A., Dessa, J. X., Tavakoli, F., et al. (2013). Discriminating the tectonic and non-tectonic contributions in the ionospheric signature of the 2011, Mw7.1, dip-slip Van earthquake, Eastern Turkey. *Geophysical Research Letters*, *40*(11), 2518–2522. https://doi.org/10.1002/grl.50544

Sevastano, G., Komjathy, A., Verkhoglyandova, O. Mazzoni, A., Crespi, M., Wei, Y. et al. (2017) Real-Time Detection of Tsunami Ionospheric Disturbances with a Stand-Alone GNSS Receiver: A Preliminary Feasibility Demonstration, Sci. Rep. 7, 46607, doi:10.1038/srep46607.

Sindelarova T., Mosna Z., Chum J., Kouba D., Base J., Liu J.Y., and Katamzi-Joseph Z. (2018), Solar eclipse effects in the ionosphere observed by continuous Doppler sounding, Adv. Space Res., 62, 785-800, http://dx.doi.org/10.1016/j.asr.2018.05.029

Stauning P (2013) The polar cap index: a critical review of methods and a new approach. J Geophys Res Space Phys 118(8):5021–5038

Strollo, A., Cambaz, D., Clinton, J., Danecek, P., Evangelidis, C. P., Marmureanu, A., & Triantafyllis, N. (2021). EIDA: The European integrated data archive and service infrastructure within ORFEUS. Seismological Society of America, 92(3), 1788-1795.

Takashi Maruyama, Kamil Yusupov, and Adel Akchurin (2016a): “Interpretation of deformed ionograms induced by vertical ground motion of seismic Rayleigh waves and infrasound in the thermosphere” Ann. Geophys. 34(2), 271–278, doi:10.5194/angeo-34-271-2016.

Takashi Maruyama, Kamil Yusupov, Adel Akchurin (2016b): “Ionosonde tracking of infrasound wavefronts in the thermosphere launched by seismic waves after the 2010 M8.8 Chile earthquake,” J. Geophys. Res. 121(3), 2683–2692, doi:10.1002/2015ja022260.

Torres, J. A., Altamimi, Z., Boucher, C., Brockmann, E., Bruyninx, C., Caporali, A., et al. (2009). Status of the European Reference Frame (EUREF). In M. G. Sideris (Ed.), Observing our Changing Earth (pp. 47–56). Berlin, Heidelberg: Springer. https://doi.org/10.1007/978-3-540-85426-5_6

Themens, D. R., Watson, C., Žagar, N., Vasylkevych, S., Elvidge, S., McCaffrey, A., Prikryl, P., Reid, B., Wood, A., and Jayachandran, P. T. (2022) Global Propagation of Ionospheric Disturbances Associated With the 2022 Tonga Volcanic Eruption, Geophys. Res. Lett. 49(7), e2022GL098158, doi:10.1029/2022GL098158.

US Geological Survey (2023): Event page of the M7.8 - Pazarcik earthquake, Kahramanmaras earthquake sequence, https://earthquake.usgs.gov/earthquakes/eventpage/us6000jllz/executive.

Vanlommel, P. (2018). Solar-Terrestrial Centre of Excellence (STCE) Newsletter, issue 17 Feb 2023. Available online at https://www.stce.be/newsletter/.

Verhulst, T. G. W., Altadill, D., Barta, V., Belehaki, A., Burešová, D., Cesaroni, C., et al. (2022). Multi-instrument detection in Europe of ionospheric disturbances caused by the 15 January 2022 eruption of the Hunga volcano. *Journal of Space Weather and Space Climate*, *12*, 35. https://doi.org/10.1051/swsc/2022032

Vesnin A, Yasyukevich Y, Perevalova N, Şentürk E. Ionospheric Response to the 6 February 2023 Turkey–Syria Earthquake. Remote Sensing. 2023; 15(9):2336. https://doi.org/10.3390/rs15092336

Watada S, Kunugi T, Hirata K, Sugioka H, Nishida K, Sekiguchi S, Oikawa J, Tsuji Y, Kanamori H (2006) Atmospheric pressure chase associated with the 2003 Tokachi-Oki earthquake. Geophys Res Lett 33, L24306. doi:10.1029/2006GL027967

Xing Meng, Panagiotis Vergados, Attila Komjathy, and Olga Verkhoglyadova (2019): “Upper Atmospheric Responses to Surface Disturbances: An Observational Perspective,” Radio Sci. 54(11), 1076–1098, doi:10.1029/2019rs006858.

Zettergren M.D. and J.B. Snively (2019): “Latitude and Longitude Dependence of Ionospheric TEC and Magnetic Perturbations From Infrasonic-Acoustic Waves Generated by Strong Seismic Events,” Geophys. Res. Lett. 46, 1132–1140, doi:10.1029/2018GL081569.